IEM JOURNAL

MAJLIS BAGI SESI 2004/2005 (IEM COUNCIL SESSION)

CONTENT

INTERNATIONAL ADVISORY PANEL

BRANCHES

Agriculture Drainage Affects River Water Quality

Ayob Katimon, Azraai Kassim, Fadil Othman, Johan Sohaili, Zulkifli Yusop and Normala Hashim
Faculty of Civil Engineering, Universiti Teknologi Malaysia,
81310 UTM Skudai, Johor Darul Takzim

ABSTRACT

The acidic level of the freshwater is a major concern to water treatment plant operators. Extremely acidic freshwater could affect the operation of the treatment plant in many ways. The cost to neutralisation the water would increase and treatment scheduling would be more complicated. This paper reports the influence of agricultural drainage on river water quality in Bekok river system in Johor, Malaysia. The river is the sole source of freshwater supply to two water treatment plants located at the downstream reach of the river. Three water quality parameters, i.e. pH, Iron and Ammonia-N, were used as an indication parameter. Water samples collected from 16 different river reaches along the 20-km river were analysed. A significant decrease in pH was found near the water intake point, where most of the drained areas are located. The study also found that in general, the quality of the river water was better during low flow condition (non-rainy days) compared to high flow (rainy days). Multiple regression analysis showed that pH was significantly related to Iron and Ammonia contents.

Keywords : *Agricultural drainage, water quality, river, watershed*

INTRODUCTION

Stream water contamination from non-point source pollution has been a current issue in river system management of agricultural country [10]. This is particularly true when part of the river reach has to flow through an agricultural area where intensive farming activities are located. Literature had shown that the use of various type of agricultural chemicals [3] and the modification of the riverbank lands through the construction of intensive drainage infrastructure contributed to the degradation of surface water quality in the adjacent streams. The acidity level in the stream as collectively indicated by the pH values would provide a general scenario of these phenomena.

The acidic level in a river system is of paramount important if the river is to be used as source of public water supply. For instance, according to the World Health Organization [14] and the Malaysian Water Association [7] water supply guidelines standard (Table 1), the highly acidic water of pH less than 3 would incur a tremendous treatment cost in terms of neutralizing agent (liming materials) before the water could publicly be used [4]. A further reduction in pH value would cause the operation of the treatment plant to be delayed because the raw water may become toxic and unsuitable for drinking purposes.

Under natural conditions, rivers convey surface and sub-surface water from the higher point to the lower part of the watershed and eventually reaches the sea. The river system would include the riverbanks or flood plain of the catchment area that is hydrological and hydraulically important. When an integrated water resources development is planned within the river basin, alterations to the physical aspect of the watershed characteristics are expected. For example, if a watershed is to be used as a source for raw water supply to a treatment plant, a dam has to be built to store the surface water. Similarly, if agricultural crop has to be grown inside the watershed area, drainage canals along the flood plain or waterlogged area have to be built to enable crop to be grown and to avoid flooding [5]. Agricultural drainage, for instance, would change the ecosystem or the physical and chemical behaviors of the soil to some extent. For example, the pre-matured or young alluvium soils like those found along the riverbanks are generally sensitive to the changes in their horizon development [11].

Though the general environmental impact of land use changes on the overall river regime is clearly understood [12; 2] little is known on the effect of the changes in soil ecosystem on the quality of the receiving river, under the tropical Malaysian conditions. Understanding the impact of soil drainage on the stream water quality is important particularly if the river is to be used for domestic purposes. This is especially true where most of Malaysian River systems being used for domestic raw water supply flow through agricultural areas where soil drainage activities are taking place.

The purpose of this study was to investigate the impact of agricultural soil drainage taking place along the riverbanks on the receiving water quality. More specifically, this study looked into the effects of soil oxidation processes occurring during drainage canalization works on the acidity of the surface water. The study was accomplished through water quality survey at the certain reaches of the river.

The study of the effect of agricultural drainage on the receiving water quality was conducted based on the following hypotheses;

- The naturally acidic soil in the catchment was the main contributing factor to the high acidity of the Bekok River.
- The land development along the river system through the

Table 1 : Recommended/Acceptable physical water quality criteria

Parameter	Raw Water Quality	Drinking Water Quality
Total coliform	5000 count/l	0
Turbidity	1000 NTU	5
Color	300 Hazen	15
pH	5.5-9.0	6.5-9.0
(Sources: Twort et al. 1985; MWA, 1994)		

construction of an intensive field drainage system for agricultural purposes has accelerated the acidification process of the soil.

MATERIALS AND METHODS

The Study Site

This study was carried out in Bekok River System in Johor, Malaysia (103° 00' 00" E, 2° 05' 00" N). The river is one of the major fresh water sources to the domestic water supply in Batu Pahat. The river basin covers more than 100km^2 with the major river flowing down all the way from the upstream to the downstream portion where intensive multiple crops (vegetables, banana and oil palm) farming is practiced along the flood plain. Water treatment plants are located at the downstream reach of the river. These treatment plants depend solely on the raw water supply from the Bekok River. Thus the river quality will directly impact the performance of these water treatment plants.

Figure 1 is the study site showing the watershed and the river system, the agricultural drainage and the location of the water treatment plants. **Figure 2(a)** is the topographic map of the study catchment showing the general landform of the watershed. A significant portion of the area belongs to low lying areas (area of less than 4m from mean sea level). The area along the riverbanks was generally flat with shallow water table and flood prone in nature. From the conservation point of views, these areas can be considered as part of buffer zone or flood plain of the river system.

Figure 2(b) shows the landuse pattern of the study catchment. Intensive farming activities are taking place in these areas because of easy and direct access to the water supply. A mixed agriculture (seasonal crops such as corn and vegetables and perennial crops such as palm oil and bananas) is being practised in almost all parts of the area. Because of the low-lying areas, open drainage canals of 1.2 meter deep at 400 meters interval were constructed up to field level to avoid crops from flooding. The soil types of these areas are considered as young river-alluvial and potentially acidic with substantial percentage belong to peat soil.

Water Sampling Points

A series of water quality sampling was conducted during relatively low flow (dry condition) and high flow (wet condition). Water samples were taken six times within seven months. The rainfall data prior to the survey was used to indicate relatively dry or wet days. In addition, antecedent rainfall values usually indicate the soil moisture status, thus the leaching potential of the groundwater runoff.

The selection of the sampling stations was according to the distant from the water treatment plants, along the main river as well as at the discharge points of the drainage canals. Sixteen sampling stations of about 0.5-0.75km apart were identified **(Figure 2 (c))**. Fifteen water quality parameters were measured and analyzed. However only three of them i.e. *pH, NH$_3$-N* and ferrous are detailed in this paper. *pH* was also measured in one of the drainage block (so called suspected point source area) to determine the acid level of that particular drained field area. As shown in **Figure 2(d)**, the chosen drainage block was provided with proper drainage facilities, up to the field level.

RESULTS AND DISCUSSION

Soil and Water Acidification Processes

Soil acidification process can possibly occur through three different mechanisms. The first is through soil weathering process [12], the second, through the process of the oxidation of pyrite substances in soil, and third through the accumulation residual of agricultural fertilizers [6]. While the soil weathering is a natural process and is beyond human control, the other two mechanisms are simply man-made.

Soil weathering is a natural soil formation process. The interaction between mineral (mica) element contained in the soil particles and the *H$^+$* of the rain water could cause the soil to be more acidic. The mechanism is difficult to control unless a non-acidic rain is warranted. The polluted rain water caused by industrial urban activities are generally the main contributing factors for acidic rain.

The second mechanism is closely related to man-made activities. The oxidation of *FeS$_2$* in the soil was due to the decomposition of pyrite material or sulfate of the soil. The oxidation process would cause a serious soil acidification particularly when the pyrite exposed to oxygen (air). Eventually, such process would produce ferric ion and ferric hydroxide and the soil became more and more acidic [9]. In relation to this, the construction of agricultural drainage system in low-lying areas of the river basin would lower the water table of these areas.
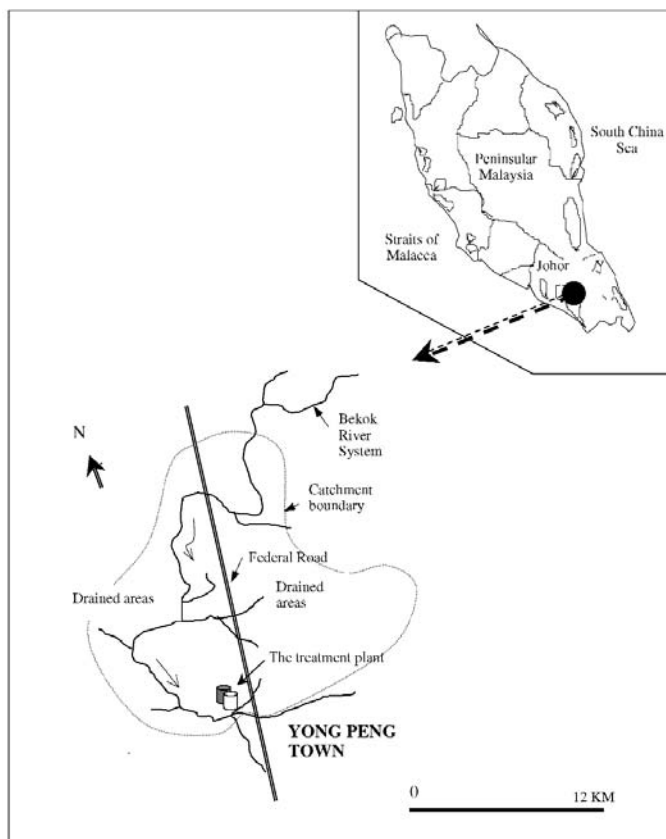
Figure 1 : The study location showing the river system and the water treatment plant
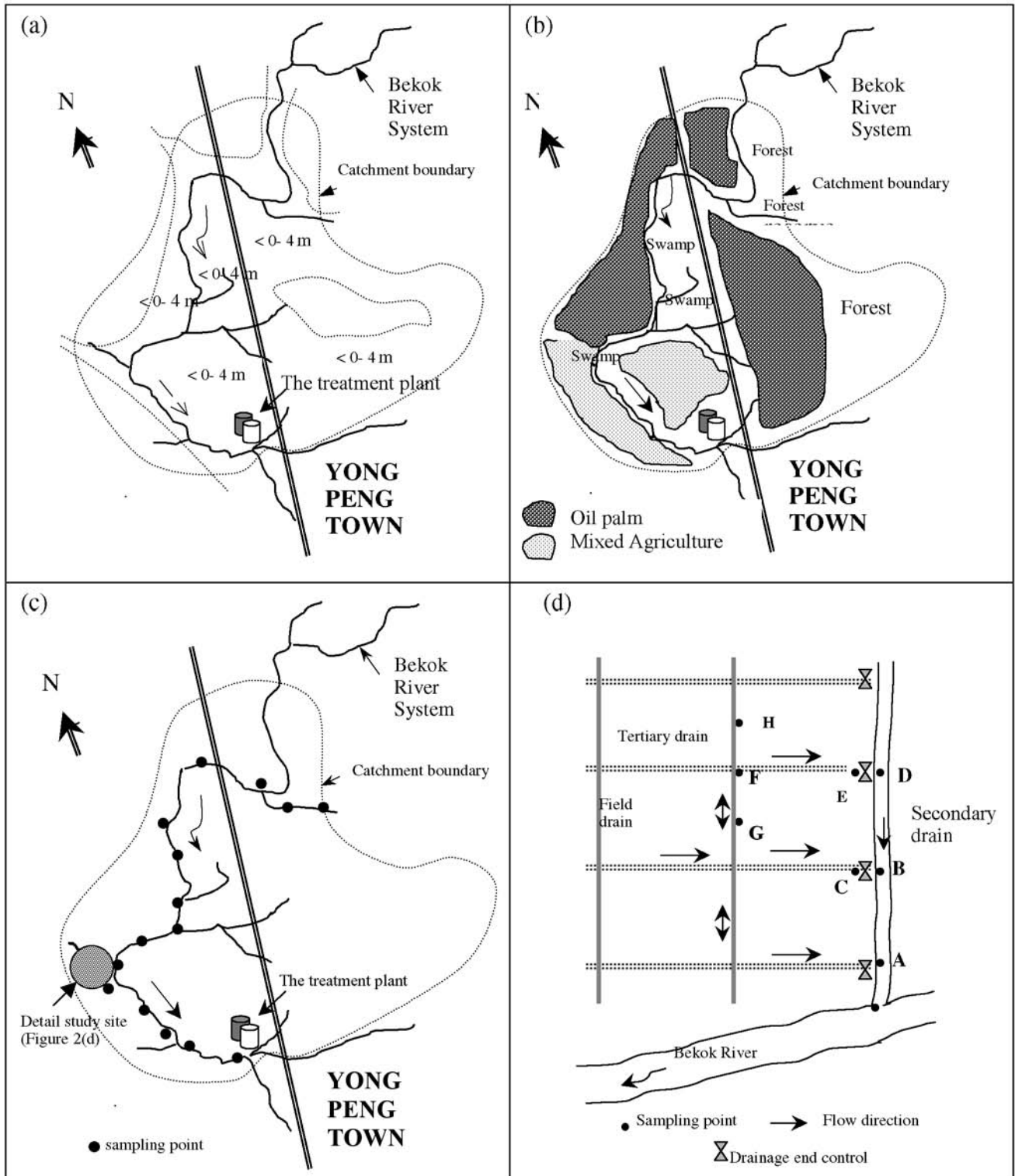
Figure 2 : (a) Topographic feature (b) Agricultural land-use (c) Water quality sampling points (d) Drainage system at block level

Consequently, more soil surface of the basin would be exposed to the air and this will accelerate the soil oxidation process. As illustrated in **Figure 3**, with the help of rainfall, the oxidized pyrite element will infiltrate and accumulate into the soil profile (particularly at horizon A of the soil), before it being leached to the river mouth through the subsurface flow processes.

The Soil Acidity

Many tropical soils especially those located along the river belong to potentially acidic soils. These soils are considered as young soils where weathering and formation process are still occurring. To verify the acidity level, the soil *pH* was determined. The result of the test is given in Table 2. The average *pH* is below 4.0 which can be categorized as acidic soil.

WATER QUALITY OF THE BEKOK RIVER

pH

The *pH* of surface water could indicate the general pattern of the acid level of the river. In a more scientific form *pH* represents

Table 2. The soil pH in the Bekok Catchment

Sampling Point	Soil depth (cm)	pH			
		1	2	3	Average
A	0-15	3.58	3.60	3.60	3.59
	15-30	3.82	3.92	3.84	3.86
	30-45	3.45	3.50	3.47	3.47
B	0-15	3.75	3.57	3.53	3.62
	15-30	3.51	3.57	3.48	3.62
	30-45	2.92	2.90	2.90	2.91

1: Fe³⁺ moved up to the ground surface
2, 3: Rain water plus Fe³⁺ infiltrated into the soil profile
4: Oxidized Fe³⁺ transported into the drainage canal through surface runoff
5: Oxidized Fe³⁺ transported into the drainage canal through sub-surface runoff
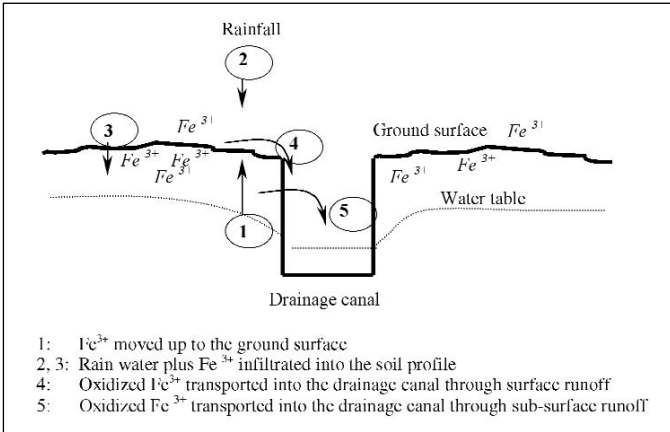
Figure 3. The mechanism of Fe^{3+} transport from the ground surface and soil profile to the drainage canal

the hydrogen ion (H⁺) contents in water. **Figure 4(a)** shows the mean *pH* of the Bekok River during relatively dry and wet days.

During the wet condition with relatively high flow, the surface water was generally more acidic compared to that of during dry period. During the rainy days the soil is wet and may be saturated. Under such soil conditions the leaching process is likely to happen more rapidly. Thus the transfer of the soluble ion through subsurface drainage from the soil profile into the drainage canals and subsequently into the river system is more obvious [4]. On the other hand, during dry days where the soil profile is relatively dry, the leaching process occurs at minimum rate.

The *pH* value of water can be significantly affected by its temperature. However, under the running water condition, a direct relationship between *pH* and surface water temperature is not obvious. The observed surface water temperature during the wet days was generally lower compared to that of dry period. The average measured stream water temperature was between 27-29°C and 29-31°C for wet and dry days respectively. This is to be expected because during wet days the river flow is higher. Thus the surface water temperature tended to decrease as the water became more aerated. Under such situation the tendency of the hydrogen ion to be neutralized is tended to be higher resulting in higher *pH* values.

NH_3-N and Fe^{2+}

Concentration of *NH_3-N* and ferrous *(Fe^2+)* of the Bekok River under different weather conditions are depicted in **Figures 4(b)** and (c). While the acid level in the surface water is collectively indicated by their *pH* values, the ammonia and ferrous levels would give some indication on the amount of the residual agricultural materials transported into the river. The *N* content, for

instance, would indicate the amount of nitrogen fertilizer leakage into the surface water [13] while the Fe^2+ would represent other toxic elements in the soil profile. As for hydrogen ions, these toxic ions are potentially get leached into the river system along with subsurface runoff.

Comparatively, the observed *N* values are within an acceptable guidelines [7] for raw water supply of 0.5 mg/l or lower. However the *Fe* content of the surface water was found higher than that proposed in the guidelines. The recommended acceptable value for *Fe* for raw water supply is 1.0 mg/l or lower. To explain these *N* and *Fe* contents in the Bekok River, it can be proposed that the Bekok River is still free from *N* contamination but not *Fe*. The high level of *Fe* in the surface water is expected as a result of soil acidification process through soil drainage activities in the area.

Other water quality parameters

The present level of other water quality parameter of the river system under study are as follow; *BOD<1.0 mg/l, COD<50 mg/l, Phosphorous<0.5 mg/l, Manganese<0.2 mg/l, Suspended Solids<3.0 mg/l* and *Total Coliform <3.0 count/100 ml*. The results obtained suggest that the river under study is still free of heavy metal contamination. This is expected as the entire river basin is categorized as an agricultural watershed with fully vegetated.
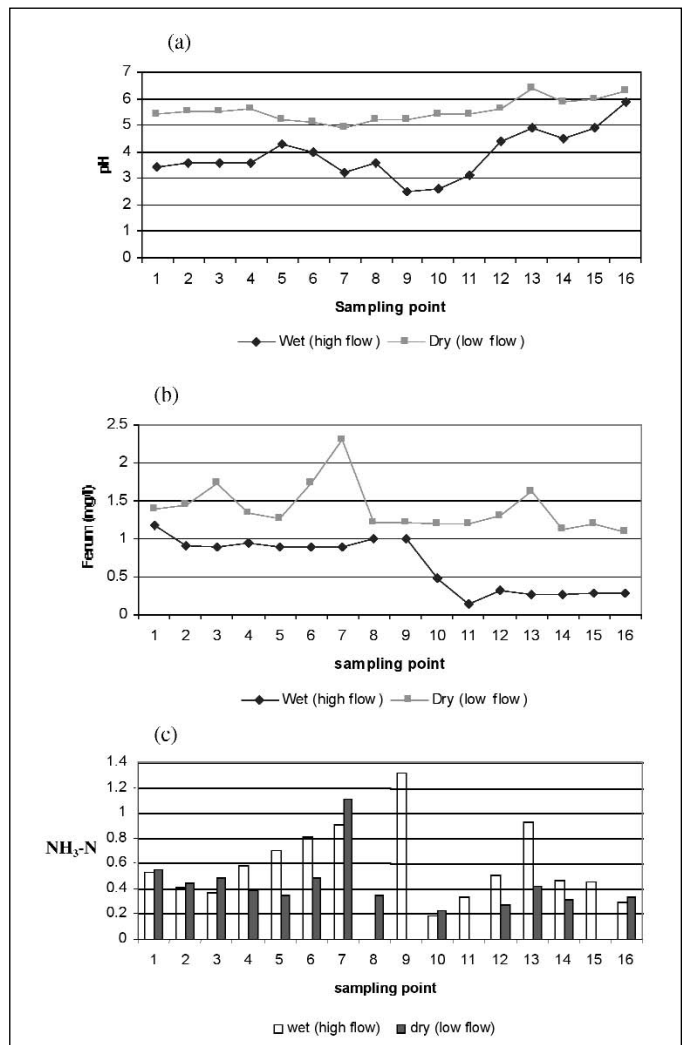
Figure 4 : Means of (a) ph (b) Fe (c) NH_3-N, along Bekok River
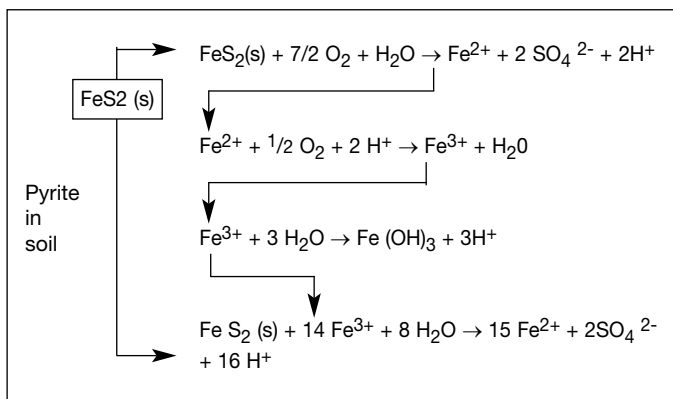
Figure 5. Acidification process of soil by oxidation of pyrite causing the release of free H^+ [1]

The equations shown in the figure:

$$FeS_2(s) + 7/2\ O_2 + H_2O \rightarrow Fe^{2+} + 2\ SO_4^{2-} + 2H^+$$

$$Fe^{2+} + 1/2\ O_2 + 2\ H^+ \rightarrow Fe^{3+} + H_2O$$

$$Fe^{3+} + 3\ H_2O \rightarrow Fe(OH)_3 + 3H^+$$

$$Fe\ S_2(s) + 14\ Fe^{3+} + 8\ H_2O \rightarrow 15\ Fe^{2+} + 2SO_4^{2-} + 16\ H^+$$

Pyrite in soil

FeS2 (s)

Water quality during low and high flow

Figure 4(a) shows the mean *pH* values of the Bekok River during low and high flows. Overall, it is observed that during the high flow, the *pH* value was lower than that during low flow. In other words, the river was more polluted during high flow. This finding is in accordance to the basic principle of non-point sources pollution problem in surface water. In a large agricultural catchment, pollution from nonpoint sources by phosphorus, agricultural organics and some heavy metals is detrimental to the river system. Unlike in urban rivers of point sources problem, the most severe impact for nonpoint sources problem occurred during or following a storm event [9]. Naturally, during the rainy days the soil is wet and may reach near saturated level. The accumulation of the free hydrogen ions in the drained agricultural areas can be explained as follow. The construction of drainage canals in an area of potentially acidic soil will expose more soil surface area. This would further expose the pyrite layer to the air and enhance oxidation process. Consequently, this will increase the amount of hydrogen ion in the soil layer. As illustrated in the chemical reaction in **Figure 5**, further oxidation of Fe^{3+} and FeS_2 through various stages of redox reaction in the soil [1] would end-up with a low soil *pH*. The ions present in the soil profile are then transported into the drainage canal through surface runoff and leaching process as rainwater percolates through the soil profile. In addition, under the gravity flow drainage, surface water in the drains carrying acidic element will eventually flow into the river system. The accumulated *H* ions from various parts of the catchment areas into the river system will eventually decrease the *pH* level of the surface water.

Nevertheless, it would depend on various factors such as sampling timing and techniques as well as the hydro-geographical characteristics of the catchment.

Water quality variation along the river reach

A further analysis was made to examine the variation in the water quality at different river reach. Using the same data, the water quality parameter was regressed against the distance from the intake point, and the results are tabulated in **Table 3**.

From the table, during the low flow only *pH* values was significantly correlated to the distant from the water intake. The coefficient of determination, r^2 of more than 48 percent indicated

a moderately strong relationship between *pH* values and the distance from the intake point. A similar trend was found during the high flow but at a lower initial (intercept) value.

In both cases, the regressions also show that the pH values decreased directly with the distance, *L*. In other words, the river is more acidic toward the lower reaches of the river, close to the water treatment plant intake. This finding is expected as more drained areas be found in the lower part of the catchment. Shallow rooted crops such as vegetables are grown in the locality and these crops require an extensive and efficient drainage system. Unlike in the lower part, the upstream parts of the catchment remain undrained and covered by secondary forest and tree crops.

The correlation analysis between *Fe* and the distance from the water intake, *L*, also gave a good relationship during the high flow. The correlation coefficient of more than 71 percent indicated a strong relationship between *iron-Fe* content and the distance from the intake point. This finding provides a further support to the hypothesis that the hydrogen ion accumulated in the soil profile is more rapidly leached into the river during the high flow.

A multiple regression analysis between *pH* as the dependent variable against $NH_3\text{-}N$ and *Fe* as independent shows a good relationship. The best fitted model was *pH = 4.669 + 0.959 Fe - 1.851 NH₃-N*. The p-values in the ANOVA table is less than 0.01 indicating that there is a statistically significant relation between variables at the 99% confidence level. The physical meaning to this analysis could be that *Fe* and $NH_3\text{-}N$ contents in the surface water contributed significantly to the *pH* value. **Table 4** presents the statistical output from cross-correlation analysis between those three water quality parameters. It is clear that pH is highly dependent on its *Fe* and $NH_3\text{-}N$ level, while $NH_3\text{-}N$ and *Fe* are not significantly correlated.

Water quality in the suspected point source area

To investigate further the effect of agricultural drainage on the receiving surface water, a more detail field investigation was carried out in one of the drained areas. This area was chosen as the authors suspected that it was the pollution point source of the Bekok River. As shown in **Figure 2(d)**, eight sampling points within the area representing different level of drained water were selected. Table 5 summarized the results of the observation.

The results show that the *pH* level of the surface water increase, as it gets closer to the river. In general, the acidity level of the surface water was in the following order; *pH* at field drain (*pH 3.3*) < at tertiary drain (*pH 3.5-3.7*) < at the secondary drain (*pH> 4.0*). For instance the pH values at points inside the field drain i.e. points G and H, were extremely acidic as compared to those at points near the drainage outlets of points C and F. This phenomenon could be explained using the principle of dilution or decaying factor of the dissolved chemicals in the running surface water system. It seems that the *pH* values is positively correlated with the distance from the pollution point source.

Field observations found that areas along 0.5 to 1.0 km from the riverbank were naturally flooded. Owing to the direct contact with the running water (river), these areas are considered the flood plain or riparian zones of the river system. The riparian or flood

Table 3 : Summary of the simple linear regression analysis

Flow	Parameter	Regression equation	r^2	P
Low flow				
	Fe	$Fe = 1.5713 - 0.0205\ L$	16.01	P >0.1 *
	NH_3-N	$NH_3\text{-}N = 0.5243 - 0.0113\ L$	10.01	P >0.1 *
High flow	pH	$pH = 3.0876 + 0.094\ 1\ L$	41.16	P <0.01 **
	Fe	$Fe = 1.0756 - 0.0486\ L$	71.51	P <0.01 **
	NH_3-N	$NH_3\text{-}N = 0.6417 - 0.0068\ L$	2.07	P >0.10 *
L = distance from the intake point in Km; ** significant , * not significant				

Table 4 : Correlations analysis of the pH, Fe and NH_3-N

		pH	Fe	NH_3-N
pH	Pearson Correlation	1.000	**.391***	**-.439***
		.	.027	.012
	N	32	32	32
Fe	Pearson Correlation	**.391***	1.000	.097
		.027	.	.599
	N	32	32	32
NH_3-N	Pearson Correlation	**-.439***	.097	1.000
		.012	.599	.
	N	32	32	32
* Correlation is significant at P ≤ 0.05				

Table 5 : Observed pH values in one of the suspected point source area

Sampling point *	pH	Specific location
A	4.7	At the intersection point between secondary drain and main river
B	4.4	At the intersection point between secondary drain and tertiary drain
C	3.5	At the tertiary drainage outlet box
D	4.7	Same as point B
E	3.5	Same as point C
F	3.7	At the inner site of the tertiary drain
G	3.3	In the field drain
H	3.3	In the field drain
* Referring to **Figure 2(d)**		

Note: – The secondary drain is one of the straightened natural Bekok River tributaries

– The drainage block is provided with an intensive drainage network and covered with mixed crop, mainly banana and Oil palm

plain of a river system is an important part of the physical and biological structure of a healthy river [10]; [13]. Therefore, conservation of these areas is necessary toward a healthier river. The physical structure of these areas is particularly important in agricultural areas where riparian zones can act as nutrient filters between fields and surface waters.

CONCLUSIONS AND RECOMMENDATION

In agricultural watersheds the surface waters generally receive a substantial amount of drainage water from the soil horizon. Field studies have been conducted to investigate the agricultural drainage-surface water interaction. The following conclusion and recommendation could be drawn. The acidity of the river under investigation was generally quite low. The *pH* values at certain

reach of the river were somewhat affected by the soil drainage activities. The oxidation process associated with the drainage activities could have been taken place along the riverbank. The high *Fe* contents in the surface water could be taken as another evidence. Soluble ion in the soil profile resulted from the soil oxidation process could have been transported into the river system thus it caused the surface water to be more acidic. The *NH_3-N* content is relatively small.

This study was simply based on spot water quality samplings and was not according to a proper dynamic modeling design. Therefore, further research is needed to further verify the soil drainage-surface water quality relationship in the study basin. A long-term monitoring of stream water chemistry in relation to the land use change, particularly at the flood plain area of the

catchment is essential. It would provide useful information towards an integrated river basin management in the long run. To be more specific, knowing the changes in soil chemistry of the flood plain area over time would be able to predict the long-term effects of soil chemical changes on important water quality parameters of the receiving water. Such research work is more urgent in catchment areas where their river systems are being utilized for freshwater supply to the domestic water treatment plant.

The findings of the study clearly show that the stream water quality had been affected by land drainage activities of the catchment. Several recommendations are made as part of stream water quality protection program.

- Establishing riprarian zone of the catchment: the riprarian zone is an important interface between the surroundings agricultural land and the stream ecosystem. The riprarian zone controls the interaction between the stream and the surroundings. Besides functioning as nutrient filters and buffer zones between surface waters and agricultural land these zones are important areas for floras and faunas.
- Establishing cropping zone: Crop zoning or right selection of crop to be grown at the stream terrestrials would be able to minimize the acidification processes of agricultural land. If only flood tolerant crop such as aquatic-type of crops are grown, no intensive drainage system is required. As a result, the water table drawdown and soil surface exposure could be minimized and eventually the release of the hydrogen ions in the soil profile can be reduced.
- Soil liming: liming the drained agricultural areas could be another immediate measure to reduce acidity level of the soil, thus the river. Though it would give immediate effect, it requires higher cost and it should be considered as an emergency correcting measure.

ACKNOWLEDGEMENT

REFERENCES

[1] Ahmad, A.R., Wahab, N.A, Kamaruddin, A. and Ting, C.C. (1990). Acidity Amendments and Ccrop Responses to Liming of Malaysian Soils. Special Report, Serdang: MARDI.

[2] Bruinjzeel, L. A. (1993). Land-use and Hydrology in Warm Humid Regions: Where do We Stand? Proceedings of Yokohama Symposium: Hydrology of Warm Humid Regions. *IAHS Publ.* No.216. p:3-35.

[3] Evan, R.O., Gilliam, J.W. ans Skaggs, R.W. (1988). Controlled Drainage Management Guidelines for Improving Drainage Water Quality. Pub.No. AG-443, Cooperative Extension Services, Raleigh : N.C.State Univ.

[4] Henrikson, L., Hindar, A. and Thornelof, E. (1995). Freshwater Liming. *J.Water,Air and Soil Poll*., 85,131-142.

[5] Keizrul Abdullah (1997). Drainage and The Environment: The Need for a Reassessment. Proceedings `7th ICID International Drainage Workshop' 17-21 Nov 1997, Penang, Malaysia.

[6] Lowrance, R.R., Todd, R., Fail, J., Hendrickson Jr., Leonard, R. and Asmussen, L. 1984. Riparian Forest as Nutrient Filters in Agricultural Watersheds. *BioScience*, 34, 374-377.

[7] Malaysian Water Association (1994). Design Guidelines for Water Supply System. Kuala Lumpur: MWA.

[8] Novotny, V. (1995). Nonpoint Pollution and Urban Stormwater Management. Water Quality Management Library, Vol.9. Lancaster:Technomic Publishing.

[9] Novotny, V. and Chesters, G. (1981). Handbook of Nonpoint Pollution Sources and Management. New York: Van Nostrand Reinhold.

[10] Petersen, R.C., Madsen,B.L., Wilzbach, M.A., Magadza, C.H.D., Paarlberg, A., Kullberg, A. and Cummins, K.W. (1987). Stream Management: Emerging Global Similarities., *Ambio*, 16(4),166-179.

[11] Phillips, J.D. (1989). Nonpoint Source Pollution Control Effectiveness of Riparian Forest Along A Coastal Plain River. *J. Hydrol*., 110, 221-237.

[12] Reuss, J.O., Cosby, B.J. and Wright, R.F. (1987). Chemical Processes Governing Soil and Water Acidification. *Nature*, 329(3), 27-32.

[13] Smedema, L.K. and Rycroft, D.W. (1983). Land Drainage. New York: Cornel Univ.Press.

[14] Twort, A.C., Law, F.M. and Crowley, F.W. (1985). Water Supply. 3rd Ed. Kent: Edward Arnold.

ANNOUNCEMENT

Dear Member,

ENGINEERING CAREER ADVISORS

IEM intends to further its contribution to the community by initiating and encouraging its members to promote engineering as a career to science and increase awareness about engineering. Any IEM member living or had been educated in the community can volunteer his services to represent IEM to conduct talks at the school of the member's choice. For further information, please contact IEM Secretariat at 603-79684001/2 or e-mail to **sec@iem.org.my.**

Ir. Dr Tee Tiam Ting
Chairman
Sub-Committee on Engineering Career Advisors

Ultimate Strength of Precast Concrete Sandwich Panel with Opening Under Axial Load

Farah Nora Aznieta Abdul Aziz, Abang Abdullah Abang Ali, Mohd Saleh Jaafar,
Abdul Aziz Abdul Samad and D.N. Trikha
Department of Civil Engineering, Universiti Putra Malaysia,
43400 UPM Serdang, Selangor.

ABSTRACT

A precast sandwich panel which is being developed as a building system consists of a single layer of insulation sandwiched between two layers of reinforced concrete. At present, an equation to predict the ultimate strength of precast concrete sandwich wall panel with opening, to the best of authors' knowledge, is not available. This paper reports a research effort to determine the suitability of the load equations developed by earlier researchers for thin reinforced concrete solid wall with opening when used to estimate the ultimate load of precast concrete sandwich wall panel with opening. Nine sandwich panels with different window and door opening combination were prepared and tested under uniformly distributed load. The load was applied and increased in stages till failure. At each stage of the load, deflection gauges and strain gauges reading were recorded. The development of cracks was also monitored. The experimental ultimate loads of precast concrete sandwich wall panels with opening tested in the laboratory were compared with and found close to the theoretical values derived from the equation proposed by Saheb and Desayi for ordinary precast concrete wall panels with opening.

Keywords : Precast Concrete, Sandwich Panel, Ultimate Load, Concrete Design

INTRODUCTION

Precast concrete components have been widely used in the building sector. The rapid growth of the building industry plus the increasing demand for quality buildings necessitates the building industry to continuously seek improvement, leading to industrialisation in the building industry. The advent of industrial methods had shown that mass production of precast concrete components had increased the quality as well as reduced the cost of construction. Cost reduction is achieved through lesser construction time and amount of labour [1].

Precast concrete is defined as concrete which is cast in some location other than its position in the finished structure. One possible building elements in a precast building system is precast concrete sandwich wall panel. The difference between precast concrete wall panel and precast concrete sandwich wall panel is the presence of an intervening layer of insulation. An opening refers to a void area in the wall. In practice, it can be a door or a window. This paper presents the results of an experimental investigation comparing between the experimental and theoretical ultimate loads of precast concrete sandwich panel with opening under static loading.

Very little information is available on the behaviour of concrete panels with openings. Seddon [2] studied wall panel supported at the top and bottom with a symmetrical opening. His conclusions were as follows:

1. Openings cause beam element behaviour above and below the opening. Portions adjacent to openings in the direction of the load exhibited column element action. It was found that panels ultimately failed through one of the column elements due to the cracks extending to the corners of openings.

2. To fully utilise the concrete strength, there is a need for adequate reinforcement in the beam elements.

Saheb and Desayi [3] realised the need for more detailed information on panels with openings. The authors carried out test on twelve panels; six were supported at the top and bottom only and the others were supported on all four sides. Each panel was provided with a window or a wall opening in different regions. The size of the panels was 600mm high x 900mm long and 50mm thick. The test panels were subjected to in-plain vertical loads applied at an eccentricity. The test panels had identical vertical and horizontal reinforcement ratios, i.e., either r = 0.173 or 0.236, and the concrete strength was set at 28 N/mm^2. The slenderness ratio i.e. the height to thickness ratio was constant at 12, the thickness ratio at 18, and the aspect ratio at 0.67. To prevent premature failure due to cracking at corners, reinforcement was placed at 45 degrees in these areas. The conclusions to these tests were:

1. The failure of the concrete panels appeared to be due to buckling influenced by bending of slender column strips adjacent to the openings.

2. Empirical equations were developed for panels with openings for both one-way and two-way panels by modifying the ACI formula and the introduction of a reduction parameter that allowed for the geometry of the openings.

3. The panels supported on four sides appeared to be slightly stronger than the one-way panels. The cracking load was marginally greater for panels under two-way action. But more importantly, the ultimate load was found to be nearly equal.

In studies on the design of beams (as opposed to walls) with openings, an important consideration is the stress concentration

that occurs due to a sudden reduction in beam cross section. Inadequate reinforcement or improper detailing may lead to wide cracking and even premature failure of the beam. To deal with this stress concentration, Nasser et al. [4] suggested the use of diagonal bars at each corner of the opening and recommended that a sufficient quantity be provided to carry twice the amount of external shear. However, Lorenston [5] and Barney et al. [6] suggested the use of stirrups in the solid section adjacent to each side of the opening. These stirrups should be designed to carry the entire shear force, but without any magnification.

The PCI Committee [1] report on Precast Concrete Sandwich Panel defined the openings as being completely contained within the panel or as blockouts in the panel sides, top or bottom. Panel openings should have re-entrant corners reinforced with diagonal bars in both layer to limit the width of corner cracks. Punched opening located near one edge of the panel are very susceptible to cracking and it is advisable to eliminate the insulation in this area and reinforce the side with additional reinforcement.

Previous research work on panel with opening was very limited. Only Saheb and Desayi [3] had suggested an equation to calculate the ultimate load of reinforced concrete wall panel with opening. In order to compare the experimental ultimate load with the theoretical value, the Saheb and Desayi [3] equation for panels with opening was used to estimate the theoretical load as follows:

$$P_{uoc}^c = (k_1 - k_2\alpha)P_c^{cu} \tag{1}$$

where, P_{uc}^c is the theoretical ultimate load for panel without opening, which is given by:

$$P_{uc}^c = 0.55\phi \left[A_g f_c' + (f_y - f_c')A_{sv}\right]$$
$$[1-(H/32t)^2][1.2-H/10L] \tag{1b}$$

and $\quad k_1$ *and* k_2 *= constant*
$\quad\quad A_g \quad\quad$ *= gross area of the wall panel section*
$\quad\quad A_{sv} \quad\quad$ *= area of vertical steel in wall section*
$\quad\quad f_c' \quad\quad$ *= cylinder strength of concrete*
$\quad\quad f_y \quad\quad$ *= yield strength of steel*

$\quad H, L \quad\quad$ *= height, length of wall panel*
$\quad t \quad\quad\quad$ *= thickness of the wall*

The influence of size and location of the opening(s) was taken into account through the parameter a, where

$$a = \frac{A_o}{A} + \frac{a}{L} \tag{2}$$

Where

$\quad A_o \quad = \quad L_o t$
$\quad A \quad = \quad Lt$
$\quad a \quad = \quad \left[(L/2) - \bar{a}\right]$
$\quad \bar{a} \quad = \quad \dfrac{(L^2 t/2 - L_o t a_o)}{Lt - L_o t}$

$\quad Lo \quad = \quad$ *length of panel opening*
$\quad ao \quad = \quad$ *distances of the centres of gravity of the opening from the left edge of the panel*
$\quad \bar{a} \quad = \quad$ *distances of the centres of gravity of the panel without opening from the left edge of the panel*
$\quad a \quad = \quad$ *distance between centres of gravity of panels with and without opening*

METHODOLOGY

Test Specimen

In this study, three types of precast concrete sandwich panels were designed and classified as: -
- Precast concrete sandwich panel with door opening;
- Precast concrete sandwich panel with window opening; and
- Precast concrete sandwich panel with door and window opening.

A total of nine test specimens were prepared; three specimens each for the three types. The panels were named as OA, OB and OC for panels with door opening, panels with window opening and panels with both door and window openings, respectively. Number 1, 2 and 3 were designated to the three specimens in

Table 1: Test Specimen Details

Type of specimen	Specimen No. (h x w x t) mm	Size of panel (h x w) mm	Size of opening (h x w x t)		No. of Shear Connector	Column size (h x w x t) mm
			Door	Window		
With door opening	OA1 OA2 OA3	900 x 1000 x 120	700 x 300	-	4@ 200mm c/c	900 x 100 x 120
With window opening	OB1 OB2 OB3	900 x 1000 x 120	-	460 x 400	5@ 200mm c/c	-
With door and window opening	OC1 OC2 OC3	900 x 1000 x 120	700 x 300	360 x 400	6@ 200 mm c/c	900 x 100 x 120
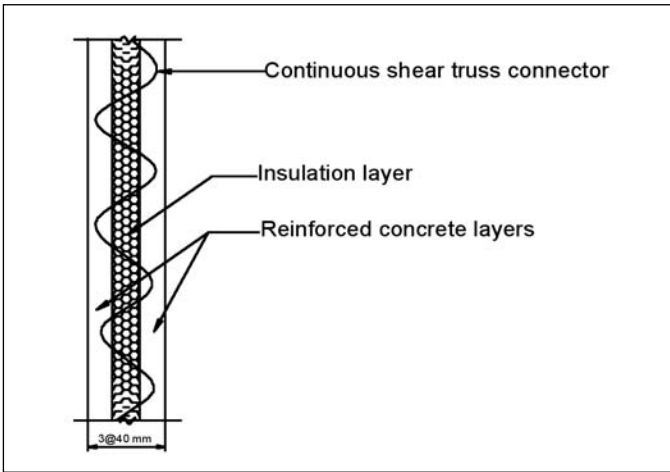
Figure 1 : Sandwich Panel Layers

Figure 2(b) : Panel With Window Opening (OB)

each type. The specimen size was 900mm x 1000mm by 120mm thick. Table 1 shows the details of the specimens. The thickness of the sandwich panel was made of two 40mm layers of concrete and a layer of insulation material in between. The two concrete layers were connected through the insulation layer by continuous shear truss connector along the length of the panel (Figure 1). The shear truss connectors were located at every 200mm centre to centre across the width of the panel.

The precast concrete sandwich panel with door opening (OA) was prepared with a door opening of 700 x 300mm. Figure 2(a) shows the door position as well as the locations of steel reinforcement. The small area of concrete next to the door opening was designed as a column to prevent failure at that area. Four 6mm diameter bars were used as reinforcement. At the edge of the opening, two diagonal bars were placed at both concrete layers. The diagonal bars were placed at 45° to the opening edge.

The precast concrete sandwich panel with window opening (OB) had an opening 270mm from the bottom of the panel. The opening was designed at the centre of the panel. The size of the window opening was 460 x 400mm. The diagonal bars were placed at the four corners of the opening in both concrete layers. The detailed drawing of the panel is as shown in Figure 2(b).

The precast concrete sandwich panel with door and window opening (OC) have 700 x 300mm door and 360 x 400mm window

Figure 2(c) : Panel with Door and Window Openings (OC)

openings. Diagonal bars were placed at every corner of the openings in both concrete layers. Similar to the panel with door opening, in order to prevent failure, the small area of concrete near the door opening was designed as a column. Figure 2(c) shows the details of this panel.

Materials

A ready mix concrete with a mix ratio of 1: 2.22: 2.46 and a water-cement ratio of 0.57 by weight was used. The maximum size of aggregate was 10mm. The concrete was designed for 28-day cube strength of 30 N/mm². Concrete compression test was carried out on 150mm cubes at concrete age of 28-days to obtain the concrete compression strength.

6mm diameter mild steel bars were used for vertical and horizontal reinforcements. The percentages of vertical and horizontal reinforcements used were 0.12 and 0.2 percent of gross concrete area respectively. This was based on ACI 318-83 Section 14.3.2 and 14.3.3 (minimum vertical and horizontal reinforcement in reinforced concrete wall); applied to steel bar diameter less than 16mm with the specified yield strength not less than 413.7 N/mm². The maximum allowable spacing of reinforcement in wall according to Section 14.3.5 for vertical and horizontal reinforcement was three times the wall thickness or 457mm whichever was less. BRC bars with 200 x 200mm opening were

Figure 2(a) : Panel with Door Opening (OA)
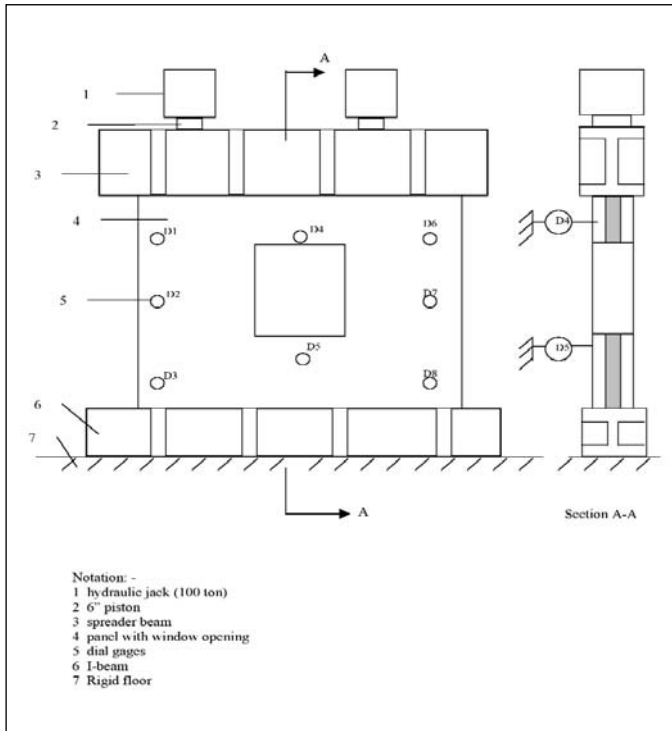
Figure 3 : Schematic View of the Test Frame (back view)

used as reinforcement mesh in both concrete layers.

For continuous shear truss connectors, the 6mm mild steel bar was bent to an angle of 60° (against horizontal plane) with a height of 90mm. The continuous shear truss connectors were placed at 200mm centre to centre along the width of the panels. Premature failure may occur at two critical areas; the corners of the opening and the small width adjacent to the door opening. In order to prevent this, the corners of the opening were reinforced with 6mm diameter bars placed diagonally at 45° to the corners and a concrete column with four 6mm diameter bars provided at the small width next to the door opening.

In this investigation, polystyrene was used as insulation material because it has good thermal resistance, economical and easy to acquire from the local market. The insulation material chosen depends upon the thermal properties of the material, the design temperature of the structure and the desired thermal resistance of the panel.

Test Setup

For the experimental test, the panels were placed vertically and simply supported at the top and bottom as shown in Figure 3. This allows for the rotation at the support, but restrains horizontal and/or vertical displacement. The horizontal movement was restrained by the top support. The panels were subjected to uniformly distributed load, applied through a spreader beam. The horizontal levels of the panel and spreader beam were checked prior to loading. Two hydraulic jacks with 100-tonne capacities each applied the load in stages up to failure. The hydraulic pressure recorded on the pump meter controlled the load applied to the panel. The calibration factor of the pump was 0.85. At every 53.3kN increment, the load was kept constant for a while to allow the panel to stabilise before the strain gauges and deflection dial gauges readings were recorded. The ultimate loads and the crack patterns were also recorded.

RESULTS AND DISCUSSION

Material

The average compressive strength (f_{cu}) of the concrete cubes recorded from the compression tests was 35.2N/mm^2. The equivalent compressive strength of concrete cylinder (f_c') was taken as 0.85f_{cu} or 29.9N/mm^2.

As for the steel, the tensile test was carried out on three samples of 6mm diameter BRC bars and three samples of 6mm diameter mild steel bars as the shear connector. The average yield strength (fy) of the BRC bars and the shear connector was 572.9N/mm^2 and 546.8N/mm^2 respectively.

Ultimate Load Analysis

In the ultimate load calculation, the thickness of an insulation layer was not taken into consideration. The total effective thickness of the panel was taken as 80mm. Loads at first crack were about 28% to 74% of the ultimate loads. Panels with door opening had the first crack at 54% to 74% of ultimate loads. Panels with window opening had its first crack at 30% of ultimate load. The first crack for panels with door and window opening occurred as early as 28% of its ultimate load. This showed that, the panels with door and window opening had the earliest crack when compared to the other types of panel. The strain gauges and dial gauges readings were also recorded during the experiments but not presented in this paper. The ultimate loads and the crack patterns were also recorded.

Table 2 tabulated the values of α and experimental ultimate load of panels with opening to theoretical ultimate load of panel without opening (P_{uo}^e / P_{uc}^c). The theoretical ultimate load of panel without opening (P_{uc}^c) was taken as 1363kN. This value was calculated using Saheb and Desayi for panel without opening equation. The strength reduction factor (f) is taken as 1 in order to compare with the actual ultimate load.

Values of parameter α and P_{uo}^e / P_{uc}^c c from Table 2 were plotted as in Figure 4. The values of k1 and k2 are 1.0027 and 0.779 respectively, were calculated from the best-fit linear line of graph in Figure 4. By using equation 1, the theoretical ultimate loads were compared to the experimental values.

Table 2: Analysis of Panel With Opening

Type of panel	No. of panel	$\dfrac{A_o}{A}$	$\dfrac{a}{L}$	α	P_{uo}^e (kN)	P_{uo}^e / P_{uc}^c
With door opening	1				951.3	0.70
	2	0.3	0.116	0.416	996.6	0.73
	3				860.7	0.63
With window opening	1				724.8	0.53
	2	0.4	0	0.400	1177.8	0.86
	3				906.0	0.66
With door and window opening	1				634.2	0.47
	2	0.7	0.026	0.726	634.2	0.47
	3				498.3	0.37
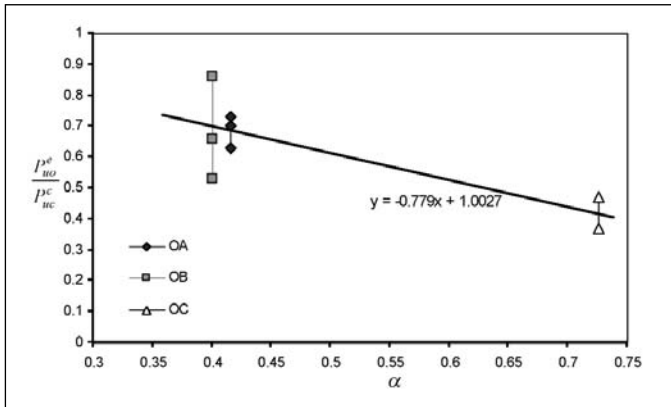
Figure 4 : P_{uo}^e / P_{uc}^c verses α

Table 3 shows the ratio of experimental to theoretical ultimate loads of panel with opening varied from 0.77 to 1.25. The panels with door opening (OA) showed one panel having a 7% lower experimental value compared to the theoretical value. For panel with window opening (OB), two panels had lower values (23% and 4%) than the theoretical while for panels with door and window openings (OC) only one panel showed a lower value of 16%.

The average ratio of experimental ultimate loads to the corresponding theoretical values varies from 0.99 to 1.01 for the three types of panel with opening. This showed that the theoretical equation by Saheb and Desayi [3] for ordinary reinforced concrete wall with opening could be used to estimate the ultimate load for sandwich panels with opening.

CONCLUSIONS

The theoretical ultimate loads were calculated using Saheb and Desayi [3] equation for ordinary reinforced concrete wall with opening. The calculations were made with an assumption that the total thickness of the sandwich panel is equal to the total thickness of the two reinforced concrete layers only. After analysing the experimental data, the average ratios of

experimental to theoretical ultimate loads for sandwich panels were found to vary between 0.99 and 1.01. This shows that the ultimate load equation for ordinary reinforced concrete wall with opening proposed by [3] can be used to estimate the ultimate load of precast concrete sandwich wall panels with opening.

REFERENCES

[1]   PCI Committee. State-of-the-Art of Precast/Prestressed Sandwich Panels, *PCI Journal, Vol. 41,* No. 2, pp. 92-134,1997

[2]   Seddon, A.E. Strength of Concrete Walls under Axial and Eccentric Load; Symposium – Strength of Concrete Structures, Cement and Concrete Association, London, May 1956.

[3]   Saheb, S.M.; Desayi, P. Ultimate Strength of RC Wall Panels With Opening, J*ournal of Structural Engineering (ASCE), Vol.116,* No. 6, pp. 1565 – 1578, 1990.

[4]   Nasser, K.W, Acavalos, A. and Danial, H.R. Behaviour and Design of Large Openings in Reinforced Concrete Beams, *ACI Journal Proceedings, Vol. 64,* No. 1, pp. 25-33, 1967.

[5]   Lorenstan, M. Holes in Reinforced Concrete Girders, *Byggmastaven (Stockholm), Vol. 4,* No. 7, pp.33, 1962. Also, Informal Report translated by Portland Cement Association, pp.141-152.

[6]   Barney, G.B, Corney, W.G, Hanson, J.M. and Parmelee, R.A. Behaviour and Design of Prestressed Concrete Beams with Large Web Openings, *Journal Prestressed Concrete Institute, Vol. 22,* No. 6, pp. 36-61, 1977.

Table 3 : Theoretical and Experimental Ultimate Loads for Panels With Opening

Panel No.	Experimental ultimate load P_{uo}^e	Average experimental ultimate load P_{uo}^e (ave)	Theoretical ultimate load P_{uo}^c	Experimental/ theoreticald ultimate load P_{uo}^e / P_{uo}^c	Average experimental/ theoretical ultimate load P_{uo}^e (ave) / P_{uo}^c
OA1	951.28			1.03	
OA2	996.59	936.19	924.98	1.08	1.01
OA3	860.69			0.93	
OB1	724.79			0.77	
OB2	1177.79	936.19	941.97	1.25	0.99
OB3	905.99			0.96	
OC1	634.19			1.06	
OC2	634.19	588.89	595.83	1.06	0.99
OC3	498.29			0.84	

Synergistic Systems for Spacecraft Attitude Control

Renuganth Varatharajoo, Aznijar Ahmad Yazid, Mohd Ramly Ajir
Spacecraft System, Department of Aerospace Engineering, Universiti Putra Malaysia
43400 UPM Serdang Selangor.

ABSTRACT

The synergistic system design could be an attractive approach for future spacecraft to cope with their demands. The idea of combining the Attitude Control System and the conventional Electrical Power System is presented here. In this article, the Combined Energy and Attitude Control System (CEACS), a double counter rotating flywheel assembly in the pitch axis, is investigated for small satellites. The performance of CEACS is demonstrated for a selected configuration and mission. Another idea of incorporating the Attitude Control System into the Thermal Control System is also investigated. The Combined Attitude and Thermal Control System (CATCS)* consisting of a "fluid wheel" and permanent magnets, couples an existing onboard temperature gradient with the magneto-hydrodynamic (MHD) effects for its operation. The performance of CATCS is demonstrated for a reference configuration and mission. The CEACS and CATCS are potential synergistic systems for the future spacecraft.

Keywords : Flywheel/fluid wheel/spacecraft attitude control

INTRODUCTION

Synergisms for spacecraft describe the linking or merging of different subsystems in order to achieve a better overall performance, e.g. in reliability, mass saving or even for enabling a certain mission. In coming years, the projected power requirements for space missions will be increasing. With the current energy densities (5-20 Wh/kg), the conventional energy storage system (electrochemical battery) could most probably be insufficient to handle this task [1]. Therefore, having reasonably high energy densities (60 Wh/kg), the flywheels are proposed as the alternative energy storage device for the future spacecraft. These flywheels can also simultaneously serve as attitude actuators in the spacecraft, forming a "Combined Energy and Attitude Control System" (CEACS). Additionally, mass savings could also be achieved by such systems [2]. This concept has been proposed for bigger platforms in recent years, e.g. the International Space Station (ISS) [3]. In the present article, the idea is investigated for the small satellites. Generally, the CEACS should consist of a double counter rotating flywheel assembly, magnetic bearings, motor/generator units, and control electronics for the energy/attitude management.

Another possible synergistic effect for future spacecraft could be generated by the coupling of the thermal and attitude control systems, eventually having a "Combined Attitude and Thermal Control System" (CATCS). In a spacecraft that requires an active thermal control, an electric conducting fluid system could be used for the thermal and attitude control. Such a system would make use of the thermoelectric effects generated by the available onboard temperature gradient, and the magnetic fields from the permanent magnets for its operation. Thus, an excess onboard heat could be used by the CATCS for the spacecraft attitude and thermal management. Consequently, the power budget for these tasks could be suppressed.

This article is organized in the following manner: First, the miniaturisation design principle is viewed generally to verify the possibilities of down scaling the conventional flywheels for CEACS. Second, in section 3, the CEACS power/attitude architecture is presented along with the required transfer functions. Its performance is analysed through numerical treatments and is presented in section 4. In section 5, the CATCS is introduced together with its governing equations. The principal investigation in determining the capability of this system as an attitude actuator is by the determination of its response time. Thus, in section 6, the transient analysis is formulated. The performance analysis follows for the CATCS in section 7. In the final section, the conclusion for this study is drawn.

MINIATURISATION DESIGN PRINCIPLE

Generally, the conventional reaction or momentum wheels for

Table 1 : Satellite Dimension

Satellite Mass [kg]	Satellite Dimension [m]
2	$0.1 \times 0.1 \times 0.1$
10	$0.22 \times 0.22 \times 0.22$
50	$0.6 \times 0.6 \times 0.6$
100	$1 \times 1 \times 1$

-Flywheels' masses: 20 % of the satellite's mass.

-Flywheel size: X % of the satellite's dimension.

-$t_{eclipse} = 36$ minutes.

-Satellite mass $m \approx$ Satellite power P (empirical).

-$\Omega_{max} = \sqrt{\dfrac{2 P t_{eclipse}}{I_W}}$
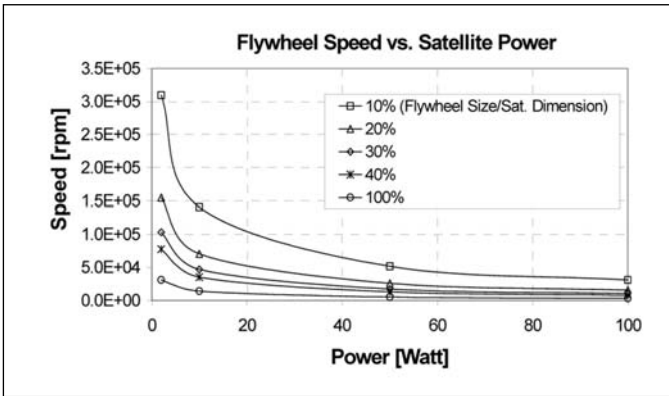
Figure 1: Requested speeds for each flywheel.

Figure 2: A single flywheel speed control loop

bigger satellites could be miniaturised for the small satellite applications. However, the CEACS's flywheel dimension is governed by the power requirement, mass and volume of a satellite. An overview on the relationship is envisaged based on the assumptions in Table 1.

The maximum requested flywheel speed Ω_{max} becomes the crucial parameter for CEACS. Figure 1 shows the quested relationship for different satellites. It can be seen that the flywheel speed increases drastically with the decrease in its size. This indicates that miniaturising the conventional flywheels for CEACS would result into very high rotational speeds. Therefore, the CEACS's flywheel dimension for small satellites should be increased to achieve higher inertia. Eventually, the operating flywheel speed could be suppressed between 40 000 rpm and 60 000 rpm. Moreover, this speed range is achievable with the currently available technology and is sufficient for the small satellite missions [4].

Composite rotors are mandatory for CEACS as they are very much stronger than metal rotors at high speeds. The design of such rotors can be implemented according to Kirk and Sung [5, 6]. Both investigators have focused mainly on the stress analysis for composite rotors. The dynamic analysis (rotor natural frequency) was not described in their investigations. For the small satellites (e.g. <120 kg), single layer composite rotors are found to be able to sustain the stresses (longitudinal and transverse), and to satisfy the energy requirements at about 50 000 rpm. The strength of these rotors can be further increased by using multi-layer configurations [5, 6]. As a result, the rotors can be operated at higher speeds so that their mass budgets could be further reduced. It has been found that even though the strength of the rotors can be increased, their dynamic behavior (eigenvalues) remains to be critical in the high-speed regimes [7]. The performed numerical treatments with a finite element software (ANSYS™) also revealed that the first natural frequency still appears around 50 000 rpm even with the multi-layer rotors. This is due to the thin structure/dimension of the rotors. This dimension could not be drastically altered as it is optimized corresponding to the mass allocation of the rotors. Therefore, the use of a single layer rotor is retained, and it is found to be sufficient for the small satellites.

CEACS CONTROL ARCHITECTURE

The CEACS control design can be implemented either based on the speed controlled mode or the torque controlled mode. The speed controlled mode is selected herein to minimise the steady state sensitivity of possible torque gain errors, especially coming from the differences in the flywheels' inertias and motor/generator constants.
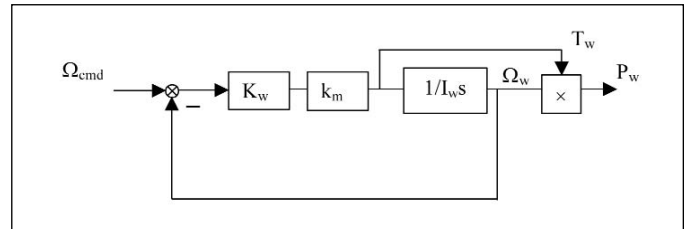
Figure 2 shows the speed control loop of a single flywheel system. From Figure 2, the transfer functions for the resulting speed Ω_w and the exerted torque T_w on a satellite are

$$\frac{\Omega_w}{\Omega_{cmd}} = \frac{K_w k_m}{K_w k_m + I_w s} = \frac{1}{1 + \tau_w s} \tag{1}$$

$$and \qquad \frac{T_w}{\Omega_{cmd}} = \frac{I_w s}{1 + \tau_w s}. \tag{2}$$

The transfer function for the output power P_w corresponding to the input speed command Ω_{cmd} is

$$\frac{P_w}{\Omega_{cmd}} = \frac{T_w \Omega_w}{\Omega_{cmd}} = \frac{I_w s \Omega_w}{(1 + \tau_w s)}. \tag{3}$$

In Figure 2 the flywheel friction term is neglected as the magnetic bearing is used for supporting the rotor. Nevertheless, some other energy losses (e.g. iron losses: eddy-current, hysteresis, etc.) will be macroscopically included in the global charge/discharge efficiency of the system. Additionally, the vacuum compartment for CEACS omits the presence of air drag/friction on the flywheel.

In this investigation, the time constant chosen for the speed control loop is $\tau_w = 2\,s$, and for the motor/generator constant, which gives a proportional relation between the control current and resulting torque, $k_m = 1$ is assumed. As the torque T_w is exerted on the satellite body, an identical counter-rotating partner must be employed to compensate for the torque produced during the charging and discharging phases. The architecture for a double flywheel is presented in Figure 3.

From Figure 3, the transfer function for the total system power P_{system} with respect to the torque energy command $T_{energy.cmd}$ is

$$\frac{P_{system}}{T_{energy.cmd}} = \frac{K_1 I_{w1} \Omega_{w1}}{(1 + \tau_{w1} s)} + \frac{K_2 I_{w2} \Omega_{w2}}{(1 + \tau_{w2} s)}, \tag{4}$$
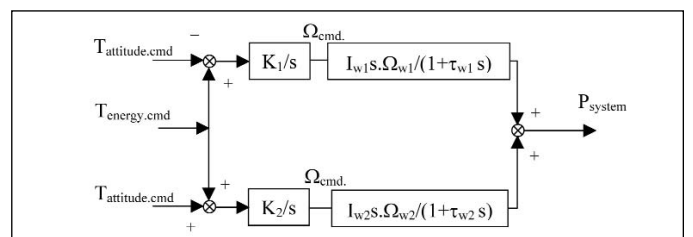
Figure 3 : A double flywheel power loop
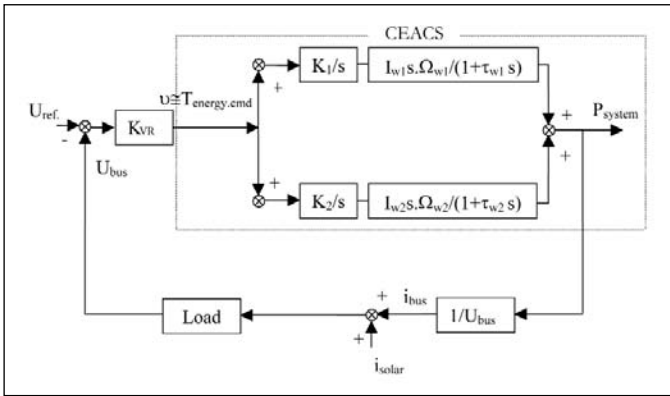
Figure 4: Power management by CEACS

where, for an ideal system, $I_{w1} = I_{w2} = I_w$, $\tau_{w1} = t_{w2} = t_w$, and $K_1 = K_2 = K$. Further, the integrators' gains in this analysis are set to one, thus $2KI_w = 1$.

The CEACS can be integrated on the satellite bus as shown in Figure 4. This design offers a tightly regulated bus voltage. Moreover, a bus voltage regulator KVR can be used to determine the charging and discharging phases without an additional switching equipment. As soon as the bus voltage U_{bus} gets higher than the bus reference voltage U_{ref}, a positive torque command by the regulator will result into a charging operation. In the case that U_{bus} drops below U_{ref}, a negative torque command will discharge the flywheels. In this investigation, the nominal bus reference voltage is assumed to $U_{ref} = 28\ V$.

On the other hand, the attitude control loop can be implemented as shown in Figure 5. By introducing a filter $F(s)$ in Figure 5, the transfer functions developed are valid for the single (angle θ_{sat}) and double (including angle rate ω_{sat}) attitude feedbacks. As shown in Figure 3, the desired attitude control torque is achieved by slowing-down one flywheel and speeding-up its counter rotating member. The attitude controller selected for this application is a Proportional-Derivative (PD) type, which shows good agreements with the stability aspects. Setting the integrators' gains equal to one in Figure 3, and assuming that the flywheels are identical, the dynamics for this attitude actuator is

$$\frac{T_S}{\upsilon} = \frac{1}{1+\tau_w s} \ .$$ (5)

As a result, the transfer function for the satellite's dynamics in Figure 5 yields

$$\frac{\theta_{sat}}{\theta_{ref}} = \frac{1}{1+\frac{K_D}{K_P}s+\frac{I_{sat}}{K_P}s^2+\frac{I_{sat}\tau_w}{K_P}s^3} \ ,$$ (6)

where $\quad F(s)$ is $\quad \dfrac{1}{1+(K_D/K_P)s}$.
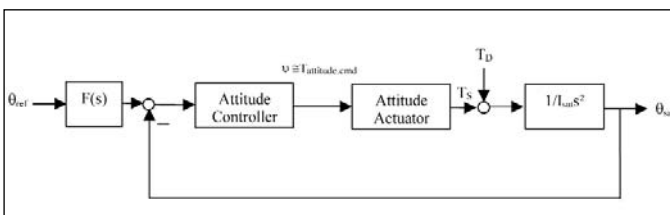
Figure 5: Attitude Control Architecture

CEACS PERFORMANCE

To facilitate the evaluation procedure, a reference mission is chosen as below:

- Mission duration: 5 years.
- Circular orbit at 500 km with an inclination of 53°.
- Period: 95 minutes with 36 minutes of eclipse.
- Satellite mass: 100 kg for 1 m³ of volume.
- Attitude accuracy: Pitch (Y) < 0.2°.
- Maximum external disturbance torque $T_{D.pitch} = 6.15 \times 10^{-5}$ Nm.
- Power requirement: 98 W.

The optimised rotor inertia I_w for this mission is about *0.0155 kgm²*, which corresponds to the inner and outer radii of *0.1137 m* and *0.1430 m*, respectively. On the other hand, the selected proportional and derivative attitude control gains are $K_P = 0.0252$ *Nm/rad* and $K_D = 0.9489$ *Nms/rad*, respectively. The closed loop poles are in the left side of the imaginary axis; hence, the system is stable. In addition to that, this particular mission is assumed to be a bias momentum stabilised type. Therefore, the CEACS is also requested to provide about *6 Nms* of bias momentum or a minimum bias speed of about *400 rad/s* along the pitch axis. The evaluation starts for an ideal CEACS considering only the external disturbance torques acting on the satellite. The initial speed for one of the flywheels was set to *1000 rad/s* in the numerical simulation using Matlab^{TM}. The charge/discharge efficiency for the flywheels was kept to about *80%* [4]. And, a depth of discharge (DoD) of about *90%* was maintained for the operational reasons. In Figures 6 (a) and (b), the flywheels' speeds increase during charging and decrease during discharging operations as expected. These results justify that the flywheel speed range posited in section 2 is hence suitable (below 50 000 rpm). Figure 6 (d) shows that the energy demanded ($\approx$ *60 Wh*) during the eclipse phase is fulfilled by the system. Additionally, the attitude accuracy and the bias momentum remain within their budgets, see Figures 6 (e) and (c), respectively.

The second test case is for a non-ideal CEACS. The identified internal gain errors, which disturbance the system, are from the relative differences in motor/generator constants and flywheels' inertias. On the other hand, the relative misalignment (e.g. *0.1°*) has an impact on the transverse axes of the flywheels' rotational axis; however, this can be overcome with the recent technology advances in the magnetic bearings [4]. Therefore, the system was tested for a relative motor/generator constant difference of *0.5%* and a relative difference in flywheels' inertias of *0.2%* [2]. Figure 6 (f) shows the impact of these errors, which causes the attitude accuracy to exceed its pointing budget. However, the attitude improved after the control loop stiffness was tightened accordingly, see Figure 6 (g). The CEACS shows good performance for the reference mission.

THE CATCS

The basic idea to combine the thermal control system and the attitude control system is by utilizing an electrical conductive fluid, which circulates in a closed loop to serve as a "heat conductor" and a "momentum generator". Thus, the conventional heat pipes

Figure 6: CEACS Performance

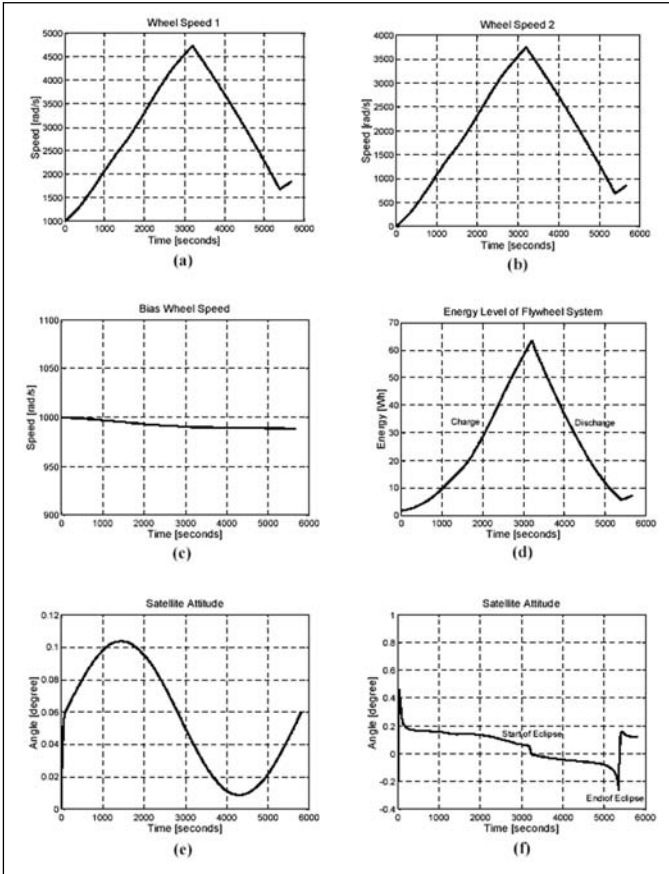could be replaced by a duct system in which the fluid with a reasonable heat transfer coefficient circulates, and simultaneously generates reaction torques for the attitude control. The fluid motion could be influenced by a variation of the external and internal effects, e.g. electric and magnetic fields, and temperature gradients. The concept makes use of the existing temperature gradient in satellites to create a flow through the coupling of the thermoelectric and magnetic fields. The thermoelectric current can be generated by the temperature gradient between metal pairs. Hence, when a magnetic field is introduced near the generated electric current, a fluid flow is induced.

Two configurations are proposed for CATCS, see Figures 7 (a) and (b). The former benefits from the internal heat sources (payloads) and the latter benefits from an external heat source (Sun). These configurations allow an active heat dissipation to the neighboring satellite walls, which will eventually avoid thermal stresses on the satellites. Additionally, this method is independent from the natural convection phenomena, and enhances the heat transport activity. In both configurations, the fluid velocity is controlled by varying the distance between the permanent magnets and fluid housing. This task can be executed by engaging the linear motors to position the magnets [8]. The system details are given in Figure 7 (c). The working fluid selected is gallium, which has a melting point at *303 K*. In fact, this value can be easily dropped by adding the indium (*24%*) and tin (*16%*) compounds [9]. The thermoelectric generator selected as an example is cobalt with an absolute thermoelectric power ΔS of about *-35 µV/K*. Since the liquid-metal gallium is active towards cobalt, the stainless steel is chosen for the fluid housing. Both the

materials, gallium and stainless steel, have no absolute thermoelectric powers, but they are reasonable electric and heat conductors. And, the permanent magnets chosen for the setup are Neodymium-Iron-Boron ($Nd_2Fe_{14}B$) type [10].

The crucial parameter to be estimated first is the maximum fluid velocity V_{max}. The working principle of this system is that the pressure drop due to the duct friction Δp_{loss} must be balanced by the total pressure of the MHD pumps $n\Delta p_{pump}$. Therefore, the Bernoulli's equation for this closed fluid system yields

$$\Delta p_{loss} = n \Delta p_{pump}. \tag{7}$$

The equivalent pressure provided by a MHD pump is induced by the Lorentz force ($F_L = b\,i\,B$) over a cross section ($A = h\,b$).

$$\Delta p_{pump} = \frac{F_L}{A}. \tag{8}$$

Another required parameter to be calculated is the generated thermoelectric current i_{local}, which can be estimated with the following equation,

$$i_{local} = \sigma_{ec} \frac{A_e}{b} \Delta S \,\Delta T, \tag{9}$$

where the cross section A_e is: the mean circumference of duct l_f times height h. It is assumed that a MHD compartment has a particular length $l_f \approx 0.05\ m$. Subsequently, the estimated current is about *80 A* corresponding to an assumed system temperature gradient ΔT of *50 K*. For the magnetic flux density *B = 0.5 T*, eq. (7) yields for the maximum fluid velocity V_{max} = *1.07 m/s*. As a result, the corresponding angular momentum is about *0.95 Nms*. Since the CATCS will be used as "fluid reaction wheel", the quest for its response time will be the prime analysis as reflected in the next section.

TRANSIENT RESPONSE

The CATCS consists of the MHD and classical fluid flows (see Figure 6), which will be characterised respectively in the following. For the reference case, the Hartmann number *Ha >>1*. Thus, the Hartmann flow and MHD Couette flow solutions show the velocity and current variations are localised in a very thin layer (close to the wall), whose thickness is of the order of *h/Ha* [11]. Hence, the system's time response is dominated by the evolution of the core velocity V_θ in the core region. Taking into account the Hartmann properties and the current density in the core region for parallel flows, the Navier-Stokes equation can be solved for the core velocity. In seeking an analytical solution to the transient response, the convection, pressure, viscosity and gravity terms are neglected. The solution for the core velocity in Laplace form yields.

$$V_\theta(s) = \frac{I}{2l_\theta \sqrt{\sigma_{ec}\,\rho\,v}} \left(\frac{1}{1 + (\frac{h^2}{v\,Ha})s} \right). \tag{10}$$
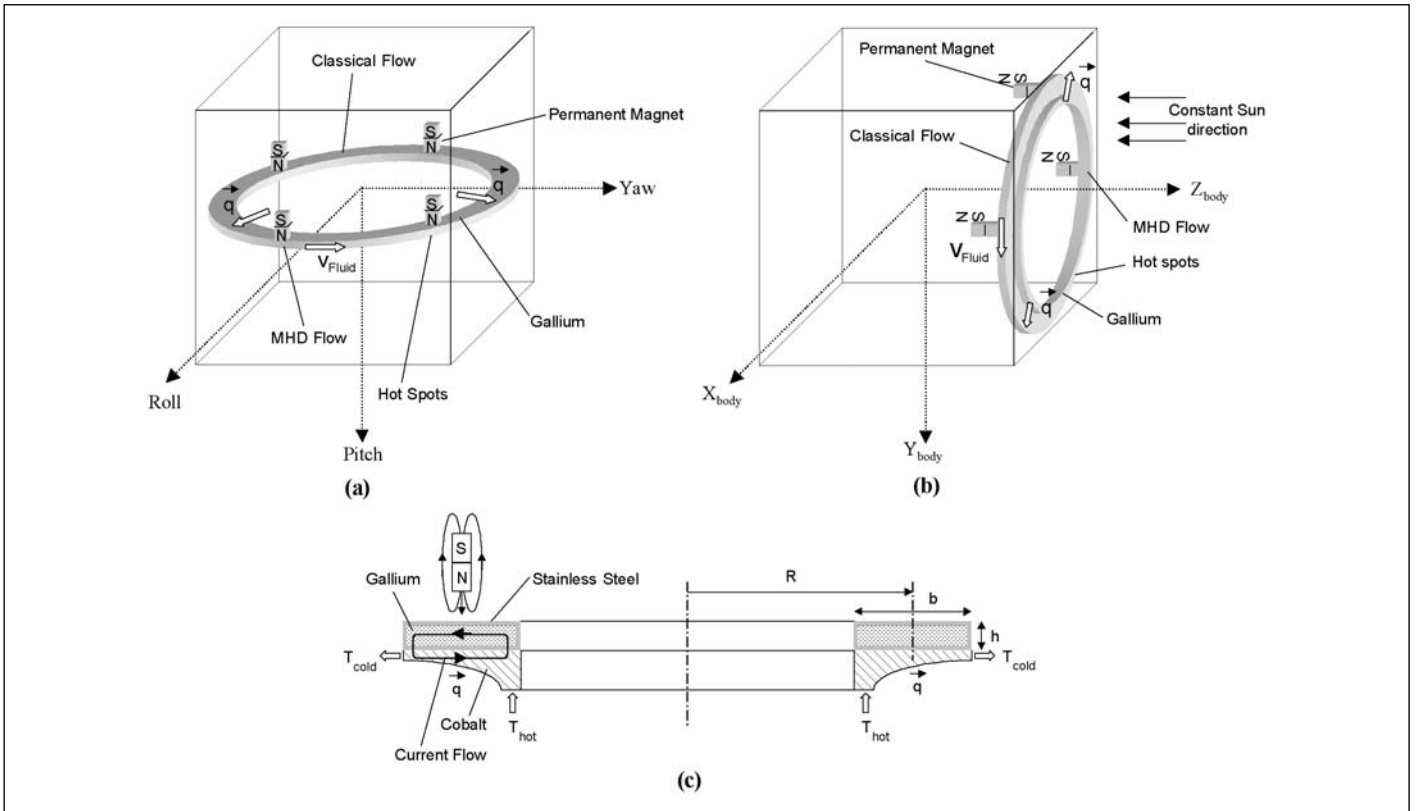
Figure 7 : CATCS Configuration. Setup details: Radius R = 0.5 m, height η = 5 mm, width b = 20 mm, mass μ = 1.86 kg, number of MHD pumps η = 4, fluid inertia If = 0.46 kgm^2, and heat flow q

The core velocity has an exponential function with a response time τ_{mhd} of $h^2/\nu Ha$. For the reference configuration, the estimated time constant is τ_{mhd} = 0.68 s. In order to determine the response time of the complete system, this transient analysis is continued for the classical fluid flow.

The final pressure of the MHD pumps p_{final} must balance the friction pressure drop in order to achieve the intended fluid velocity V_{final}. Therefore, the transient flow can be expressed in the following

$$\frac{\partial V}{\partial t}\rho l = p_{final}\left(1 - \frac{V_{ins}^2}{V_{final}^2}\right), \quad (11)$$

where V_{ins} is the mean instantaneous fluid velocity. Applying the boundary conditions, V_{ins} = 0 at t = 0, and noting that the exponential velocity profile attains *99%* of the V_{final} in a finite time, this equation yields for the quested response time.

$$\tau_{cls} = 2.646\frac{\rho\, l V_{final}}{p_{final}}. \quad (12)$$

The response time solves to τ_{cls} = *1.2 s*. Thus, the total response time for CATCS is: $\tau_f = \tau_{mhd} + \tau_{cls}$ = *1.88 s*. With this remarkable response time, the CATCS attitude control architecture can be envisaged.

CATCS PERFORMANCE

Before embarking on the performance evaluation, the CATCS attitude control architecture has to be implemented first. The attitude control design in Figure 5 is radically similar for CATCS.

Only the dynamics of this actuator need to be established, see Figure 8.

From Figure 8, the displacement *d,* induced magnetic flux density *B* and resulting torque T_f are the physical constants describing the drivers. Their dependencies are given by the linear motor constant k_L, induced flux density constant k_B, and resulting torque constant k_T, respectively. The system gains are: K_C = *1/n*, and the drivers' constants are held as below for an ideal system

$$\begin{aligned}k_{L1} &= k_{L2} = k_{L3} = k_{L4} = k_L,\\k_{B1} &= k_{B2} = k_{B3} = k_{B4} = k_B,\\\text{and}\quad k_{T1} &= k_{T2} = k_{T3} = k_{T4} = k_T.\end{aligned}$$

The product of these constants is defined as: $k_L \times k_B \times k_T = k_G$. And, the ε in Figure 8 represents the system torque accuracy: ε = *1 $\pm$ ε_T*, where ε_T is the internal torque gain errors. For an ideal system, ε_T would be equal to zero so that ε = *1*. The attitude controller selected is a Proportional-Integral (PI) type, which fulfils the stability aspects as well. Thus, the transfer function for the satellite's dynamics is

$$\frac{\theta_{sat}}{\theta_{ref}} = \frac{1}{\left(1 + \frac{K_P}{K_i}s + \frac{I_{sat}}{K_i k_G \tau_f}s^2 + \frac{I_{sat}}{K_i k_G}s^3\right)}, \quad (13)$$

where

$$F(s) = \frac{1}{1 + (K_P/K_i)s}.$$

With these equations, the control architecture is amenable for the numerical treatment using Matlab™. The reference mission
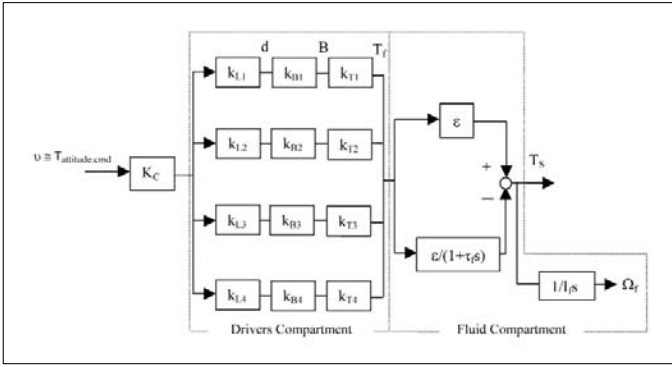
Figure 8: CATCS Actuator Compartment

defined in section 4 is retained for the CATCS performance analysis. The chosen attitude control gains are $K_P = 0.8$ *Nm/rad*, $K_i = 0.011$ *Nm/s*, and k_G is regarded as unity so that the desired and exerted torque commands are directly proportional. The system's response time τ_f was set to *2 s*. The linear motors' delays (e.g. *50 ms*) were also considered in the simulation. The ideal CATCS simulation results are depicted in Figures 9 (a) and (b). The satellite's attitude is within the pointing budget ($\theta_{sat} < 0.2°$), see Figure 9 (a). In Figure 9 (b), the fluid velocity attains the maximum velocity after about 5 operational orbit periods. To reset this velocity, the available standard desaturating methods can be engaged [12].

The second test case is for a non-ideal CATCS. Three torque gain errors are identified for this analysis, e.g. from the linear motors, permanent magnets, and the temperature instability in the MHD compartments. For the motors, about *4%* are assumed for the torque constants' differences. On the other hand, the temperature surrounding the magnets influences their magnetic flux densities *B* acting on the MHD compartments. For the $Nd_2Fe_{14}B$ magnets, this temperature dependency is about *0.15% / °C* [10]. Additionally, the vacuum environment is assumed to have a maximum gradient/margin of *10°C* [13]. Therefore, this would induce *1.5%* difference in the resulting control torque. Finally, the temperature variation in the MHD compartments is held about ± *2 K* with respect to the system's temperature gradient of *50 K* [14]. This
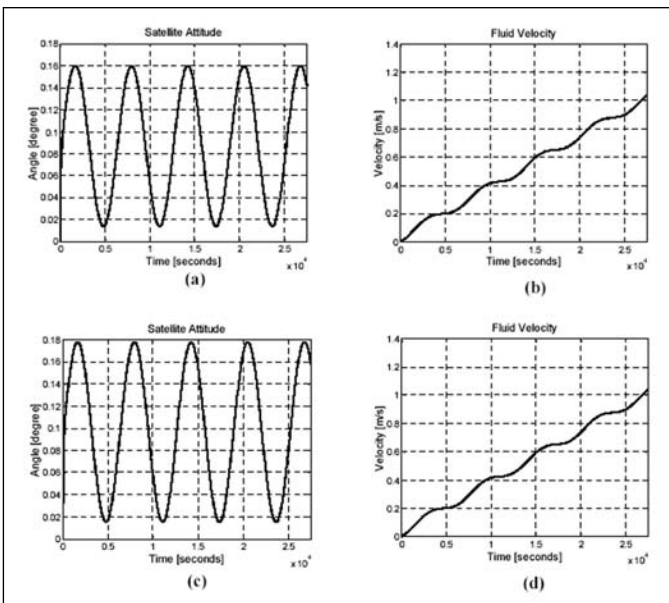
would account for about *4%* of difference in the generated thermoelectricity, and is proportional to the system's torque gain error. So, macroscopically, the total system torque gain errors ε_T would account for about *9%*. For this non-ideal test case, all the system gains were retained as in the ideal simulation. Despite the gain errors, the results pertaining to the non-ideal analysis show that the attitude accuracy and the fluid velocity are still within their nominal limits, see Figures 9 (c) and (d), respectively. Nevertheless, if desired, the attitude accuracy can be increased by tightening the stiffness of the attitude control loop.

So far only the attitude control performance for CATCS is discussed. It is also necessary to view its heat transport aspects. For example, having a temperature gradient of *5 K* (hot and cold satellite walls) together with the estimated mass flow (e.g. *0.3 kg/s*), the system can transport about *560 W* of heat from an exposed area of *0.01 m²*. Thus, the CATCS has a reasonable heat transport capability. On the other hand, the conventional heat pipes have good heat transport capabilities as well. However, in some cases their mass could reach up to *1 kg* or more depending on the types [15, 16]. As a result, the total mass budget for the conventional heat pipes and a reaction wheel (e.g. *0.4 Nms*) could reach up to *2.7 kg* [15, 16, 17]. This indeed has a significant impact on the overall spacecraft mass budget. Instead, the entire CATCS mass budget would account for about *2.5 kg*. Moreover, through the effects of synergism, additional mass savings could be obtained. For example, the CATCS requires only small amount of electrical power for the motors (e.g. *6.4 W* for 4 units) so that the performance of the solar panels and batteries could be reduced in terms of their masses.

It is evident that the CATCS is susceptible to the temperature variations, especially in the MHD compartments. To alleviate this problem and to arrest such situations, the use of electrical heaters (e.g. thermofoils) becomes desirable. These heaters are extremely lightweight, and consume about *1 W* corresponding to the temperature per-heated mass, e.g. *15°C/kg* can be achieved in half an hour for cobalt [18]. Moreover, these thermofoils could be used to partially dump the excess solar power during the begin-of-life (BOL), which could eventually increase the system's thermoelectric generation capability. This coupling can be classified as an additional advantage of the CATCS. Further, to achieve even higher thermoelectricity, the use of better thermoelectric generators (e.g. bismuth) instead of cobalt can be envisaged. In fact, this could be also an approach for the satellites with lower on-board temperature gradients to employ the CATCS. In this investigation, it has to be noted that the magnetic flux densities used are only half of the theoretical value for the reference configuration. Hence, with only two $Nd_2Fe_{14}B$ magnets (e.g. *1 T*), the similar performance presented in this article can be achieved. As a result, the power and mass budgets for CATCS can be reduced accordingly.

CONCLUSION AND OUTLOOKS

The CEACS attitude and power management for a small satellite has been demonstrated in this article. The ideal and non-ideal CEACS performances coincide with the reference mission requirements. The CEACS is a promising alternative compared to the separate conventional attitude and power systems, especially for increasing the life of the LEO satellites. The second system,

Figure 9: CATCS Performance

CATCS, has also its own potentials. This system is suitable for the satellites that require an active thermal control to handle the excess on-board heat. The performances shown by the ideal and non-ideal CATCS also comply with the mission requirements. Moreover, the usage of the unwanted on-board heat for its operation brings the additional benefits for the satellites. Both systems, CEACS and CATCS, demand a stringent design procurement. However, with the current available technologies such systems are judiciously feasible. In order to achieve their formal operational statuses, further research will be concentrated on designing the prototypes. This would also allow the systems' gains or parameters to be characterised profoundly. Finally, this investigation demonstrates the potential synergisms for the attitude control system, and offers a novel approach for designing the future spacecraft.

ACKNOWLEDGEMENT

REFERENCES

[1] W. Robinson, et al., "Spacecraft Energy Storage System," *11th AIAA/USU Conference on Small Satellites*, Logan, Utah, 1997.

[2] P. Guyot, H. Barde, and G. Griseri, "Flywheel Power and Attitude Control System (FPACS)," *4th ESA Conference on Spacecraft Guidance, Navigation and Control System*, ESA-ESTEC, Noordwijk, 1999.

[3] C. M. Roithmayr, International Space Station Attitude Control and Energy Storage Experiment: Effects of Flywheel Torque, *NASA Technical Memorandum 209100*, 1999.

[4] H. Barde, "Energy Storage Wheel Feasibility Study," *4th Tribology Forum and Advances in Space Mechanisms*, ESA-ESTEC, Noordwijk, 2001.

[5] J. A. Kirk, J. R. Schmidt, G. E. Sullivan, and L. P. Hromada, "An Open Core Rotator Design Methodology Rotor," *Aerospace and Electronics Conference*, IEEE-NAECON, Dayton, 1997.

[6] K. H. Sung, K. Dong-Jin, and S. Tae-Hyun, "Optimum Design of Multi-ring Composite Flywheel Rotor Using a Modified Generalized Plane Strain Assumption," *Int. J. Mech. Sci.*, Vol. 43, pp. 993-1007, 2001.

[7] V. Renuganth and S. Fasoulas, The Combined Energy and Attitude Control System for Small Satellites – Earth Observation Missions, *Digest of 4th IAA Symposium on Small Satellites for Earth Observation*, ISBN 3896855697, Berlin, Germany, 2003.

[8] Linear Motor Data Sheet, Haydon, Waterbury, USA, 2002.

[9] S. Lee, "Liquid Metal Wetting of Metal Surfaces Using a DC Glow Discharge," *J. Korean Physical Society*, Vol. 29, pp. 257-260, 1996.

[10] Rare-Earth Permanent Magnets Data Sheet, Vacuumschmelze, Falkensee, Germany, 2001.

[11] R. Moreau, *Magnetohydrodynamics*, Kluwer Academic Publishers: Dordrecht, 1990, pp. 124 –126.

[12] J. R. Wertz, *Spacecraft Attitude Determination and Control*, Kluwer Academic Publishers: Dordrecht, 1994, pp. 202 and 648.

[13] J. W. Larson and J. R. Wertz, *Space Mission Analysis And Design*, Kluwer Academic Publishers: Dordrecht, 1997, pp. 416.

[14] Space Engineering - Mechanical – Part 1: Thermal Control, ECSS-E-30 Part 1A, ESA-ESTEC, 2000.

[15] Heat Pipes Data Sheet, Alcatel, Toulouse, France, 2000.

[16] Thermal Products and Solution Data Sheet, Dynatherm Corporation, California, USA, 1998.

[17] Momentum and Reaction Wheels Data Sheet, Teldix, Heidelberg, Germany, 2000/2001.

[18] Thermofoils Heaters and Controller Data Sheet, Minco Products, Minneapolis, USA, 2002.

NOMENCLATURE

A	cross section
b	width
B	magnetic flux density
D	hydraulic diameter
ϕ	friction coefficient = $0.32\, Re^{-0.25}$
F_L	Lorentz force
h	height
Ha	Hartmann number = $\sqrt{\dfrac{\sigma_{ec}}{\rho \nu}}\, B\, h$
i_{bus}, i_{solar}, i_{local}	currents
I_w, I_f, I_{sat}	inertias
k_m	motor torque constant
K_i	attitude integral constant
K_d	attitude derivative constant
K_p	attitude proportional constant
K_w	flywheel proportional constant
l_θ, l_f	longitudinal length
ν	number of pumps
P	power
Re	Reynolds number = $\dfrac{VD}{\nu}$
t	time
T	torque command
T_D	external disturbance torques
T_S	torque exerted on the satellite body
U	voltage
V	velocity
Δp_{loss}	friction pressure = $f\,\dfrac{2\pi R}{D}\,\dfrac{\rho}{2}\,V^2$
ΔS	thermoelectric power
ΔT	temperature gradient
θ_{ref}, θ_{sat}	reference and true satellite attitudes
$\upsilon = T_{attitude.cmd}$	proportional torque command
ν	kinematic viscosity ($\nu = 3.49 \times 10^{-7}\ m^2\,s^{-1}$)
ρ	density ($\rho = 5907\ kgm^{-3}$)
σ_{ec}	electrical conductivity ($\sigma_{ec} = 3.7 \times 10^6\ Ohm^{-1}m^{-1}$)
Ω	flywheel speed

Simulation of the Distributed Rainfall-Runoff Process

Huang Yuk Feng and Lee Teang Shui

Department of Biological and Agricultural Engineering Faculty of Engineering, Universiti Putra Malaysia,
43400 UPM Serdang, Selangor

ABSTRACT

A deterministic model to simulate rainfall runoff from pervious and impervious surfaces is presented. The surface runoff model is based on an established one-dimensional, variable width, kinematics wave approximation to the Saint Venant equations and Manning equation, to mathematically route overland and channel flow, using the finite element method. The Galerkin's residual finite element formulation utilizing linear and quadratic one-dimensional Lagrangian elements is presented for the spatial delimitation of the nonlinear kinematics runoff equations. The system of nonlinear equations was solved using successive substitutions employing Thomas algorithm and Gaussian elimination. The whole formulation was set up using the MapBasic and MapInfo Geographical Information System. A laboratory rainfall runoff physical model was set up to test the numerical model. Parameters considered include, surface roughness, plane slope, constant or changing rainfall intensities. Linear element simulation was found to give results as accurate as the quadratic element simulation. Increasing the number of elements to simulate runoff from a homogenous surface did not give any added advantage. Whilst the Courant Criterion gives maximum time step increment for computation, it is however recommended that as small a time increment be used to eliminate any oscillatory instability. Time increment for channel flow routing was found to be always smaller when compared to lateral overland flow. Thus, the chosen time step increment for channel flow routing must be a common factor of that of lateral overland flow in order to satisfy the linear interpolation of overland outflow hydrograph as input into the channel. For laboratory scale catchments, smaller upstream plane and larger downstream plane roughness, 0.033 for bare soil surface upstream and 0.300 for grass surface downstream, respectively, can result in small oscillatory disturbances at the rising limb. Such discrepancy does not occur when upstream roughness is larger then downstream roughness. Differences in elemental interface slope can be catered for rather well in the model. A hypothetical watershed and imaginary tropical rainstorm was also studied to verify the stability of the model in larger runoff catchments. Channels, which are initially dry or with existing flows can be simulated incorporating additional rainfall. Large catchments with large physical elemental roughness and slope differences can be well simulated, without oscillations that are evident in laboratory scale tests.

Keywords : Rainfall runoff, finite element, kinematics-wave modeling, overland flow, geographical information system

INTRODUCTION

A hydrologic system model is an approximation of the actual system, in which its inputs and outputs are measurable hydrologic variables and are linked by a set of equations. The flow of water through the soil plane and stream channels of a watershed, however, is a distributed process, since the flow rate, velocity, and depths usually show temporal and spatial variation throughout the watershed. Therefore, by using a distributed hydraulic model, flow rates can be computed as a function of space and time. Most of the hydraulic models require a large number of input data and might produce a large set of output data. A complex, large-area, multi-basin drainage study requires significant effort in terms of data organization, development of models, and presentation of results. To overcome these problems and difficulties, a GIS system can be used to organize, store, and display spatial (maps) and non-spatial (characteristic) data for the study.

In the actual flow process, the velocity of flow in a river varies along the river, across it and differs from the water surface to the riverbed. However, the first two spatial variations can be ignored. The flow process is assumed varying in only one space dimension that is along the flow channel or in the direction of flow. The Saint Venant partial differential equations for continuity and momentum respectively, are the governing equations for one-dimensional, unsteady flow in an open channel. Based on these equations, the simplest distributed or hydraulic routing model is the kinematics wave model, which assumes that the friction and gravity forces balance each other, and the flow condition is steady and water surface profiles are uniform. Direct numerical methods for solving partial differential equations can either follow the finite difference approach, or the finite element method.

Judah used the Galerkin's residual method in the formulation of a flood routing model and obtained satisfactory results [10]. The Galerkin's residual method of the finite element method was also used by Al-Mashidani and Taylor [1] solve the non-dimensional form of the shallow water equations for surface runoff. Cooley and Moin [3] also applied Galerkin's residual method to a finite element solution of open channel flow and obtained good results. Taylor et al. developed a numerical finite element for the analysis of watershed direct runoff problem [12]. White had demonstrated the application of the FEM in watershed analysis [14]. Jayawardena and White presented an analytical basis for the formulation of a distributed catchments model within the flexible framework of the finite element method (FEM) [9]. In this model, the solutions in the space and time domain, is carried out by using the finite element and the finite-

difference method, respectively. A finite element storm hydrograph model (FESHM) has been developed as a distributed parameter model to simulate flow on ungauged watersheds [11].

Blandford and Meadows presented a Galerkin finite element formulation, utilizing linear, quadratic, and cubic one-dimensional Lagrangian elements, for the spatial delimitation of the nonlinear kinematics runoff equations [2]. A method to estimate a suitable computation time-step size based on the Courant condition is also presented. However, using a time increment approximately equal to the presented Courant time increment may not produce accurate results with both explicit and implicit schemes. Viessman et al. stated that for the explicit time integration scheme, the best results are obtained with a time increment of 20% off of that defined by the Courant condition [13]. Giammarco et al. (1995) developed a conservative finite elements approach to overland flow, known as the control volume finite element (CVFE) method [5]. This CVFE method is said to be extremely useful and flexible not only for overland flow studies but also for flood plain modeling.

The objective of this study is to develop a deterministic GIS based finite element model to simulate the rainfall runoff process. A laboratory scale model with various surface conditions and uniform rainfall simulation will be used to verify the model's computation stability, accuracy and differences between the linear and quadratic element based models used. The model is then to be checked for its stability when applied to fictitious real world catchments, albeit only in its computation stability, so that it can be used later for real life simulations.

METHODOLOGY

Several assumptions were made:

(i) evaporation and evapotranspiration are assumed to be zero for the purpose of this study in order to reduce the complexity of the model. This is an event driven model and this assumption can be valid for the duration of rainfall runoff process;

(ii) excess rainfall is the only inflow onto the overland;

(iii) the net inflow into the channel is contributed from the direct rainfall onto the channel as well as from lateral overland flow; and

(iv) assuming that the kinematics overland and channel flows have only a forward characteristic with no backwater effects. The Saint-Venant (1871) equations of continuity and momentum form the basis for the solution. The kinematics wave based model neglects the local accelerations, convective acceleration, and pressure terms in the momentum equation, and thus assumes that the friction and gravity forces balance each other, that is, $S_o = S_f$. and is approximated using the Manning equation.

FINITE ELEMENT FORMULATION

The finite element method is especially adaptable to the problem of evaluating the impact of land-use changes on flood flows since a watershed and channel can be divided into a finite number of sub-areas or elements. The hydrologic properties of one or all of the elements can then be altered to simulate the

effect upon the hydrologic response of the entire watershed system. The results from the overland flow are considered as input for the subsequent channel flow computation, ignoring direct rainfall into the channel. The same finite element formulation can be applied for the both stages.

The derivation of the finite element equation involves the development of algebraic equations from a governing set of differential equations. Galerkin's residual method was used to derive the individual element equations because it has been demonstrated to be a good formulation procedure for surface flow problems. For the finite element grid consisting of more than one element, it must be arranged in a form, which embodies the total number of elements. The direct stiffness method is used to obtain the assembled matrices. The algebraic equations must be solved as a set of simultaneous equations to obtain the primary unknowns, area of flow A, at the nodes. Here, the Thomas algorithm and the Gaussian elimination are used to obtain the solution. The solutions of the system equations are next used to calculate the secondary unknowns, discharge Q, at the nodes.

DETERMINING STEP TIME INCREMENT

Selection of a proper time increment to be used for flow routing process in the model is essential for an efficient and accurate solution. A large value of time increment may produce an inaccurate result or an instability problem. On the other hand, a time increment that is too small requires larger number of computations. In the finite element model, a time step is chosen to satisfy the Courant condition. Courant condition time increment is the time taken by the kinematics wave to travel from node to node (element length). The equation to estimate the maximum Courant condition time increment (Blandford and Meadows, 1990), applicable in the model is given by:

$$\Delta t_c = \frac{\Delta x}{\left(m.\alpha^{\frac{1}{m}}\right)} \left(L.i_{max}\right)^{\frac{1}{m}-1} \tag{1}$$

In cases where more than one value of n and S is applied, the smallest n and biggest S should be selected. The calculated time increment approximates the maximum time increment that should be used in the model. In the case of channel flows, using this calculated time increment for flow routing, produced inaccurate results. Here, the value of maximum rainfall intensity should be replaced by the maximum lateral inflow value from the lateral strip of the channel. This is because, the lateral inflow into the channel is very high compared to the direct rainfall falling on to the channel. Thus, depending on the rainfall duration, a suitable value of the time increment, which must be at least equal to or less than the Courant condition time increment, should be chosen for both the overland and channel flows routing.

TEMPORAL EXCESS RAINFALL DELIMITATION

Typically, excess rainfall event data are reported and displayed at regular time interval, say, every 1 min, 5 min, or at breakpoint intervals. Such a discontinuous loading function would cause convergence problems. To eliminate the abrupt discontinuities in the excess rainfall, a

linear transition over two time steps is used. The transition scheme adopted here is such that it conserves the excess rainfall volume. This transition strategy will result in less oscillatory results in runoff simulation.

MODEL

A model based upon the mathematical equations delineated was programmed using the MapBasic Language and run concurrently with the desktop MapInfo Geographical Information System. The simple rectangular laboratory set up is used as an example to illustrate some of the geographical information system functions in running the model and are as shown in Figures 1 - 5.
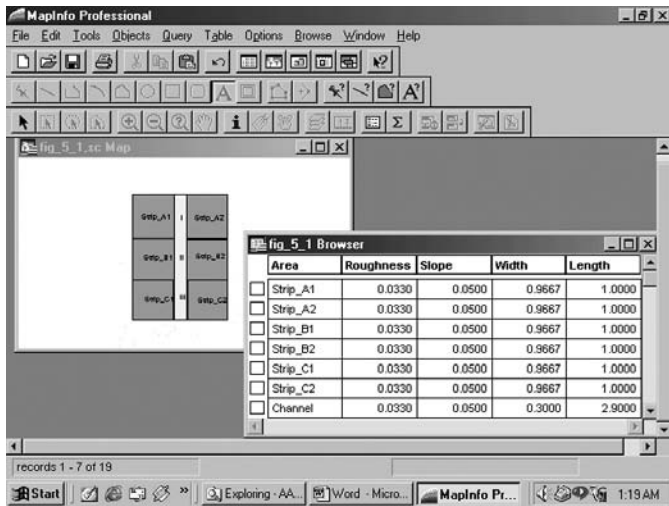

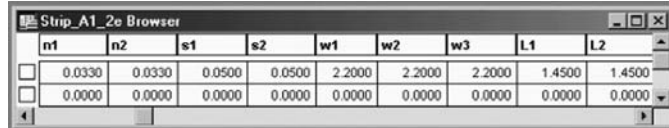**Figure 1: Example of the digitized map of the Laboratory Setting with corresponding MapInfo data table**

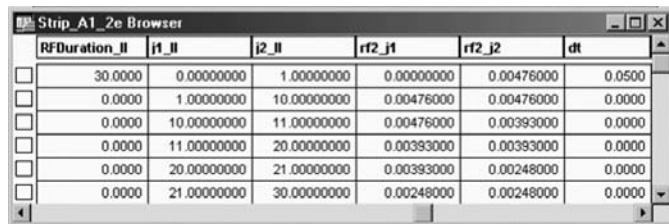**Figure 2: MapInfo Data Input Table for a 2-element overland flow strip**

Figure 3: Excess rainfall data and time increment MapInfo Input Table

LABORATORY TESTS

The laboratory apparatus consist of a rainfall simulator, runoff basin, runoff collection drain (discharge measurement), and infiltration-percolation collecting tray. The rainfall simulator was made such that the raindrops are formed by a large number of sprinklers spaced at 30 cm apart, and inserted into seven equal lengths of 32 mm diameter PVC pipes. The pipes were placed parallel to each other at a spacing of 30 cm. The sprinklers were set in a 30 cm × 30 cm (one-square-foot) rectangular grid with one sprinkler at each corner. The simulator was suspended at 45 cm above the runoff basin. Water is supplied through a gate valve controlled water pump, which pumped water uniformly and
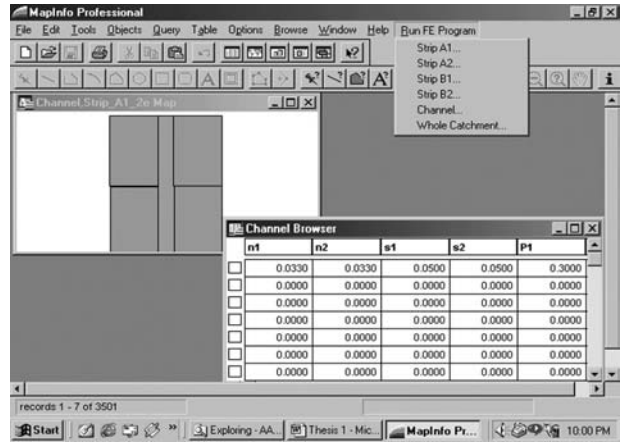

Figure 4: MapInfo Menu for MaBasic program execution for a 2-element channel
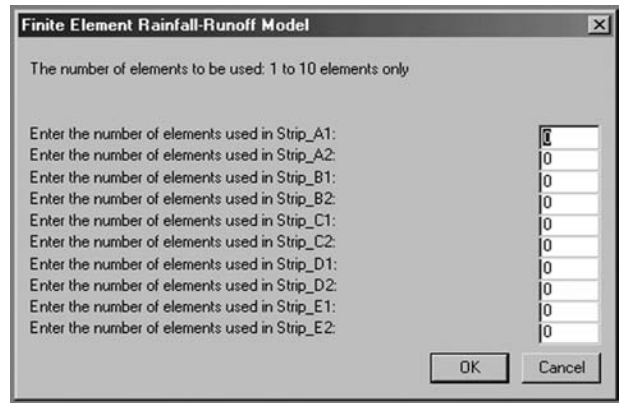
Figure 5: MapInfo Dialog Query Box for number of elements to be used

continuously from a constant-head tank. According to Yoon et al. and Hall et al. [16; 7], droplet size and droplet velocity were reported to have a negligible effect to the flow mechanics of the plane compared to the rainfall intensity.

The dimensions of the basin are 2.9 meters in length and 2.2 meters in width. The soil used consisted of mining sand and clayey loam soil, each of equal volume, with the clayey loam soil on top. The total thickness of the plane was 30 cm and the surface was lightly compacted. The runoff surface plane of the basin when required was formed by changing to the appropriate type of materials; namely, bare clayey loam soil, Taiwanese Grass, a combination of bare clayey loam soil surface and grassed surface, and plywood. In addition, different values of plane slope were also set in the runoff basin for the overland flow and overland with channel flow cases. For overland with channel flow, the runoff basin was divided symmetrically into two equivalent sections along the longitudinal axis of basin, with the channel placed right in the middle of the basin, as shown in Plate 1.

RANGE OF EXPERIMENTAL CONDITIONS

In runoff hydrograph measurements for overland flow planes, two different slopes, 5% or/and 10%, were set for each of the surface condition. The surface conditions are bare clayey loam soil (Plate 2), Taiwanese grass (Plate 3), bare clayey loam soil and Taiwanese grass interface (Plate 4), and plywood (dimension: 1.125m × 2.400m). In addition, a clayey loam soil overland flow

Plate 1: Runoff basin for overland with channel flow simulation

Plate 2: Runoff basin with bare clayey loam soil surface

Plate 3: Runoff basin with Taiwanese grass surface

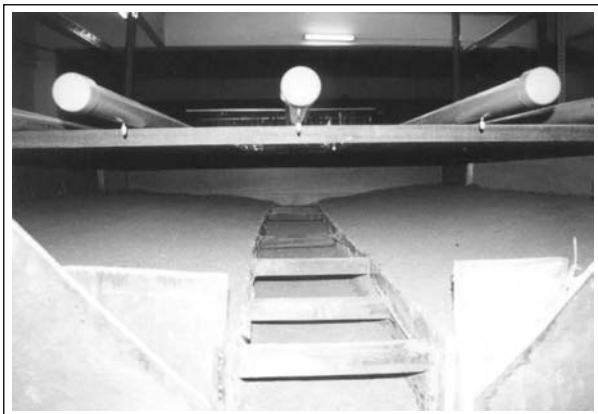**Plate 4: Runoff basin with bare clayey loam soil (upstream) and Taiwanese grass (downstream).**

plane with a combination of two different slopes (5% and 10%) was used. For the overland with channel flow experiments, the only surface condition used was clay soil, and the side slopes were set to either 5% or 10% slope. The longitudinal flow channel of the plane was also built up using clay soil and fixed at 5% slope for all experiments (Plate 1).

The duration of all constant rainfall events was 20 minutes, except for the plywood surface, which was set to 5 minutes. The duration for all the experiments with increasing or decreasing rainfall intensity was set at 10 minutes per rainfall intensity, making a total of 30 minutes for an experiment run over three different intensity. Similarly, 5 minutes duration (a total of 15 minutes for the experiment) were set for the experiments on plywood surface.

RESULTS AND DISCUSSIONS EFFECTIVE RAINFALL

In the laboratory set up, the only infiltration rate that can be determined is the maximum infiltration rate, which occurred when the measured infiltration rate become constant. This is the time after which all the soil in the model is well wetted and absorbs no more water. The excess rainfall that is calculated during this period can be considered as the maximum excess rainfall for that rainfall event. Since the laboratory model is very small, it can be assumed that the excess rainfall rate will be constant when the measured runoff-discharge volume first becomes constant, as long as the rainfall intensity is constant. Figure 6 shows the discharge hydrograph of the laboratory test which was set at 5% bare soil slope for overland flow with 4.76×10^{-3} m^2/min excess rainfall, 2.2m width, 2 equal 1.45m length elements; using linear element.

An excess rainfall hyetograph and discharge hydrograph for a changing rainfall intensity event is illustrated in Figure 7 (Laboratory Test: 5% bare soil slope for overland flow with $4.76 \times$
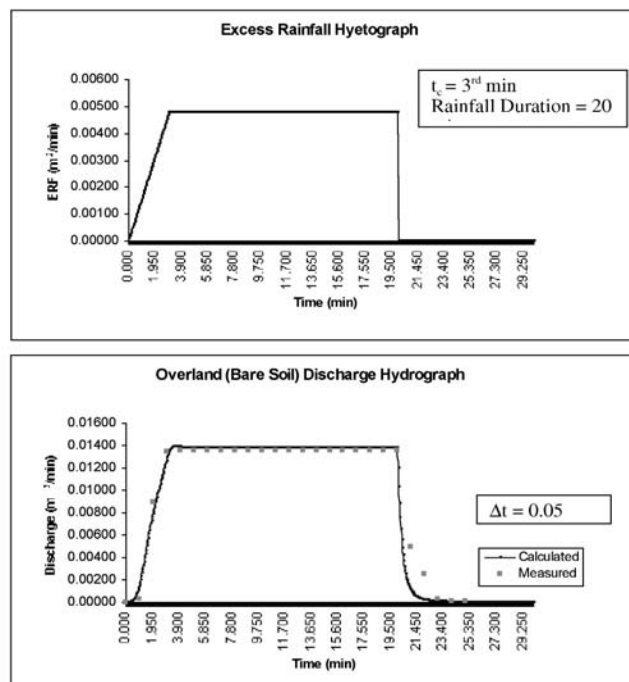

Figure 6 : Excess Rainfall Hyetograph and corresponding Discharge Hydrograph for 5% slope bare soil (n = 0.033) overland flow. Rainfall intensity 2.67 x 10^{-3} m/min
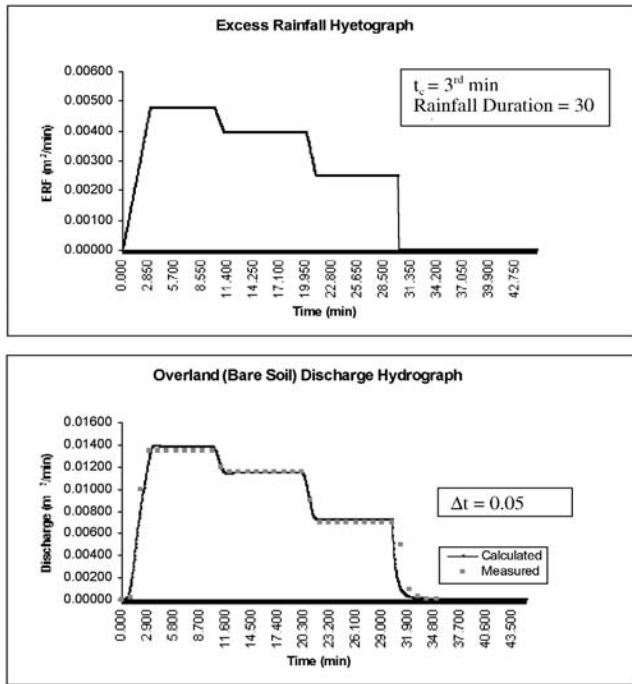
Figure 7: Excess Rainfall Hyetograph and corresponding Discharge Hydrograph for 5% slope bare soil (n = 0.033) overland flow. Consecutive rainfall intensities 2.67 x 10-3, 2.25 x 10-3, 1.44 x 10-3 m/min

Figure 8: Discharge Hydrograph for 10% slope grass (n = 0.300) overland flow. Rainfall intensity 2.25×10^{-3} m/min, $\Delta t > \Delta t_c$

Figure 9: Discharge Hydrograph for 10% slope grass (n = 0.300) overland flow. Rainfall intensity 2.25×10^{-3} m/min, $\Delta t > \Delta t_c$

Figure 10: Discharge Hydrograph for 10% slope grass (n = 0.300) overland flow. Rainfall intensity 2.25 x 10-3 m/min, $\Delta t > \Delta t_c$

10^{-3}, 3.93×10^{-3}, and 2.48×10^{-3} m^2/min excess rainfall, 2.2m width, 2 equal 1.45m length elements; using linear element simulation model

TIME INCREMENT SELECTION

It was observed that the value of time increment depends on the length of element used, the surface roughness, slope, maximum rainfall intensity, and the length of the whole system. Hence, time increment must be chosen so that the Courant condition for that particular case is always satisfied to avoid kinematics shocks that produce instability. In addition, the selected time increment must be a common factor of the rainfall duration also (required for the purpose of interpolation in excess rainfall between two adjacent time period). If a smaller time increment were to be used, it will give a more stable and accurate result.

Figures 8, 9 and 10 show the results of using different time increment values for a laboratory test (2 elements, linear element simulation), where $\Delta t > \Delta t_c$, $\Delta t = \Delta t_c$, and $\Delta t < \Delta t_c$ respectively.

In this case, the time increment that should be used according to Courant condition is about 0.54 minute. However, this value is not a common factor of the rainfall duration (20 minutes). The biggest common factor that is less than 0.54 is 0.50, which is about 7.4% off the Courant condition time increment. Thus, the recommended values of time increment that can be used in simulation include 0.50, 0.40, 0.20, 0.10, 0.05, or other values, as long as it is a common factor of the rainfall duration and less than 0.54.

However, in channel flows routing process, the time increment is calculated according to the peak overland flow runoff discharge volume into the channel from lateral strips. It is recommended that the time increment used in channel flow routing be as small as possible. This is because the maximum rainfall intensity in the equation to determine time increment is now replaced by the maximum lateral inflow from the overland strips from both sides. A large volume of lateral inflow will result in a very small Courant condition time increment value.
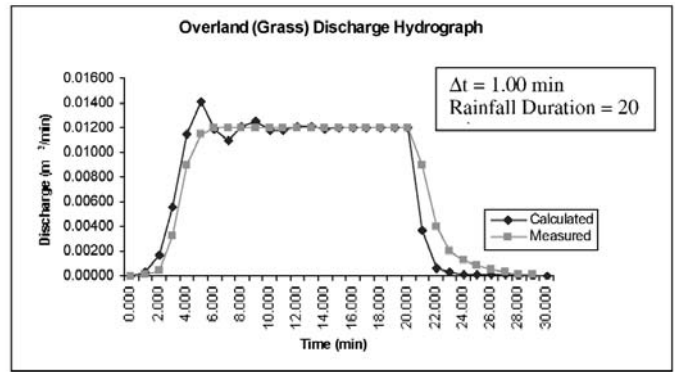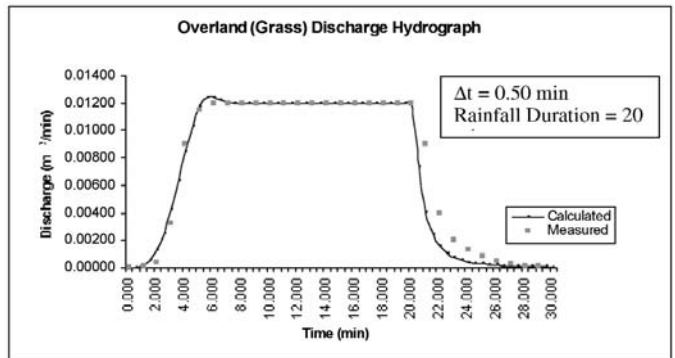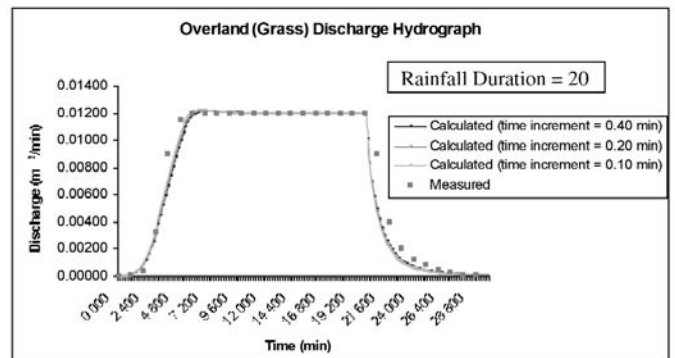
The dissipative mechanism can be quickly dampened by the judicious choice of the time increment. Although it is said that the maximum time of computational time increment is the Courant Criterion, it can be concluded that the time increment selected should be as small as possible. It is not true that satisfying the Courant criterion will result in solutions that are inherently stable. With increased iterations, flow behavior is more precisely simulated than that of using a single time leap for the wave to travel to the element node. This linear time discrete is thus an important consideration in the solution of the algorithm.

SELECTION OF SURFACE ROUGHNESS

The Manning roughness coefficients for the bare soil and

grass were selected using values recommended by Engman [4] for overland flow. The recommended values for bare clay-loam (eroded) ranges from 0.012 – 0.033, and 0.170 – 0.300 for dense grass. In all the laboratory tests, the value of roughness coefficient chosen for bare soil is 0.033, and 0.300 for dense grass (Taiwanese grass). The Manning roughness coefficient for the plywood surface is estimated as 0.015 using the value recommended by Schwab al. [15], which ranges from 0.010 to 0.015 for planed wood. The highest value of roughness coefficient from the ranges is always selected for all cases. This is because the laboratory model is very small relatively, and will need a very small time increment value to produce results without undue divergence, especially when the rainfall intensity used is high, or the number of element used is large.

NUMBER OF ELEMENTS AND ELEMENT LENGTH

According to the Courant condition time increment equation, the time increment value used in a system mainly depends on the element length of the system. The shorter the element length, the smaller is the time increment needed for the model simulation. The criteria of element length selection and the number of element used in a system mainly depend on the topography condition of the simulation area, such as surface roughness and slope. Areas with the same roughness coefficient and slope should be selected as an element, instead of dividing it into two or more elements. Two simulations had been carried out to prove that the number of elements used to assess a homogenous surface did not affect the simulated results: (1) using different number of elements for a homogeneous overland flow routing system; (2) using different number of elements for a homogeneous overland flow with channel flow routing system. In both cases, the results were not significantly different in terms of absolute values. On the other hand, in situations where the use of shorter element length and bigger number of element cannot be avoided, for example, in a natural catchments due to the various types of surface physical properties, selection of a smaller time increment value is still needed and cannot be avoided.

LINEAR VERSUS QUADRATIC INTERPOLATION FUNCTION MODELS

From simulations performed it was found that simulated results obtained through using either the linear or quadratic function models were similar. However, it is noted that quadratic element simulation model need a smaller time increment value than that predicted by the Courant condition time increment because it has a bigger matrix iteration for the same number of element compared to the linear element simulation model.

ACCURACY, STABILITY, AND CONVERGENCE

Various sets of test (not shown here) with different physical and rainfall conditions have been carried out for this purpose. From all the plots, it can be concluded that almost all the simulated result matched quite closely with the measured results. However, some of the peak discharge and the volume of runoff for
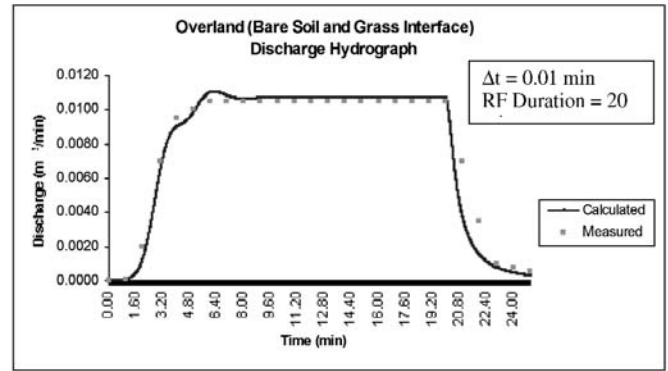
Figure 11: Discharge Hydrograph for 5% slope bare soil (upstream, n = 0.033) and grass (downstream, n = 0.300) interface overland flow. Rainfall intensity 2.25 x 10^{-3} m/min
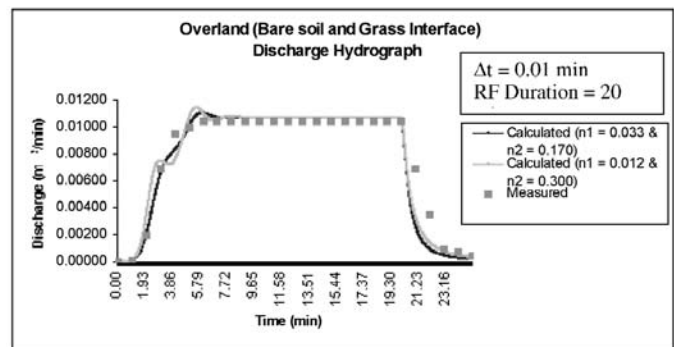
Figure 12: Discharge Hydrograph for 5% slope bare soil (upstream, n = 0.033) and grass (downstream, n = 0.300) interface overland flow. Rainfall intensity 2.25 x 10^{-3} m/min, two sets of different roughness

certain events have been either over-predicted or under-predicted although the deviations are not large. The inconsistency can be due to the assumption of overall homogeneity of infiltration, roughness, rainfall intensity, slope, and uniform pumping pressure in all the laboratory experiments. But in reality, this is virtually impossible to achieve all at once for each individual experiment.

Almost in all the events, the rising curves have been underestimated by model. This discrepancy may be caused by the assumption of linear transition of the simulation of the excess rainfall, from zero to the maximum constant rate. In the recession curve of all the hydrographs, the simulated results always show faster recession and underestimation due the residual effect of remaining water in the pipes as explained earlier.

A laboratory test using bare soil surface with two different slopes, 5% (upstream side) and 10% (downstream side), divided into two equal length elements, was also set to check the ability of finite element method in simulating runoff discharge for an area with different slopes. Generally, the results simulated by the model for both constant rainfall intensity, and changing rainfall intensity events are close to the measured results. Further evaluation included a laboratory test using a bare soil (upstream) and grass (downstream) interface as runoff surface, divided equally into two elements (each with 1.45m of length), to check the ability of finite element in simulating runoff discharge from an area with different roughness coefficients. The simulated discharge hydrograph compared to the measured discharge hydrograph is shown in Figure 11. The rising curve in the simulated hydrograph has shown

small oscillations. The roughness coefficient values used in the model is 0.033 for bare soil surface, and 0.300 for grass surface, a factor of 10 difference. This may be the main factor that affects the rising curve simulated by the model. This is where the kinematics-wave theory may fail due to dam effect at the interface.

When two closest values of roughness coefficient for bare soil and grass are used, 0.033 for bare soil and 0.170 for grass, and compared to the case where two as-far-apart-as-possible roughness coefficient values for these two surfaces is used, 0.012 and 0.300 for bare soil and grass surfaces respectively, the simulated rising curves have shown that the former case would produced less oscillatory result, as shown in Figure 12. Thus, when the two values of roughness coefficient used in simulation differs by a large margin, there will be more instability. The spurious oscillatory behavior can be suppressed when the difference between adjacent values of roughness (and perhaps slope) is made very much smaller. On the contrary, if the upstream elemental roughness has a bigger value compared to the downstream end, the resulting simulated hydrograph would be normal. However, this is only a conclusion made from the laboratory condition, where the catchments model is very small. If the same situation is applied in bigger catchments, this oscillatory may not occur. The scale factor of the physical model may be contributory impedance in model simulation.
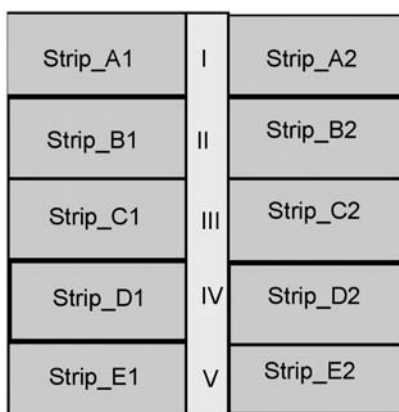

Figure 13: Schematics of a fictitious large natural catchments with 5 strips each side of overland flow and 5 element for channel flow

NATURAL CATCHMENTS

The parameters of a hypothetical larger natural catchments and imaginary rainstorms, was used to verify the stability of the model in simulation in large real catchments. A catchments area about 25km^2 (5 × 5 km) is considered for this purpose. The catchments is a square area with a channel flows in the middle of the catchments, as shown in Figure 13.

The overland components in the both sides of the channel are divided into five equal strips, each with 1 km width and 2.5 km long. The surface of the overland area (strips) has a 10% slope, and covered by a material with a coefficient of roughness, 0.20. Similarly, the channel has a 2% slope with 0.02 of roughness coefficient. Each strip is delimitated into five equal length elements (0.5 km each). Similarly, the channel is also delimitated into five equal 1 km length elements with 30 m width. A constant excess rainfall intensity, i = 50 mm/hr (8.333 × 10^{-4} m/min) with 1-hour rainfall duration is applied to the model. The result simulated from the catchments is shown in Figure 16.

The peak flow runoff discharge volume of 6,500.0 m^3/min (or, 108.33 m^3/sec) of the catchments simulated by the model is reasonable when compared to a catchments used as an example in DID [6], with the approximate size of area and rainfall intensity. Similarly, a constant rainfall intensity, i = 100mm/hr (1.667 × 10^{-3} m/min) is also applied in the model with the same catchments to check the stability of the model in simulating with different rainfall intensities (Figure 14).

In addition, an overland component (strip) in the catchments was tested with different rainfall durations of these rainfall intensities values and, was found that the model work as well. Also, with this overland component, different rainfall intensities amongst the elements in the system was applied to test the stability of the model in simulating a condition where the catchments system has different rainfall intensities, or some parts totally without rainfall.
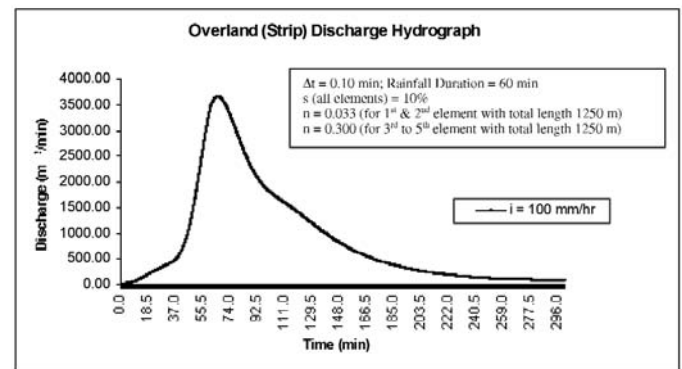
Figure 14: Comparison of fictitious large natural catchments runoff hydrographs for two rainfall intensities
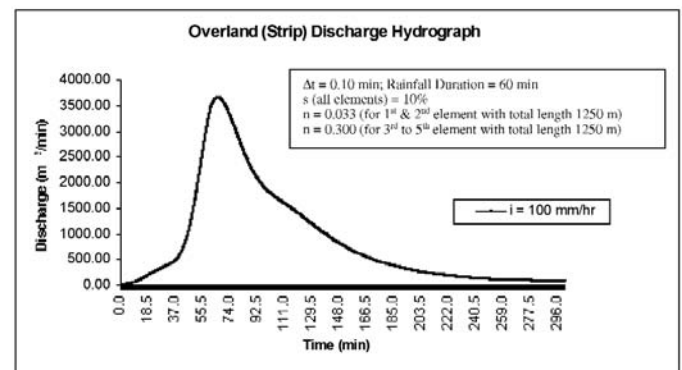
Figure 15: Oscillatory effects not evident in fictitious large natural overland component with different roughness coefficient values amongst the elements in the overland system

VARYING CATCHMENTS TOPOGRAPHY

In order to verify the capability of model to simulate rainfall-runoff events for different types of topography condition, the overland component from the catchments was also tested with different sets of physical conditions. As mentioned previously, when different values of roughness coefficient are used in the small-scale physical model for overland flow simulation, the results were oscillatory. However, when the same conditions were applied to this big overland component (divided into two equal 1,250 m
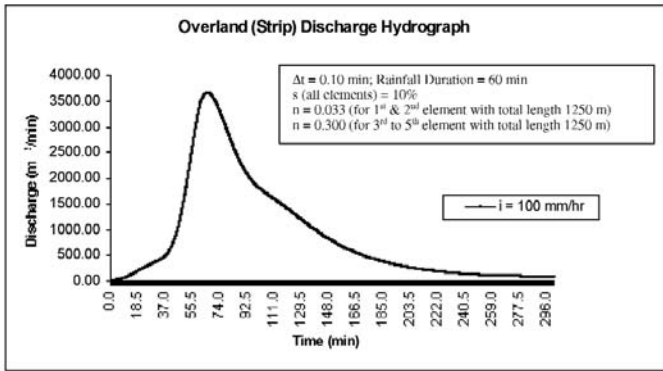
Figure 16: Oscillatory effects not evident in fictitious large natural overland component with different roughness coefficient values and slopes amongst the elements in the overland system
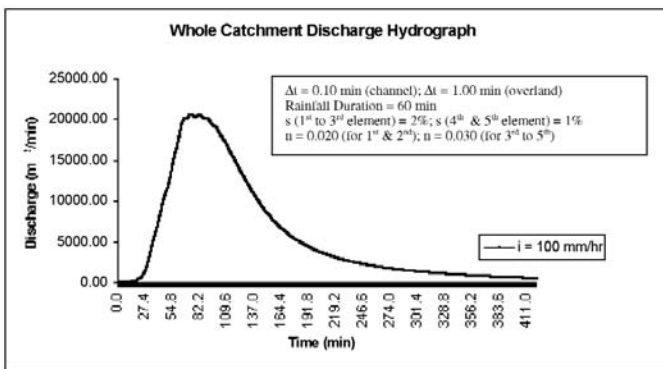
Figure 17: Oscillatory effects not evident in fictitious large natural catchments with different roughness coefficient values and slopes amongst the elements in the channel system

length with upstream roughness 0.033 and downstream roughness 0.300), the results are as illustrated in the following Figure 15.

The finite element method can work well in large-scale catchments, with different roughness coefficient values amongst the elements in the system. In addition, the same condition as used in the previous case, but with different values of plane slopes, was also simulated, and the results shown were reasonable, as in Figure 16.

It was also applied to the same whole catchments system (with channel) used previously, where the roughness coefficients and slopes used in the channel system are set with different values. The results shown in Figure 17 indicated that the model could be used to simulate a channel flow routing system with different physical conditions accurately.

CHANNELS WITH EXISTING FLOWS

All the theoretical cases discussed before were without existing flows in the channel. The model was also tested with the consideration of an existing flow in the channel. For this purpose, a volume of discharge, $Q = 989$ m^3/min (or, 16.48 m^3/sec), is assumed to exist uniformly in the channel. The hydrograph produced by the model for this is shown in Figure 18. This plot indicated that the existing flow would continue to discharge in combination with rainfall and lateral flows input into the channel. A similar condition was also applied to the system where a larger volume of existing flow is assumed, and where $Q = 5,742$ m^3/min (or, 95.70 m3/sec). The hydrograph is illustrated in Figure 19.

It can be noted that the sum total runoff discharge volume below the hydrograph (without existing flow) and the hydrograph (with existing flow only), is always equal to the runoff discharge volume of the catchments hydrograph (with existing flow, $Q = 5,742$ m^3/min). The outflow discharge hydrograph for the combination of existing flow with rainfall and lateral flows input, initially is contributed mainly by the existing flow in the channel. The rainfall and lateral inflows into the channel initially did not show any obvious contributions. It is illustrated that, after about twenty-one minutes, the rainfall and lateral inflows started to contribute to the channel runoff discharge. This situation would be continued until about the forty-ninth minute, whereby thereafter, the channel runoff discharge is almost only contributed by the rainfall and lateral inflows (assuming the whole volume of existing flow has been routed out). Thus the model could be used to simulate runoff discharge of a catchments system with an existing flow in the channel. For the case of a perpetual uniform existing flow, then the superimposition principle holds.
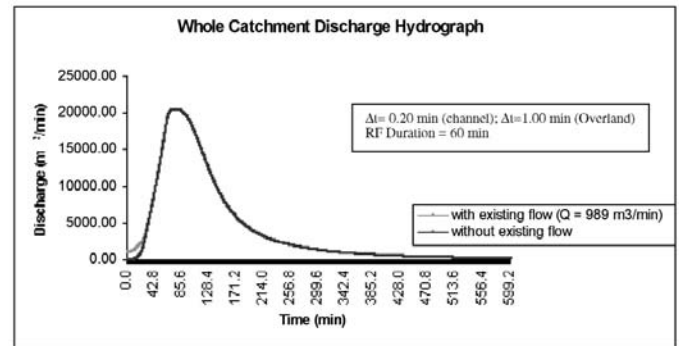
Figure 18: Simulation of fictitious large natural catchments discharge for channel without/with existing flows (lower volume)
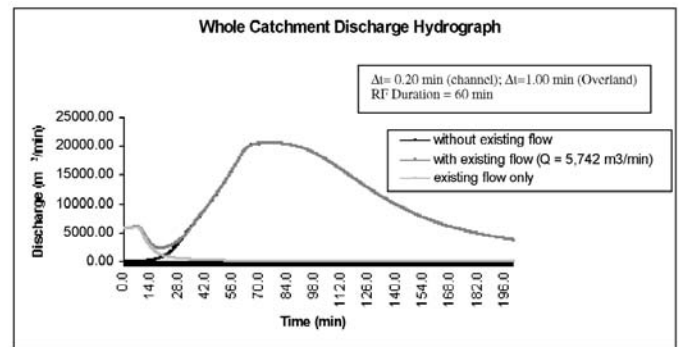
Figure 19: Simulation of fictitious large natural catchments discharge for channel without/with existing flows (higher volume)

CONCLUSIONS

The following conclusions were drawn from this study: (i) it is confirmed that the kinematics wave equation solved by the finite element standard Galerkin's residual method is able to simulate the runoff for overland plane and channel accurately; (ii) the spurious oscillatory behavior for the overland flow and channel flow can be suppressed by using a smaller time increment value (the smaller the better), governed by the Courant criterion; (iii) the temporal excess rainfall discrete scheme adopted has shown good results with less oscillatory disturbance at the point where discontinuous excess rainfall data are prescribed; (iv) spatial variations in geometry, hydrologic properties, and precipitation can be easily incorporated using geographical information

systems; (v) number of elements used in runoff simulation did not significantly affect the simulated results. The consideration of number of element to be used in the model mainly depends on the topography, and/or climatic properties of the catchments. The linear and quadratic element simulation methods gave similar predictions of peak runoff volume, and the rising and receding curves pattern; (vi) simulation with differential elemental roughness whereby the upstream roughness is smaller than downstream roughness, have indicated inconsistent result in the upper end of the rising limb. However, when upstream roughness is larger than the downstream roughness, this discrepancy did not appear. Scale effects and/or storage detention at the interface by the rougher surface downstream, seems to be the reason for this phenomenon. However, all this does not appear in larger catchments and; (vii) in the recession curve of all the hydrographs, the simulated results always show faster recession and underestimation. This is due to the problem in the laboratory setting in that water through the spray nozzles could be not stopped instantaneously, upon closure of the control valve. The residual water in the pipes would contribute quite a big volume of water onto the small-scale lab runoff basin. This being in contrast to the mathematical model that assumes instantaneous cutoff.

REFERENCES

[1] Al-Mashidani, G., and C., Taylor, 1974. Finite Element solutions of the shallow water equations-surface runoff. In: J.T. Oden, O.C. Zienkiewicz, R.H. Callagher and C. Taylor (Editors), Finite element methods in flow problems. University of Alabama Press, Huntsville, Ala., pp.385-398.

[2] Blandford, G.E., and M.E., Meadows, 1990. Finite Element Simulation of Nonlinear kinematics surface runoff. Journal of Hydrology, 119:335-356.

[3] Cooley, R.L., and S.A., Moin, 1976. Finite element solution of Saint Venant equations. Journal of Hydraulic Division., ASCE, 102 (HY 6):759-775.

[4] Engman, E.T. 1986. Roughness Coefficients for Routing Surface Runoff, Journal Irrigation Drain. Engrg. ASCE, Vol.112 (1).

[5] Giammarco, P.D., E.Todini, P. Lamberti, 1995. A conservative finite elements approach to overland flow: the control volume finite element formulation. Journal of Hydrology, 175(1996), 267-291.

[6] DID, 1997. Hydrological Procedure No. 5, Rational Method of Flood Estimation for Rural Catchments in peninsular Malaysia. Revised and Updated in 1989. Drainage and Irrigation Department, Ministry of Agriculture, Malaysia.

[7] Hall, M. J., Johnston, P. M., and Wheater, H. S., 1989, Evaluation of Overland Flow Models Using Laboratory Catchments Data, 1. An Apparatus for Laboratory Catchments Studies, Journal of Hydrological Science, Vol. 3(3), 1989.

[8] Jayawardena, A.W. and J.K., White, 1977. A Finite Element Distributed Catchments Model I: Analytical Basis. Journal of Hydrology, 34 (1977) 269-286.

[9] Jayawardena, A.W. and J.K., White, 1979. A Finite Element Distributed Catchments Model II: Application to real catchments. Journal of Hydrology, 42 (1979) 231-249.

[10] Judah, O.M., 1973. Simulation of runoff hydrographs from natural watersheds by finite element method. Ph.D. Thesis, Virginia Polytechnic Institute and State University, Blacksburg, Va.

[11] Ross, B. B. et al. 1982. Model for simulating runoff and erosion in ungauged watershed. Bulletin 130, Virginia water resource center, Virginia Polytechnic Institute and State University Blacksburg, Virginia.

[12] Taylor, C., Al-Mashidani, G., and Davis, J.M., 1974 A Finite Element Approach to Watershed Runoff. Journal of Hydrology, 21 (1974) 231-246.

[13] Viessman, W. Jr., and G. L., Lewis, 1996. Introduction to Hydrology. Harper Collins College Publishers, USA, 1996.

[14] White, J.K., 1973 A finite element deterministic catchments model. In C.A. Brebbia and J.J. Connor (Editors), Numerical Methods in Fluid Dynamics, Pentech Press, London, pp. 533-543.

[15] Schwab, G.O., Fangmeier, D.D., and Elliot, W.J. 1992. Soil and Water Conservation Engineering, John Wiley & Sons. Inc. Fourth Edition, 1993.

[16] Yoon, Y. N., and Wenzel, H. G., 1971, Mechanics of Sheet Flow Under Simulated Rainfall Journal of the Hydraulics Division, ASCE, Vol. 97, No. HY9, Proc. Paper 8373, Sept 1971, pp. 1367-1386.

ACKNOWLEDGEMENTS

NOTATION

Q	discharge overland or in channel
A	wetted Area, channel flow area
R	hydraulic radius
L	element length
V	flow velocity
q	lateral inflow
n	roughness coefficient
Δx	smallest element length
Δt	time increment
Δt_c	Courant time increment
i_{max}	maximum rainfall intensity
x	horizontal distance
y	depth of water surface
t	flowing time
g	gravity
S_f	friction slope
S	plane slope, bed slope
m	coefficient

Remediation of Heavy Metal Contaminated Soil by Using Chemical Stabilization

Yin Chun Yang, Md Ghazaly Shaaban and Hilmi Mahmud

Department of Civil Engineering, Faculty of Engineering, University of Malaya, 50603 Kuala Lumpur

ABSTRACT

The effectiveness of ordinary portland cement (OPC) in the immobilization of heavy-metal contaminated soil was investigated in this study. Heavy metal contaminated soil was collected from a scrap metal yard within the outskirts of Kuala Lumpur, Malaysia. Metal composition analysis indicated that the predominant heavy metals present in the soil were iron and aluminium with some composition of zinc and lead and little composition of copper and chromium. The contaminated soil was treated with OPC using cement-to-dry soil (C/S_d) ratios of 0.5, 1, 2, 4 and 8. The effectiveness of the treatment was evaluated by performing unconfined compressive strength (UCS) test and crushed block leaching on the treated soil. Crushed block leaching tests were performed in accordance with standard protocols of Method 1311: Toxicity Precipitation Leaching Procedure (TCLP) and Method 1312: Synthetic Precipitation Leaching Procedure (SPLP) of the United States Environmental Protection Agency (USEPA). The treatment results were compared to the solidified waste acceptance criteria which were compiled based on the regulatory waste disposal limit at a disposal site in the United Kingdom (UK) and the maximum concentration of contaminants for toxicity characteristic of solid wastes from USEPA. The UCS values of the solidified samples at 28 days under air drying for C/S_d ratios of 0.5 – 8.0, far exceeded the minimum landfill disposal limit of 0.34 N/mm^2 at a disposal site in the UK. Subsequent to leaching of the treated soils by three different leaching solutions (acetic acid, deionized water and nitric/sulfuric acid), metals in the leachates were either undetectable or appreciably below the proposed leachability limits.

Keywords : Land remediation, chemical stabilization, ordinary portland cement (OPC), heavy metal contaminated soil, unconfined compressive strength (UCS), leachability

INTRODUCTION

Chemical stabilization or chemical immobilization techniques which are more extensively utilized in the treatment of hazardous wastes, are increasingly finding applications in remediation of contaminated soil especially in developed countries such as the United States [1] and European Union [2]. Applications of established technologies for land remediation are scarce and still in its infancy in Malaysia due to the lack of specific contaminated land legislations that obligate land polluters to bear the clean up costs. Consequently, the disinclination of land polluters (mostly small and medium industries) to shell out exorbitant land remediation clean up fees had diluted specific pertinent stakeholders' effort in ensuring that remediation of numerous contaminated land are aptly carried out. Comprehensive researches on chemical stabilization technologies in Malaysia are only limited to treatment of industrial wastes prior to land disposal, most of which are undertaken at local academic institutions. Hence, there is a need to research novel remediation techniques or customize established ones for local applications in Malaysia in order to address the increasing exigency in remediating contaminated land to protect the public health as well as the environment.

Chemical stabilization is generally defined as a chemical alteration technique of reducing the mobility and solubility of contaminants present in waste or soil in order to convert that particular waste or soil into chemically innocuous form which may or may not include production of a monolithic matrix [3]. Chemical stabilization of contaminated soil may produce an end product of high strength which can be reused as construction-base materials. The objectives of this study were to evaluate the effectiveness of OPC treatment for heavy metal-contaminated soil which was subjected to Malaysian weather and establish the most appropriate C/Sd ratio for the treatment based on the treated material's ultimate purpose or destination.

MATERIALS AND METHODS

Site and Soil Sample Description

An operational scrap metal yard located within the outskirts of Kuala Lumpur was selected as the study area (Figure 1). The scrap metal yard has been in operation for more than a decade and manages a variety of scrap metals ranging from construction steel bars to metal components of household appliances. Contaminated soil samples were collected at depths of 20 cm from the surface by using a stainless steel shovel and stored in cylindrical plastic containers. Based on visual inspection, the soil was dark in colour and contained fragmented metal pieces. All labware and sampling apparatus were pre-soaked in 5% nitric acid solution followed by distilled water for a day prior to sampling to remove trace concentrations of metals. Large plant debris and metal pieces were manually discarded from the contaminated soil samples before subjected to screening by using a 2-mm sieve.

Characterization of Contaminated Soil

Physical characteristics that include moisture content, soil particle density (specific gravity), soil pH, loss-on-ignition and particle size distribution were determined by using the *British Standard Methods for Test for Soils for Civil Engineering Purposes* [4]. The soil was acid digested by using *Method 3050B: Acid Digestion of Sediments, Sludges and Soils* [5] prior to chemical

Figure 1: Scrap metal yard

analysis by using the OPTIMA 3000 Perkin-Elmer Inductively Coupled Plasma-Optical Emission Spectrometry (ICP-OES).

Production of Solidified Samples

Type 1 OPC obtained from Associated Pan Malaysian Cement was used throughout the study. The OPC was selected as binder in this study due to its relatively inexpensive cost and easy availability in Malaysia which may prove crucial should the technology be locally commercialized. The technical justification for its selection was due to the fact that composition of OPC was much more consistent, thus eliminating some of the many variables in studying chemical stabilization processes [6]. OPC was added to the contaminated soil at C/S_d ratios of 0.5, 1, 2, 4, and 8. Mixing of these materials was done in a 25-L SPAR type mixer. The sieved contaminated soil and cement were added into the mixer and homogenized for 15 minutes prior to the addition of ASTM Type II deionized water. It was ensured that the addition of water to the cement and soil was adequate to produce a mixture with a flow of 10% by using a K-slump tester specified in the standard test procedure given in ASTM Standard Method C 1362-97 [7]. The mixture was then cast into 50 mm × 50 mm × 50 mm cubic steel molds, 25.4 mm × 25.4 mm × 25.4 mm cubic perspex molds and 0.5-litre high-density polyethylene (HDPE) cylinder in three layers, with each layer compacted by using a vibrating table to yield good packing of the solidified samples. Solidified cubic samples for all the tests were prepared in triplicates. After the initial mixing, one day was allowed for setting before the solidified samples were demolded. A total of 27 days were allowed for air drying of the solidified samples in a cabinet at a controlled condition (temperature = 25 ± 2°C, humidity > 80%).

Unconfined Compressive Strength

The unconfined compressive strength (UCS) test measures the compressive strength of a material without lateral confinement [8]. This test was conducted on the solidified samples to indicate whether the treated material had adequate strength to support any overburden pressure. The 50 mm × 50 mm × 50 mm solidified cubic samples were subjected to the UCS test [9] at 1, 3, 7, 21 and 28 days.

Leaching Tests

Crushed block leaching tests were performed according to the standard US Environmental Protection Agency protocols of Method 1311: Toxicity Precipitation Leaching Procedure (TCLP)

[10] and Method 1312: Synthetic Precipitation Leaching Procedure (SPLP) [11]. The TCLP leaching solution was designed to simulate the worst-case leaching conditions on disintegrated landfill wastes due to prolonged aging effects while SPLP used a leaching solution that simulated acid rain. Although the TCLP test is principally used to determine hazardous characteristics, it is occasionally utilized to determine the impact of a waste on groundwater even when the waste is stored or disposed in non-landfill conditions [12].

For the TCLP test, 50 g of crushed samples (dry-cured for 28 days) which passed through a 9.5 mm sieve were placed in low-density polyethylene (LDPE) containers prior to addition of 1 litre of 0.1 M nitric acid (solution pH = 2.88) to provide a ratio of 20:1 mass ratio of leachant to solidified samples. The containers were then agitated using a rotating extractor at 30 rpm for 18 hours. Leachate pH was measured at the end of the extraction period prior to vacuum filtration (using 0.45-micron membrane filter) since the level and control of pH were extremely crucial factors in evaluating leachability of OPC-stabilized wastes, especially for metals [6]. The filtrate was then acidified with nitric acid to pH<2 and stored under refrigeration (<4°C) prior to heavy metal analysis by using the ICP-OES. The SPLP test was slightly different from the TCLP as it required a leaching solution of diluted nitric/sulphuric acid (solution pH = 4.20) while other features remained the same. All TCLP and SPLP analysis were performed on sample triplicates and average values were used. A third leaching solution, deionized water (pH = 6.80) was used to examine the impact of a non-aggressive solution.

Table 1 : Soil physical characterization

Characteristic	Value
Particle Size	Gravel = 22.68
Distribution (%)	Sand = 72.91
	Silt & Clay = 4.41
Moisture Content (%)	14.48
Soil Particle Density	2.616
Soil pH	7.11
Loss-on-ignition (%)	7.63

RESULTS AND DISCUSSION

Characterization of Contaminated Soil

Results of contaminated soil physical characterization are shown in Table 1. The contaminated soil comprised of 22.68wt % of gravel, 72.91wt % of sand and 4.41wt % of silt and clay prior to sieving. The soil was classified as "gravelly sand" based on the British Soil Classification System [13]. The soil moisture content and particle density were 14.48% and 2.616 respectively while pH of the soil was determined to be slightly alkaline at 7.11. The soil consisted of 7.63% of organic content as determined by the loss-on-ignition (LOI) test [4].

Table 2 shows the result of the heavy metal analysis. High concentration of iron (108,290 mg/kg of soil) in the samples was observed because construction steel bars were the predominant type of scrap metal stored at the site. Zinc, lead and aluminium

were also present in the samples in excess of 1000 mg/kg of soil while copper and chromium were detected at concentrations of less than 1000 mg/kg.

Table 2: Heavy metal concentrations in contaminated soil

Heavy Metal	Concentration (mg/kg)
Fe	108,290
Cr	275
Cd	ND
Zn	2,315
Pb	1,005
Cu	559
Al	5,967

ND denotes "below detection limits"

Solidified Waste Acceptance Criteria

Table 3 lists the solidified waste acceptance criteria which were used to evaluate the effectiveness of the treatment. These criteria were compiled and used for evaluation purposes of the chemical stabilization treatment due to unavailability of soil and groundwater standards as well as solidified waste treatability criteria in Malaysia. The two characteristics selected for assessment of the treated soils were UCS and leachability since the two were the predominant criteria assessed for the effectiveness of solidification/stabilization treatment in the United States [14]. The regulatory UCS and leachability levels were extracted from two sources; regulatory waste disposal limit at a disposal site in the United Kingdom (UK) [15] and the maximum concentration of contaminants for toxicity characteristic of solid wastes from US Environmental Protection Agency [10,11].

Table 3: Solidified waste acceptance criteria

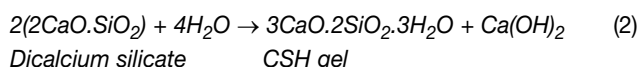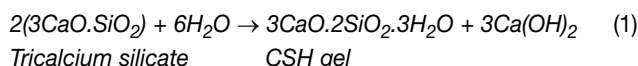| Characteristic	Regulatory (Acceptance) Level	
Compressive strength at day-28 (N/mm^2)	Landfill disposal limit†	:0.34
	Comparative mortar limit†	:20
Leachability (mg/L)	Cadmium*	:1.0
	Chromium*	:5.0
	Lead*	:5.0
	Copper†	:5.0
	Zinc†	:10.0

†Regulatory waste disposal limit at a disposal site in the UK (Sollars & Perry, 1989)
*U S EPA maximum concentration of contaminants for toxicity characteristic (SW-846)

Strength Development of Solidified Samples

Table 4 shows the UCS data of solidified samples throughout 28 days of air drying. Figure 2 shows the UCS development of solidified samples throughout 28 days of air drying while the correlation between UCS, C/S_d and curing age is depicted in Figure 3 as contour and surface profile which was created by utilizing Surfer 7.0. The UCS values of the solidified samples at 28 days of dry curing were in the range of 9.4 – 34.7 N/mm2 for C/S_d ratio of 0.5 – 8.0, which far exceeded the minimum landfill

disposal limit of 0.34 N/mm2 at a disposal site in the UK. It was observed that all solidified samples possessed UCS above 0.34 N/mm2 even at the age of one day. This result indicates that by doubling the C/S_d ratio, the UCS of solidified samples had averagely increased by approximately 6 N/mm2 from the preceding ratio at the age of 28 days. This effect was attributed to the fact that by increasing the C/S_d ratio, the amount of tricalcium silicate and dicalcium silicate (predominant elements in cement) increased in the stabilized soil enabling more production of tobermorite gel or calcium-silicate-hydrate (CSH) [16]. This, in turn, provided more strength to the solidified samples. The reactions of both tricalcium silicate and dicalcium silicate with water to produce CSH are shown in Equations (1) and (2).

$$2(3CaO.SiO_2) + 6H_2O \rightarrow 3CaO.2SiO_2.3H_2O + 3Ca(OH)_2 \quad (1)$$
Tricalcium silicate   *CSH gel*

$$2(2CaO.SiO_2) + 4H_2O \rightarrow 3CaO.2SiO_2.3H_2O + Ca(OH)_2 \quad (2)$$
Dicalcium silicate   *CSH gel*

Overall, higher UCS values were obtained when higher amount of OPC was used for the solidification process. It was observed that the high concentrations of heavy metals as well as organic content in the soil did not have a significant retardation effect on the hydration and initial strength development of the treated material, as indicated by the rapid strength development during the first three days of curing. A minimum C/S_d ratio of 2 was required to achieve the UK's typical UCS mortar limit of 20 N/mm2, in which solidified contaminated soils had tremendous potential in construction material applications such as engineering fills, pavement blocks, bricks etc.

Table 4: UCS of solidified samples throughout 28 days of air drying

C/S_d	Unconfined Compressive Strength (N/mm^2)				
	1 day	3 days	7 days	14 days	28 days
0.5	1.2	5.8	9.4	9.3	9.4
1	6.0	12.6	13.8	16.3	15.4
2	11.8	16.4	19.5	23.7	21.0
4	13.5	25.2	25.9	32.1	29.2
8	19.4	34.0	31.4	32.8	34.7

Crushed Block Leaching

Figure 4 indicates the leachate pH of the three leaching solutions, deionised water, acetic acid and nitric/sulphuric acid subsequent to filtration. Figures 5 and 6 show the metal concentrations of TCLP leachates by using acetic acid and deionized water as leachants at various C/Sd ratios while Figure 7 indicates the metal concentrations of SPLP leachates at various C/Sd ratios. It was determined that the leachate pH of the three leaching solutions subsequent to leaching were essentially alkaline ranging from 12.34 to 12.49 (TCLP-deionised water), 11.41 to 11.94 (TCLP-acetic acid) and 12.37 to 12.53 (SPLP-nitric/sulphuric acid).

The results of TCLP and SPLP tests conducted on the solidified samples indicated that all analyzed metals in the three different leachates were either undetectable or appreciably below the proposed leachability limits as a direct effect of chemical stabilization by OPC. The only evident metal present in the three different leachates were aluminium with concentrations ranging from 1.27 to 0.107 mg/L. The high treatment efficiency may be attributed to the high pH value (>11) of the treated soils as

the precipitation of insoluble metal hydroxide. As a result of the high pH of the treated soils, the metals were retained in the form of insoluble hydroxide within the solidified matrix [1,6]. Equation (3) shows the generic reaction between metal in the contaminated soil with the free hydroxide ion when water is added into the mixture.

$$\text{Metal + free hydroxide ion} \rightarrow \text{Insoluble metal hydroxide} \quad (3)$$
$$\text{(Precipitation)}$$
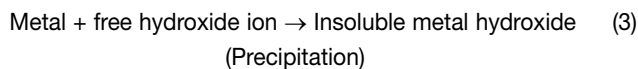
It was observed that there was no substantial effect of type of leaching solution used on the leachability of the metals with the exception that trace concentrations of aluminium were determined in each of the C/S_d ratio of which acetic acid was used as the leaching solution. In addition, it was noticed that
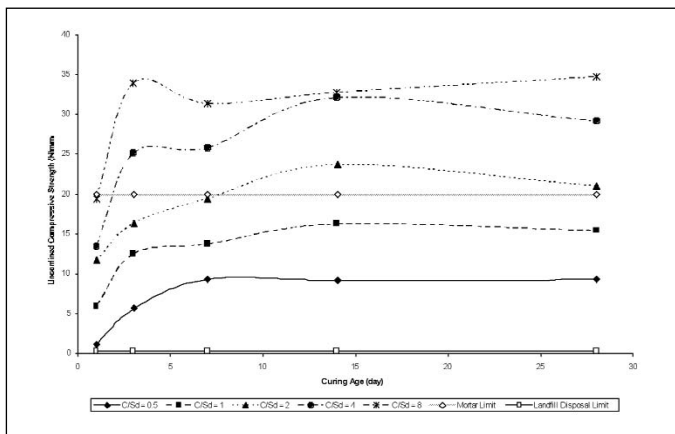
Figure 2: UCS development of solidified samples throughout 28 days
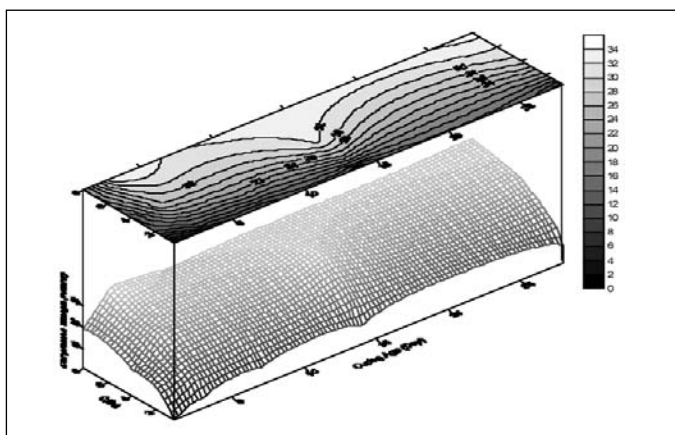
Figure 3: Development of UCS of solidified samples throughout 28 days corresponding to various C/Sd ratios
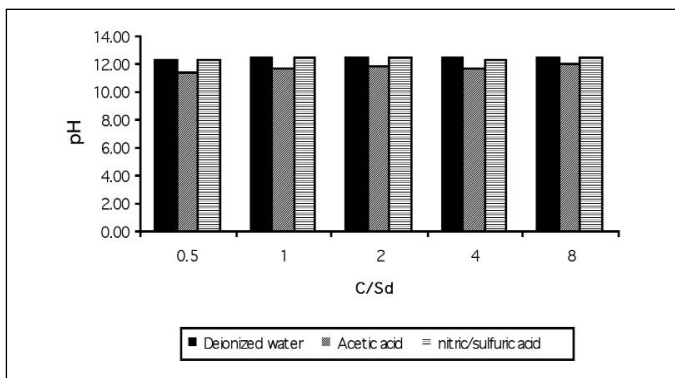
Figure 4: Comparison of leachate pH of the three leaching solutions subsequent to filtration

indicated by the pH of the leachates. It was postulated that the principal mechanism responsible for the effective treatment was hydroxide precipitation. Mass production of hydroxide ion due to hydration of OPC at the initial stage of treatment had facilitated
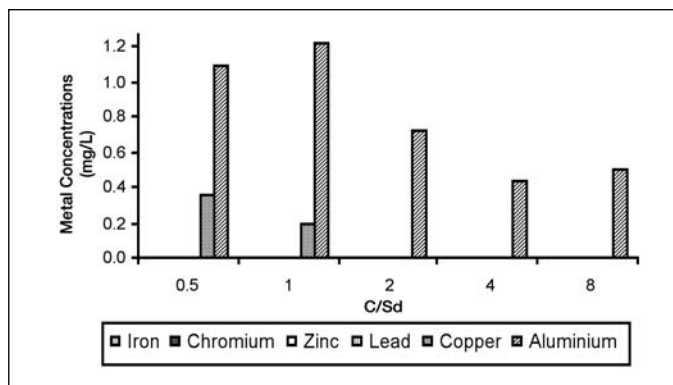
Figure 5: Metal concentrations of TCLP leachate (acetic acid as leaching solution) at various C/S_d ratios
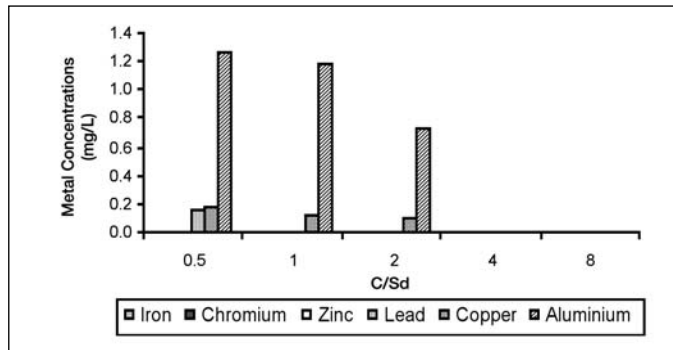
Figure 6: Metal concentrations of leachate (deionized water as leaching solution) at various C/S_d ratios
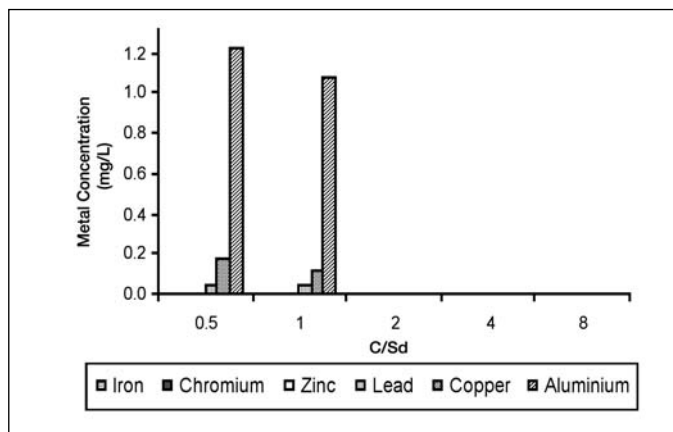
Figure 7: Metal concentrations of SPLP leachate (nitric/sulfuric acid as leaching solution) at various C/S_d ratios

increases in the C/S_d ratios were accompanied by meagre reduction of detectable metal concentrations except for the case of the deionized water and the nitric/sulfuric acid leaching solutions where no metals were detected at C/S_d ratios of 4 and 8. The results indicated that increasing the C/S_d ratios reduced the leachability of metals from the solidified samples.

Ultimate Purpose or Destination of Treated Contaminated Soils

Analysis of UCS development as well as leachability of solidified samples in this study indicated that the amount of OPC used to treat contaminated soils should be dictated by the ultimate purpose or destination of the treated soils; landfill disposal or construction material applications. If landfill is the ultimate destination of the OPC-treated soils, then treatment should be carried out by using the lowest C/S_d ratio of 0.5 in order to minimize treatment costs by which the treated product would adequately comply with the proposed UCS and leachability criteria. Alternatively, if the treated products are to be used as engineering fills or construction materials, then it is recommended that the treatment be carried out using the C/S_d ratio of 2 in order to comply with the comparative mortar limit of 20 N/mm^2.

CONCLUSIONS

Chemical stabilization is an effective land remediation method for heavy metal contaminated soils based on the compliance of the UCS and leachability of the treated material with the compiled solidified waste acceptance criteria. The strength development and heavy metal leaching from OPC treated contaminated soil had been evaluated and the following conclusions can be drawn:

(1) Increasing the C/Sd ratio increased the strength of treated soils.

(2) All solidified samples exhibited UCS above the minimum requirement for landfill disposal limit of 0.34 N/mm^2 even at the age of one day. A minimum C/S_d ratio of 2 is required to achieve the minimum UCS mortar limit of 20 N/mm^2 subsequent to 28 days of air drying.

(3) Leachability tests conducted on the solidified samples indicated that all analyzed metals in the leachates as a result of leaching by using three solutions (deionized water, acetic acid and sulphuric/nitric acid) were either undetectable or appreciably below the proposed leachability limits.

(4) There was no substantial effect of type of leaching solution used on the leachability of the metals.

(5) The amount of OPC used to treat contaminated soils should be dictated by the ultimate purpose or destination of the treated soils:
- landfill disposal (C/S_d ratio of 0.5)
- construction material applications (C/S_d = 2).

ACKNOWLEDGEMENT

REFERENCES

[1] M.D. LaGrega, P.L. Buckingham and J.C. Evans, *Hazardous Waste Management*, Second Edition, New York, McGraw-Hill, 2001, pp. 677 – 740.

[2] U. Ferber and D. Grimski, "Brownfields and Redevelopment of Urban Areas", A Report from the Contaminated Land Rehabilitation Network for Environmental Technologies, 2002.

[3] C.Y. Yin, M.G. Shaaban and H.B. Mahmud, "Strength Development of Cement-stabilized Heavy Metal Contaminated Soil", Proceedings of the LUCED-I&UA International Conference on Environmental Management and Technology. 4-6 August 2003, Putrajaya, Malaysia, pp. 226 – 229.

[4] British Standards Institution, BS 1377: 1990, "British Standard Methods of Test for Soils for Civil Engineering Purposes", London.

[5] United States Environmental Protection Agency, SW-846, Method 3050B, "Acid Digestion of Sediments, Sludges and Soils", 1996.

[6] J.R. Conner, *Chemical Fixation and Solidification of Hazardous Wastes*, New York, Van Nostrand Reinhold, 1990.

[7] American Society of Testing and Materials, "Annual Book of ASTM Standards, Section Four: Construction", Volume 04.01, 2000, C 1362-97.

[8] United States Environmental Protection Agency, "Technical Resource Document: Solidification/stabilization and its Application to Waste Materials", EPA/530/R-93/012, 1993.

[9] British Standards Institution, BS 1881: Part 116: 1983, "Method for Determination of Compressive Strength of Concrete Cubes".

[10] United States Environmental Protection Agency, SW-846, Method 1311, "Toxicity Characteristic Leaching Procedure", 1992

[11] United States Environmental Protection Agency, SW-846, Method 1312, "Synthetic Precipitation Leaching Procedure", 1994.

[12] T.G. Townsend, "Leaching Characteristics of Asphalt Road Waste", Technical Report, Florida Center for Solid and Hazardous Waste Management, pp 22, 1998.

[13] British Standards Institution, BS 5930: 1981, "Code of Practice for Site Investigations".

[14] United States Environmental Protection Agency, "Solidification/stabilization Use at Superfund Sites", EPA-542-R-00-010, 2000, pp. 7.

[15] C.J. Sollars and R. Perry, "Cement-based Stabilization of Wastes: Practical and Theoretical Considerations" *Journal of the Institution of Water and Environmental Management*, 3, pp. 125 – 132, 1989.

[16] A. M. Neville, *Properties of Concrete*, Fourth Edition, London, Addison Wesley Longman Limited, 1996.

Numerical Simulation of Dust Cake Build-up and Detachment on Rigid Ceramic Filters for High Temperature Gas Cleaning

[1]T.G. Chuah, [2]J.P.K.Seville

[1]Department of Chemical and Environmental Engineering, Faculty of Engineering, Universiti Putra Malaysia,
43400 UPM Serdang, Selangor.
[2]Department of Chemical Formulation Engineering, School of Engineering, University of Birmingham, Edgbaston,
B15 2TT Birmingham, United Kingdom.

ABSTRACT

Rigid ceramic filters have proved themselves as highly efficient gas filtration devices. However, the filter cleaning mechanisms by which deposited cake is removed from the filter surface are still not fully understood. A mathematical model that is capable of simulating the time-dependent build-up of dust filter cakes, on the surface of filter, including the calculation of the corresponding pressure drop and the thickness of filter cake which formed during the filtration is proposed. The model also simulates the regeneration of the filter medium and predicts the residual pressure drop after regeneration. This paper focuses on the first basic mechanism of regeneration, the forming and the detachment of the dust filter cake. This enables the simulation of several cycles of filtration and regeneration to investigate the long-term-behaviour of a dust filter.

Keywords : *Rigid ceramic filters, dust cakes, filtration cycles, residual pressure drop, incompressibility*

INTRODUCTION

Periodically regenerable cake-forming filters are used to separate particles from gases with high dust concentrations, whereby the separation arises as the dust-gas mixture passes through the filter medium and the particles are retained. During the build-up of the filter cake the pressure drop over the filter increases, making a regeneration of the filter medium indispensable. The regeneration is performed at a defined maximum pressure drop across the filter and after regeneration the next filtration-cycle starts and a new dust filter cake is built-up on the cleaned filter medium.

The residual pressure drop is a measure of the dust remaining in the depth of the filter medium. Unfortunately, it quite often happens that the residual pressure drop does not reach a constant value after several filtration cycles, but increases steadily due to the fact that not all the filter cake is removed by cleaning. This so-called `patchy cleaning' [1, 2] affects both the residual pressure drop and the rate of pressure increase in the following filtration cycle that may lead to a breakdown of a stable operation.

The objective of this paper is to develop a mathematical model that is capable of simulating the long term build-up of dust filter cakes, on the surface of filter, including the calculation of the corresponding pressure drop along the axis of the filter during filtration. The model should also simulate of the regeneration of the filter medium and predict the residual pressure drop after regeneration. As a first step the authors concentrated on the first basic mechanism of regeneration, the forming of the dust filter cake. This enables the simulation of several cycles of filtration and regeneration to investigate the long-term-behaviour of a dust filter.

The model should also clarify the mechanism which causes the steady increase of the residual pressure drop of a dust filter over time. It was found in some previous studies that the long-term-behaviour of the residual pressure drop depended on the compressibility of the dust cake on the filter medium. Therefore, the adhesion force and the effective distance of separation between the particles were also studied.

SIMULATION OF DUST CAKE BUILD-UP ON THE FILTER MEDIUM

This section describes a physical model for cake and pressure build-up on candle filters. The model was aimed at investigating filtration operation and reverse pulse cleaning of the filter. It is useful to calculate the filter cake thickness and pressure drop along the filter candle. Figure 1 shows the schematic diagram of filter cake build-up on the filter surface.
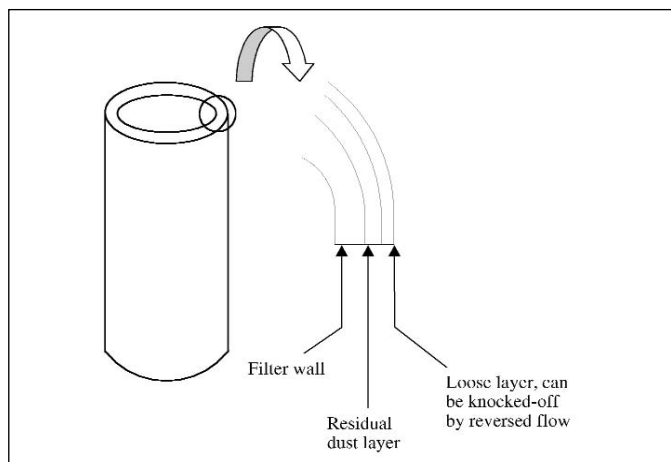

Figure 1: Schematic diagram of filter cake build-up on the filter surface

Assumptions

The model used here has to omit several factors that may affect the filtration operation and is considerably "idealised". However, this model is targeted to describe the most important physics of filtration before its secondary effects are taken into consideration.

The model derivation makes the following assumptions:

i)   All particles entering the filter housing are deposited on the surface of the filter.

ii) The filter cake and the filter medium obey Darcy's law.

iii) The gas is incompressible.

iv) To simplify the model, the small area at the bottom of the filter (closed end, about 1% of the total filter surface), for which the gas flow rate differs significantly from the rest of the filter, is ignored in the subsequent analysis.

Filter 'conditioning' or 'blinding', the penetration of fine particles into the filter pores may sometimes occur and increase the pressure drop across the filter. The effect of penetration of finer particles deeper into the filter cake has recently been modelled [3]. However, it is not considered in this analysis.

Flow Through Thick Filter

[4] suggested a numerical expression to define the pressure drop through a thick-walled rigid filter. Consider a flow at face velocity, U_o, through a thick-walled cylindrical filter of outside diameter, D_o and internal diameter, D_i. The volumetric gas inflow per unit length of the filter candle is $\pi D_o U_o$. Neglecting any changes in gas density as it passes through the porous medium, the superficial velocity at any intermediate radius r is

$$U = U_o D_o / 2r \qquad (1)$$

Assuming the radial flow is a viscous flow (i.e. Re is small), then Darcy's law can be applied here:

$$\frac{dP}{dr} = -k_1 \mu U = -\frac{k_1 \mu U_o D_o}{2r} \qquad (2)$$

Therefore, the total pressure drop across the filter candle wall is given by:

$$\Delta P_f = \int_{\frac{D_i}{2}}^{\frac{D_o}{2}} \frac{k_1 \mu U_1 D_o}{2r} \, dr \qquad (3a)$$

$$= \frac{k_1 \mu U_0 D_0}{2} \int_{\frac{D_i}{2}}^{\frac{D_o}{2}} \frac{dr}{r}$$

$$= \frac{k_1 \mu U_0 D_0}{2} \ln\left[\frac{D_o}{D_i}\right] \qquad (3b)$$

Figure 2 shows a schematic diagram of flow through a thick filter candle wall. The calculation will be extended into the filter cake build-up model and will be discussed in next section.

Because of the cylindrical geometry of the filter and filter cakes, Darcy's law needs to be solved in polar coordinates. Neglecting any changes in gas density as it passes through the porous dust medium, the superficial velocity at any intermediate radius r_c as before is given by;

$$U_c = U_o \frac{D_o}{2r_c} = U_o \frac{D_o}{D_c} \qquad (4)$$
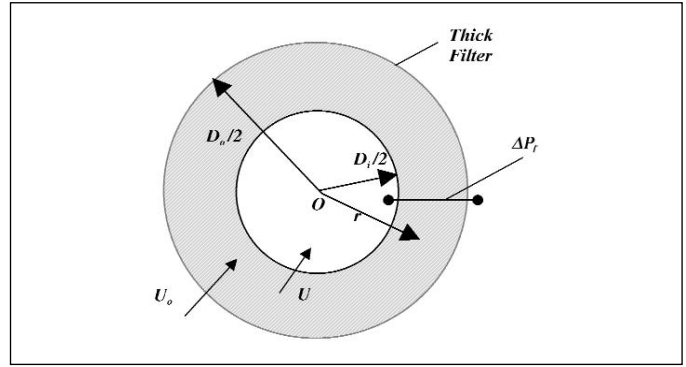
Figure 2: Schematic diagram of flow through thick filter candle.

Hence, the pressure drop across the filter cake between the filter medium and dust cake is:

$$\Delta P_c = \frac{k_2 U_c D_c}{2} \ln\left[\frac{D_c}{D_o}\right] \qquad (5)$$

where, k_2 is the cake resistance, D_c is the outer diameter of filter cake and U_c is the superficial velocity through the outer radius of cake (Figure 3).

The constant gas flow rate into the filter vessel, Q (volumetric flow rate per unit length), can be written as:

$$Q = \pi D_c U_c = \pi D_o U_o = \pi D_i U_i \qquad (6)$$

Then, U_c can be rewritten as:

$$U_c = \left(\frac{D_o}{D_c}\right) U_o \qquad (7)$$

The thickening rate of the cake formed on the surface of the filter can be determined by a dust volume balance:

$$\frac{dx}{dt} = \frac{w U_c}{\rho_c} \qquad (8)$$

$$\Delta x = \int \frac{w U_c(t)}{\rho_c} \, dt \qquad (9)$$

where w is the dust concentration (kg/m³) in the gas flow, which has been taken to be constant, ρ_c is the cake density and Δt is the time interval from $t=0$ to time t. Cake density is defined as:
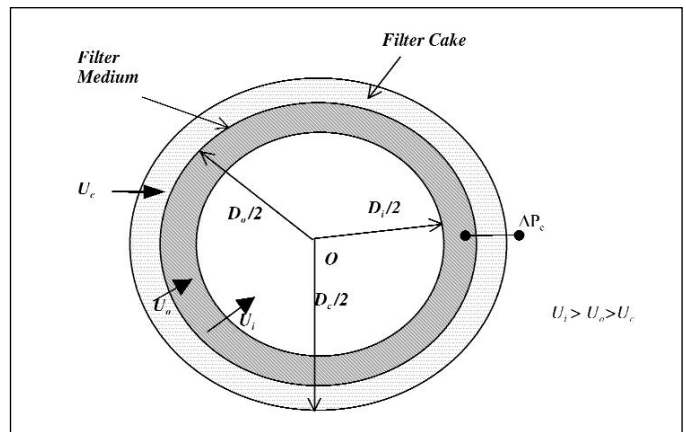
Figure 3: Schematic diagram of flow through a filter candle and filter cake.

$$\rho_c = \rho_p\,(1\text{-}\varepsilon_c) \tag{10}$$

where ρ_p is the particle density and ε_c is filter cake porosity. The outer diameter of the filter cake over Δt is then calculated as:

$$D_c(t) = D_o + \Delta x \tag{11}$$

The total pressure drop across the filter medium and dust cake is:

$$\Delta P_T = \Delta P_f + \Delta P_c \tag{12}$$

When $t = 0$, no cake is formed, the pressure difference is equal to the pressure difference across the clean filter.

$$\Delta P_T = \Delta P_f \tag{13}$$

When $t = t_1$, dust starts to accumulate on the filter surface, then

$$\Delta x_{t_1} = \int_{t_0}^{t_1} \frac{w U_c(t)}{\rho c}\,dt \tag{14}$$

$$D_{c,t_1} = D_o + \Delta x_{t_1} \tag{15}$$

$$D_{c,t_1} = D_o \int_{t_0}^{t_1} \frac{w U_c(t)}{\rho c}\,dt \tag{16}$$

The pressure difference between the filter medium and dust cake when t = t₁ is

$$\Delta P_{c,t_1} = \frac{k_2 \mu\, U_c(t_1) D_{c,t_1}}{2} \ln\left[\frac{D_{c,t_1}}{D_0}\right] \tag{17}$$

and

$$U_c(t_1) = \left(\frac{D_0}{D_{c,t_1}}\right) U_o \tag{18}$$

Rearranging equation (17);

$$\Delta P_{c,t_n} = \frac{k_2 \mu\, U_0\, D_0}{2} \ln\left[1 + \frac{\Delta x_{t_1}}{D_0}\right] \tag{19}$$

As the dust accumulates, and the changes of face velocity do not affect the structure of the dust cake, t = t_n,:

$$D_{c,t_n} = D_o + \frac{w}{\rho_c}\left[\int_{t_0}^{t_1} U_c(t)\,dt + \int_{t_1}^{t_2} U_c(t)\,dt + \ldots \int_{t_{n-1}}^{t_n} U_c(t)\,dt \right] \tag{20}$$

$$\Delta P_{c,t_n} = \frac{k_2 \mu\, U_c(t_n)\, D_{c,t_n}}{2} \ln\left[\frac{D_{c,t_n}}{D_0}\right] \tag{21}$$

Equation (21) can be rewritten as :

$$\Delta P_{c,t_n} = \frac{k_2 \mu\, U_0\, D_0}{2} \ln\left[1 + \frac{\Delta x_{t_n}}{D_0}\right] \tag{22}$$

Total pressure is then rewritten as:

$$\Delta P_{total} = \Delta P_f + \Delta P_{c,t_n} \tag{23}$$
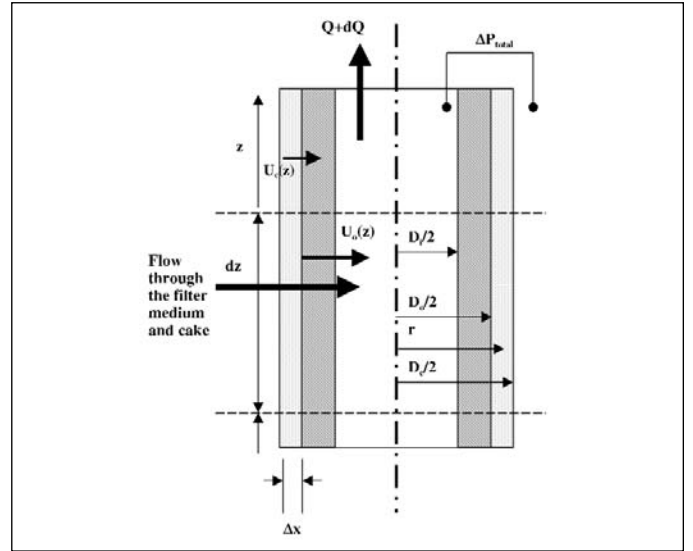
Figure 4: Schematic diagram of flow in a filter section with Filter Cake

And the resistance of flow is

$$R = \frac{(P_o - P)}{\pi D_o U_{o,z}} = \frac{(P_o - P)}{\pi D_c U_{c,z}} \tag{24}$$

where $U_o(z)$ denotes the face velocity (i.e. at the outer diameter of the medium) at position z along the axis (Figure 4). The model now can be written as equation (25) to calculate the pressure difference along the z-axis:

$$\left[\frac{\pi^2 D_i^4}{32\rho}\right] \frac{dP}{dz} = -Q(\pi D_c U_{c,z}) - \frac{fQ^2}{D_i} \tag{25}$$

The cake thickness at position z is;

$$\Delta x = \frac{\Delta z}{L} \int \frac{w U_c(t)}{p_p\,(1\text{-}\varepsilon_c)}\,dt \tag{26}$$

where L is the length of the candle.

Calculation of Cake Resistance

Cake resistance can be calculated by using the Carman-Kozeny equation, together with some assumptions. Assuming that the cake is incompressible and that the particles are spheres that barely touch, then $S_o = 6/d_p$ [5-7]. Taking the porosity of the cake as 0.85, as Schmidt [8] found that the porosity of the dust cake was constant at this value from a distance of 50μm from the surface of the filter medium upwards. The porosity can also be obtained experimentally.

Cake Porosity

The porosity of the filter cake is a very important parameter, as well as the pressure drop in the filter and the necessary force for the removal of the deposited dust layer depend on it. However, due to the high fragility of the dust cake, it is very difficult to measure experimentally. However, Aguiar and Coury [9] presented an experimental technique for measuring the porosity by adapting the work of Schmidt and Löffler [10]. Their comparisons between experimental work and theoretical equations, led them to

conclude that the Ergun correlation can be used for estimating the medium porosity with reasonable accuracy. It is then used here to estimate the cake porosity. For a dust layer of thickness, L, composed of particles with mean diameter, d_p;

$$\frac{\Delta P}{L} = 150 \frac{(1-\varepsilon)^2}{\varepsilon^3} \frac{\mu U}{d_p^2} + 1.75 \frac{(1-\varepsilon)}{\varepsilon^3} \frac{\rho U^2}{d_p} \qquad (27)$$

The mass of particles deposited on the filter is:

$$M = \dot{m}t = LA\rho_p (1-\varepsilon) \qquad (28)$$

where $\dot{m}$ is the mass flow rate of particles of density, ρ_p, A is the filtration area and t is the filtration time. Therefore:

$$L = \frac{(Qt)}{[A\rho_p(1-\varepsilon)]} \qquad (29)$$

By substituting equation (29) into the Ergun equation (27), it becomes:

$$\frac{\Delta P}{t} = 150 \frac{(1-\varepsilon)^2}{\varepsilon^3} \frac{\mu QU}{A\rho_p d_p^2} + 1.75 \frac{(1-\varepsilon)}{\varepsilon^3} \frac{\rho QU^2}{A\rho_p d_p} \qquad (30)$$

Equation (30) can then be used for estimating the cake porosity from a graph of ΔP vs. t.

Cake Detachment and Pressure Drop Analysis

Several analyses of the problem of cake detachment have been presented, *e.g.* Koch *et al.* [2]. The dust cake is assumed to be detached from the filter medium when it experiences a tensile stress sufficient to overcome either the strength of the adhesive bond between the cake and the medium (or a residual dust layer). In theory, as soon as the strength is exceeded, the cake will be detached simultaneously from the filter surface. However, in practice, the adhesive strength and the applied stress is not entirely uniform across the filter surface resulting in "patchy" cleaning.

In a rigid ceramic filter, the cleaning mechanism is different from that of the fabric filter. There is no displacement on cleaning,

therefore, the tensile stress is entirely the result of the pressure drop imposed across the cake due to the reverse flow of cleaning gas. Koch et al. [11] determined the range of tensile stresses over which the cake detaches from the filter medium using a small flat "coupon" of filter medium. Results from the coupon test were plotted in the form of "percentage cake remaining" versus "applied stress", where the applied stress is the appropriate value of the pressure drop across the cake. The curve provided the information needed for selection of a cleaning pressure. Figure 5 shows an example of such curve that might be used in practice. On the left-hand side is a set of cake detachment curves, on the right an imaginary axial distribution of cleaning pressure. If the measured cake detachment stress curve is 'a', then most of the cake will be removed by the pulse; if it is 'c', then very little will. Aguiar and Coury [12], working on detachment of phosphate rock dust from a polyester fabric, showed a good prediction of the cake detachment stress by this approach. The expression σ was then modified by Aguiar and Coury [9] as:

$$\sigma = n_c F_{ad} \qquad (31)$$

where F_{ad} is the force of adhesion between two particles and n_c is the average number of particle-particle contacts per unit area:

$$n_c = 1.1(1-\varepsilon)\varepsilon^{-1}d_p^{-2} \qquad (32)$$

In the case of dry and inert agglomerates, without the presence of binders or electrostatic charges, the forces of adhesion between the particles are usually due to Van der Waals interactions. For two spheres of the same diameter, d_p, the force can be described as:

$$F_{ad} = \frac{Hd_p}{(24a^2)} \qquad (33)$$

where H is the Hamaker constant, which depends on the particle composition (and has a value around 8 x 10^{-20} J, for most materials of interest [5] and a is the distance of separation
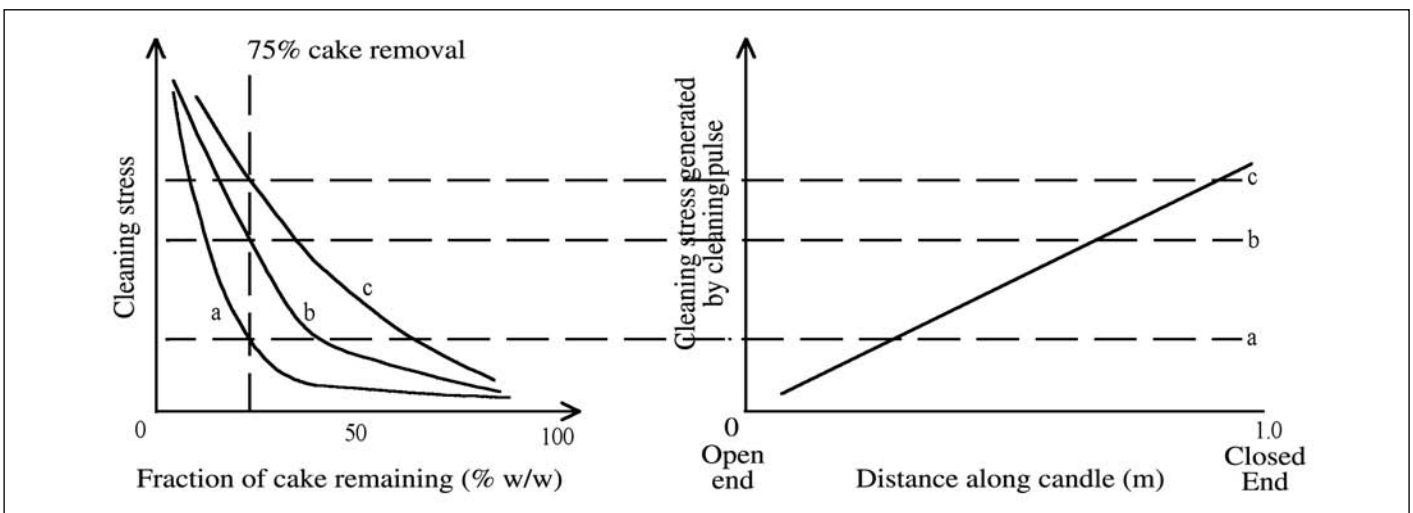

Figure 5: Variation of cake removal with axial position on candle. 'a' indicates the path of cake detachment stress where most of the cake will be removed. If it is on path 'c', very little cake will be removed (Seville, 1999).

Table 1: Parameters used in simulations.

Length of filter, L (m)	1	Resistance to flow, R (Ns/m^4)	22290 (open end) 43120 (closed end)
Inner diameter, D_I (m)	0.042m	Particle density, Limestone, ρ_p (kgm^{-3})	2500
External diameter D_O (m)	0.062	Dust concentration, w (kgm^{-3})	0.01026
Gas viscosity μ (kgm^{-1}s^{-1})	1.7894 x10^{-5}	Cake porosity, ε	0.85
Gas density, ρ_g (kgm^{-3})	1.225	Time interval , Δt (s)	300

between the surfaces of the particles. The cake removal stress can then be written as:

$$\sigma = 0.046 \frac{(1-\varepsilon)\, H}{\varepsilon d_p} \frac{1}{a^2} \qquad (34)$$

RESULTS OF SAMPLE CALCULATIONS

A large number of sample calculations were made to ensure that procedures outlined above were valid and workable. The calculation is done by Fortran 90 programming. Some of the results obtained are presented in the following sections. In Table 1, the conditions used for the calculations are outlined. The physical dimensions used here were taken from the previous work of pilot plant study. The carrier gas, air, was taken to be incompressible over the pressure range of interest.
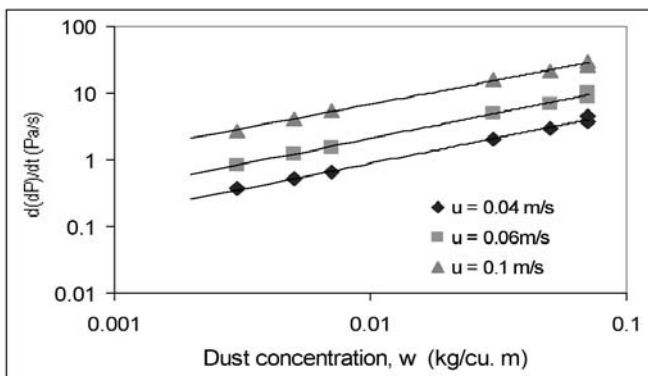

Figure 6: Relationship between the pressure drop increasing rate and the dust concentration under ambient conditions.
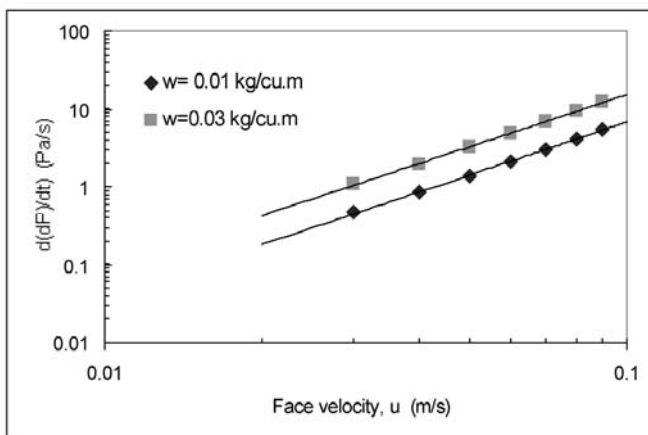

Figure 7: Relationship between the pressure drop increasing rate and the face velocity under ambient conditions.

As discussed previously, the method developed enables one to calculate the total pressure across the filter medium and filter cake. The thickness of the filter cake forming on the surface of the medium for a given face velocity with a constant particle concentration can also be calculated. The concentration w is directly proportional to the total amount of particles to which the filter media are exposed and is the independent variable.

Relationship of Dust Concentration and Face Velocity

The properties of the dust cake formed during filtration depend mainly on the filter face velocity, the filter medium, gas temperature and in particular, the particle properties. An essential feature is the pressure drop in connection with the permeation of the dust cake.

The pressure drop across the cake, ΔP_c depends on the dust concentration and the face velocity. As ΔP_c increases with time, it is more appropriate to use the rate of increase of the pressure drop, $d\Delta P_c/dt$, to express the influence of these factors. By solving those equations described in the section before, which enable the calculation of the pressure drop across the filter cake for the whole filter (*i.e.* for $z = 0$ to L), the relationships between the rate of increase of the pressure drop and the dust concentration and the face velocity are plotted respectively.

Figure 6, which shows the relationship between the rate of increase of the pressure drop (from the simulation) and the dust concentration under ambient condition, confirming, as expected, that $d\Delta P_c/dt$ is proportional to the dust concentration.

Figure 7 shows the relationship between $d\Delta P_c/dt$ and the face velocity. $d\Delta P_c/dt$ (from the simulation) is proportional to the second power of the face velocity, which follow directly from the Carman-Kozeny equation, which can be rewritten as:

$$\frac{\Delta P}{dL} = \frac{(1-\varepsilon)^2\, S_o^2}{\varepsilon^3} \mu u \qquad (31)$$

Therefore, for constant dust concentration,

$$\frac{d\Delta P}{dt} = \frac{(1-\varepsilon)^2\, S_o^2}{\varepsilon^3} \mu u \qquad (32)$$

EFFECT OF THE FACE VELOCITY ON THE CAKE THICKNESS

The cake thickness distribution along the filter surface for different face velocities after an hour of filtration is shown in Figure 7. For those discrete "steps" as seen, corresponding to the five sections of resistance into which the filter was divided for the purpose of the calculation. Each section has a different resistance value. Due to the influence of different local face velocities in the sections along the filter axis this lead to different cake deposition rates at the filter surface.

At higher face velocity, the cake thickness increased dramatically. However, the distribution of the cake thickness was not uniform at any face velocity. The variation in the thickness at different positions on the filter was caused by the non-uniform
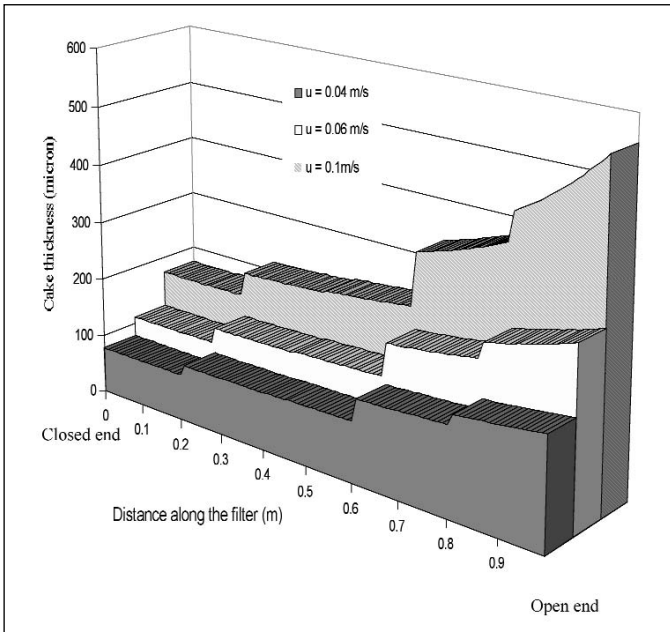
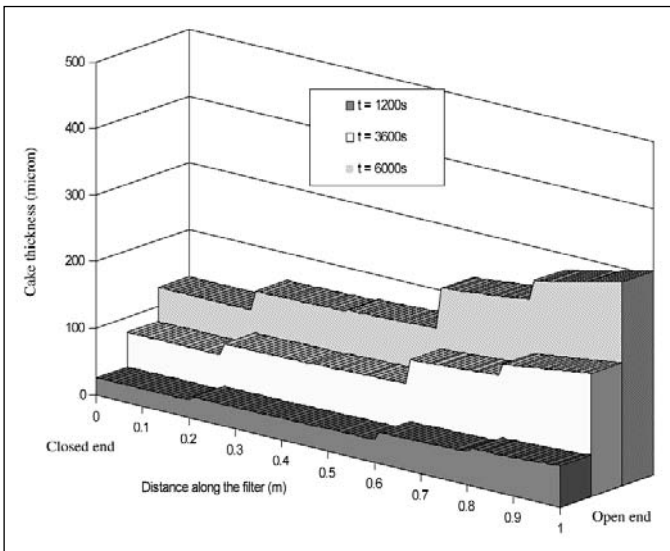*Figure 8: Relationship between the filter cake thickness and the face velocity (t=1 hr) under ambient conditions.*

Figure 9: Effect of filtration time on the cake thickness (u = 4 cm/s).

velocity distribution. At a face velocity of 4 cm/s, deposition of dust was more uniform throughout the filter medium than at higher velocities. Dust layers were found to be less than 100μm thick at less than 60cm from the closed end, but much thicker close to the open end. As for the face velocity of 10 cm/s, the dust cake accumulated rapidly at the open end of the filter due to the higher velocity there.

Effect of Filtration Time on the Cake Thickness

The distribution of dust cake thickness with time is shown in Figure 9. As expected, with increasing time the accumulation of dust on the filter surface also increased. Deposition of the dust cake became less uniform on the filter as time increased.

Figure 10 shows the relationship of dimensionless cake thickness, $h/\bar{h}$, along the filter with time ($\bar{h}$ is the average cake thickness). During the early stages of filtration, the cake thickness increment was non-uniform ($t = 1200$s). But at the longest filtration

time, more uniform increments in thickness were seen ($t = 3600$s). The accumulation of the dust over the filter surface was low at the closed end and was higher close to the open end. Figure 11 illustrates a schematic diagram of cake build up on the surface over time. At the beginning of the filtration ($t = 0$), no dust cake was formed. When $t = t_1$, the dust deposited on the filter surface and formed a cake layer at the open end of the filter. At $t = t_n$, the
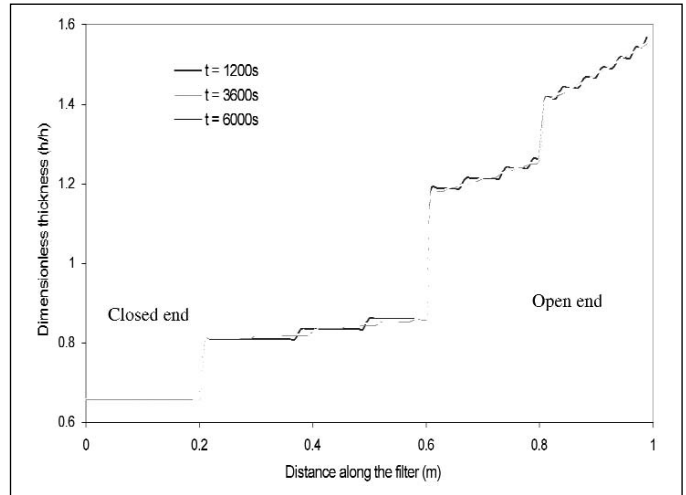
Figure 10: Dimensionless thickness vs. time.
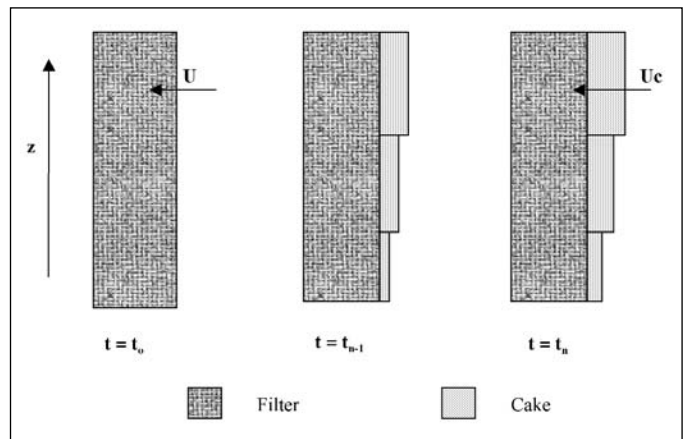
Figure 11: Schematic diagram of cake build-up. The distribution over time is shown by the varied patterns.

dust layer covers the whole surface of the filter and the previous dust layer becomes thicker as more particles deposit on it. In other words, the cake grows from the open end towards the closed end with more particles deposited at the open end due to the higher velocities, hence giving a thicker cake.

Relationship between Cake Velocity Distribution and Cake Thickness

Figure 12 shows the relationship between dust cake deposition and velocity distribution. A non-uniform velocity profile along the filter was observed at $t=900$s which mirrors the non-uniform local velocity distribution.

Effect of Friction Factors

Figure 13 shows the effect of the friction factor on the total pressure difference. The friction factor makes little contribution to the pressure difference for $f =0.05$ and 0.1 up to a distance of 60
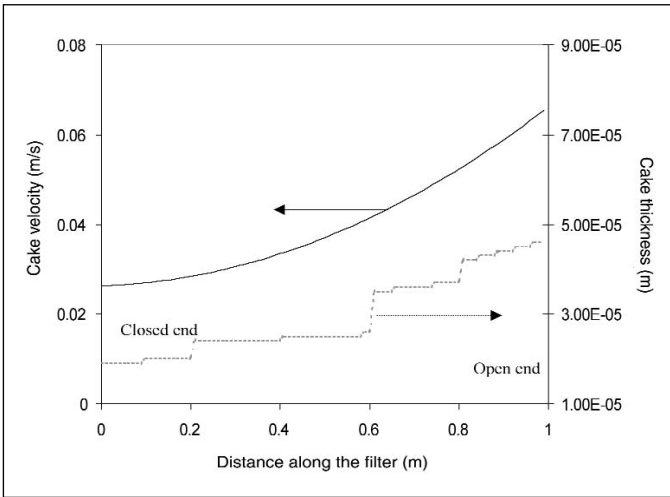
Figure 12: Relationship between the velocity distribution and dust cake thickness at t = 900s (u = 4cm/s).
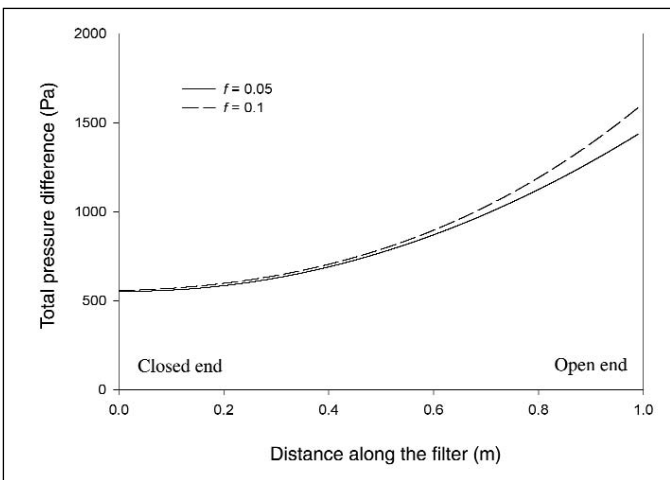
Figure 13: Effect of friction factors on total pressure difference (u=4cm/s).

cm from the closed end. The effect on the pressure difference increased close to the open end, because of the high velocities in this region. (As noted earlier, the frictional pressure drop is roughly proportional to the square of velocity). At this distance the pressure drop caused by friction had been increased. Due to the higher volumetric flowrate with the increasing distance, the momentum of gas flow was also increased. The frictional term will then dominate. At a higher friction factor, the effect on the pressure difference was more significant.

Cake Detachment Simulations

The assumption made in this simulation was that when the pressure difference across the cake exceeds the "detachment stress", detachment of the cake occurred. The detachment stress depends on various factors, including the particle size distribution in the cake, the chemical composition of the particles and temperature. The bonding forces that may occur between the filter medium and the dust cake may increase with time due to the possibility of deformation and sintering of particles [13]. To simplify the model, assumptions of constant cake detachment stress and an incompressible cake were applied.

When the removal stress was applied to the filter, some areas

of the filter cake may not be detached as they possess a higher detachment stress. The older cake layers remaining on the surface will then be covered by the new dust layers as time proceeds. Hence, thicker cake layers will be formed. The detachment stress for the dust cake was determined accrording to equation (34). By applying the reverse flow model described by Stephen [14] and Clift *et al.* [15], the applied cleaning stresses on the filter was calculated at various reverse flow volumetric flowrates.

EFFECT OF REVERSE FLOW VOLUMETRIC FLOW RATE

The distribution of dust cake thickness with different reverse volumetric flowrates, are shown in Figure 14 (face velocities 4 cm/s) and Figure 15 (face velocities 6 cm/s). As can be seen in the figures, the dust cake remained in the area near the open end, because the applied stress was lower than the detachment

Figure 14: Cake detachment after reverse flow cleaning with a face velocity of 4cm/s.

Figure 15: Cake detachment after reverse flow cleaning with a face velocity of 6 cm/s.

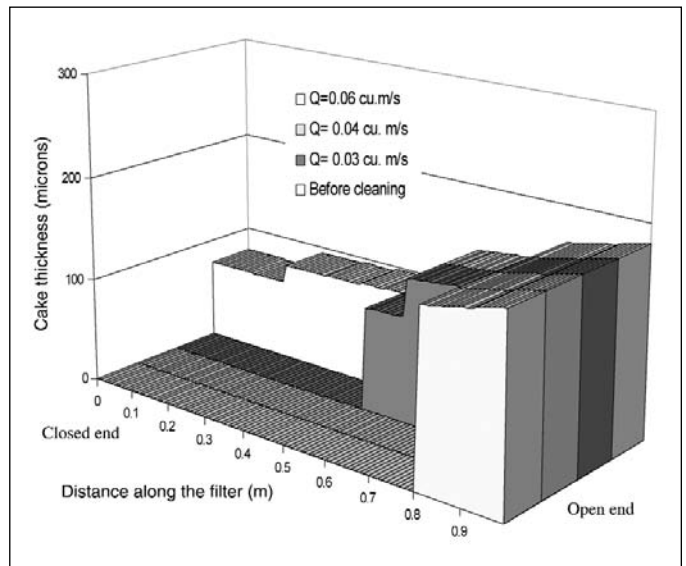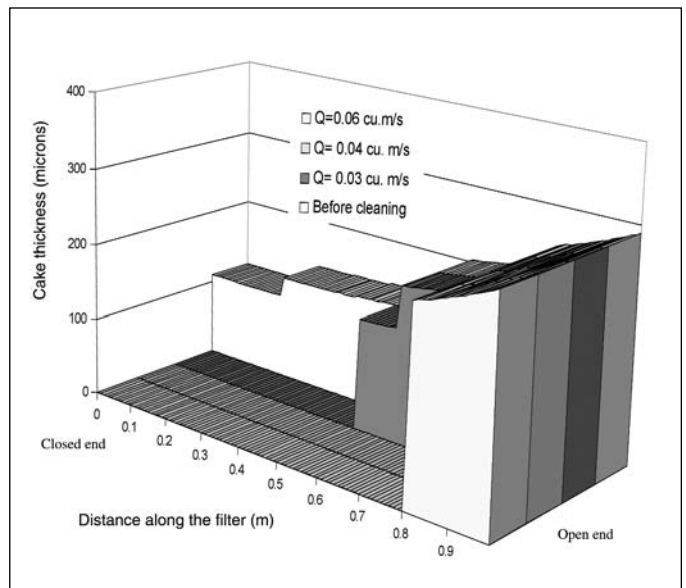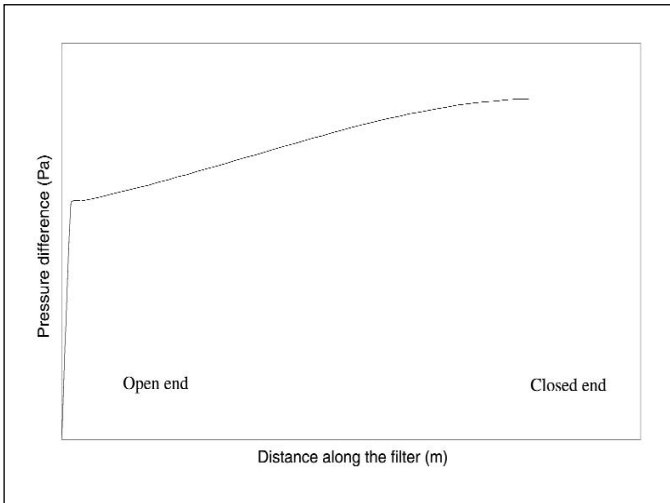*Figure 16: Schematic of diagram of pressure difference distribution of reverse flow cleaning.*
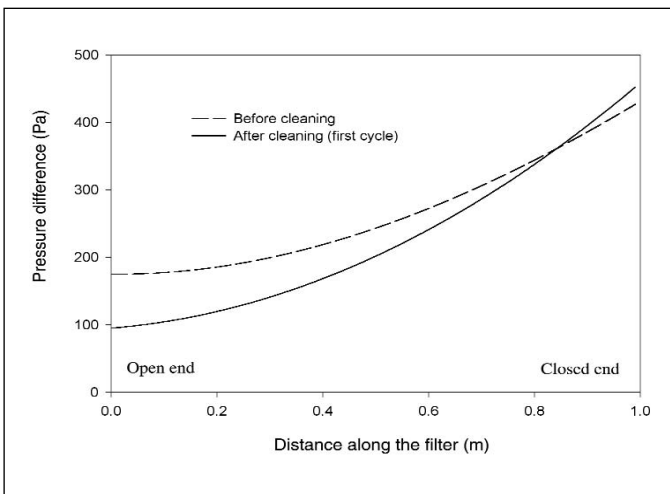

Figure 17: Pressure difference distribution before and after first cycle of cleaning in filtration mode.

stress of the dust cake in that region. Higher volumetric cleaning flow rates will improve the cleaning condition on the filter. However, even at the highest flow rate some fraction of the dust cake still remained on the filter. Detachment of the filter cake occurs more readily at the bottom of the candle because that was where the applied detachment stress was the highest (see Figure 16).

CONDITIONING OF THE FILTER

Figure 17 shows the pressure difference profile before cleaning and after the first cleaning cycle. The pressure drop was reduced in the area where dust cake had been removed. However, close to the open end the pressure drop was increased, due to the fraction of uncleaned dust cake remaining. Now "younger" dust cake will deposited on top of the older filter cake layer, hence increasing the pressure drop.

Using the numerical model, the pressure drop was simulated as a function of time in order to analyse the filter conditioning. Figure 18 shows the simulated pressure difference history for the first five cycles of the filtration with a face velocity of 4 cm/s. The filter was cleaned when the pressure reached 400 Pa. The calculated results show a similar conditioning profile on the rigid
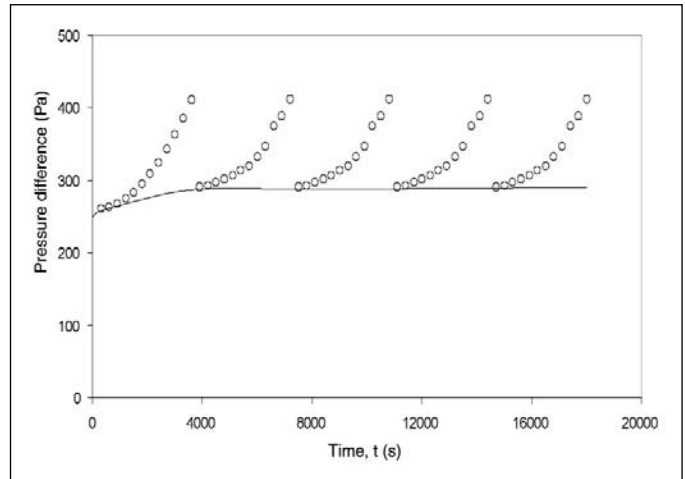
Figure 18: Simulated pressure difference vs. filtration time for a sequence of filtration cycles (4 cm/s).

ceramic filter comparable to the previous findings [16, 17]. The non linear curve indicates that non-homogeneous cake cleaning was occurring throughout the filtration. However, there was not much difference between successive filtration cycles.

CONCLUSIONS

A model has been developed for the combined processes of filtration and cake detachment, incorporating non-uniformity of cake thickness in the axial direction. Results from the cake build-up and detachment model gave an idea of the conditioning process and the development of patchy cleaning on the filter surface.

This model can also be further modified to study the pressure distribution for the compressible dust cake. The detachment stress of the cake depends on various factors, such as particle size distribution in the cake, the chemical composition of the particles, temperature, *etc*. They should also be considered in the improvement of the model. Experiments should also be carried out in order to improve the model under more realistic operation parameters.

REFERENCES

[1] J. P. K. Seville, W. Cheung and R. Clift, A Patchy-Cleaning Interpretation of Dust Cake Release From Non-Woven Fabric, *Filtration and Separation,* 26(2), 187-190 (1989).

[2] D. Koch, J. P. K. Seville and R. Clift, Dust Cake Detachment from Gas Filters, *Power Technology,* 86, 21-29 (1996).

[3] C. Tien, R. Bai and B. V. Ramarao, Analysis of Cake Growth in Cake Filtration: Effect of Fine Particle Retention, *AIChE J.,* 43(1), 33-44 (1997).

[4] J. P. K. Seville, R. Clift, C. J. Withers and W. Keidel, Rigid Ceramic Media for Filtering Hot Gases, *Filtration and Separation,* 26(3), 265-271 (1989).

[5] J. P. K. Seville, U. Tuzun and R. Clift, *Processing Solid Particulate Solids,* pp. 261-297 Blackie Academic and Professional, Glasgow (1996).

[6] H. E. Hesketh, *Fine Particles in Gaseous Media,* pp. 109-113, Lewis Publishers, Inc.,Michigan (1986).

[7] K. Ushiki and C. Tien , Analysis of Filter Candle Performance, *Powder Technology,* 58, 243-258 (1989).

[8] E. Schmidt, Simulation of Three Dimensional Dust Cake Structures via Particle Trajectory Calculations for Cake-Forming Filtration, *Powder Technology,* 86, 113-117 (1996).

[9] M. L. Aguiar and J. R. Coury, Cake Formation in Fabric Filtration of Gases, *Ind. Eng. Chem. Res.,* 35, 3673-3679 (1996).

[10] E. Schmidt and F. Löffler, Preparation of Dust Cakes for Microscopic Examination. *Powder Technology,* 60, 173-177 (1990).

[11] D. Koch, K. Schulz, J. P. K. Seville and R. Clift, Regeneration of Rigid Ceramic Filters, in: *Gas Cleaning at High Temperatures,* R. Clift and J. P. K. Seville (Eds), pp. 244-265, Blackie Academic & Professional, London (1993).

[12] M. L. Aguiar and J. R. Coury, Air Filtration in Fabric Filters: Cake-Cloth Adhesion Force, *Journal of Fluid/ Particle Separation,* 5, 193-198 (1992).

[13] W. Duo, J. P. K. Seville, N. F. Kirkby, H. Büchele, and C. K. Cheung, Patchy Cleaning of Rigid Ceramic Filters. Part 1: A Probabilistic Model, *Chemical Engineering Science,* 52(1), 141-151 (1997).

[14] C. M. Stephen, Filtration and Cleaning Behaviour of Rigid Ceramic Filters, PhD Thesis, University of Surrey (1997).

[15] R. Clift, J. P. K. Seville and J. W. W. ter Kuile, Aerodynamic Considerations in Design and Cleaning of Rigid Ceramic Filters for Hot Gases in: *Proc. of 5th World Filtration Congress,* pp. 530-537. Nice (1990).

[16] Duo, W., Kirkby, N. F., Seville, J. P .K., Clift, R. (1997b). "Patchy Cleaning of Rigid Ceramic Filters. Part 2: Experiments and Validation". Chemical Engineering Science, 52(1), pp. 153-164.

[17] Grannell, S. K. (1998). "The Industry Application of Low Density Rigid Ceramic Filters for Hot Gas Cleaning". PhD Thesis, University of Birmingham.

NOMENCLATURES

a	distance of separation between the surfaces of the particles	m
D_i	filter inner diameter	m
D_o	filter outside diameter	m
d_p	particle diameter	m
F	total shear force	N
F_{ad}	adhesion force	N
f	Fanning friction factor	-
H	Hamaker constant	J
h	Cake thickness	m
k_1	first Ergun equation constants	$kg^{-1}m^{-1}$
k_2	second Ergun equation constant	m^{-1}
L	length of the filter section	m
M	total massretained in the filter system.	kg
$\dot{m}$	mass flowrate	kg/s
n_c	average number of particle-particle contacts per unit area	m^{-2}
P	pressure	$N\,m^{-2}$
D_{Pf}	pressure dropover filter medium	$N\,m^{-2}$
D_{Pc}	pressure drop over cake	$N\,m^{-2}$
DP_T	pressure drop over cake plus medium	$N\,m^{-2}$
Q	actual volumetric flow rate	$m^3\,s^{-1}$
R	specific resistance	m^{-1}
r	radius	m
S_o	specific surface area	m^{-1}
Δt	time interval between (t-1) and t	-
U	superficial gas velocity	$m\,s^{-1}$
u	gas velocity	$m\,s^{-1}$
w	areal cake loading	$kg\,m^{-2}$
Δx	cake thickness	m
Δz	incremental distance	m

GREEK

ε	porosity	-
εc	cake porosity	-
μ	fluid viscosity	$kgm^{-1}s^{-1}$
ρ	fluid density	$kg\,m^{-3}$
ρ_c	cake density	$kg\,m^{-3}$
ρ_g	gas density	$kg\,m^{-3}$
ρ_p	solid (particle) density	$kg\,m^{-3}$
σ	cake removal stress	$N\,m^{-2}$

Hazards Analysis of LPG Storage Installation in Universiti Putra Malaysia: A Preliminary Study

[1]El-Harbawi M., [1]Sa'ari M, [1]Thomas Choong S. Y., [1]Chuah T. G. and [2]Abdul Rashid M. S.

[1]Department of Chemical and Environmental EngineeringFaculty of Engineering, Universiti Putra Malaysia, 43400 UPM Serdang, Selangor.

[2]Department of Agricultural and Biological Engineering, Faculty of Engineering, Universiti Putra Malaysia, 43400 UPM Serdang, Selangor.

ABSTRACT

A preliminary risk analysis on the impact of LPG storage explosion to the community in the Faculty of Engineering, Universiti Putra Malaysia (UPM) is studied. This paper is aimed to evaluate the physical effects of the release of hazardous substances or energy following various possible accidental events. This paper focuses on the final events that are: confined explosion fireball/ boiling liquid expanding vapour explosion (BLEVE), jet-fire and pool-fire. Several physical models including Trinitrotoluene (TNT) model are used to evaluate each possible accident and the calculated results of the affected area and distance are also shown.

Keywords : *LPG, confined explosion, BLEVE, jet-fire, pool-fire, TNT model, GIS*

INTRODUCTION

The rapid growth in the use of hazardous chemicals in the industry has brought significant increase of risk to a number of people, both workers and public, whose life could be endangered at any one time by accident involving these chemicals [1]. Risk analysis is a discipline, which has constantly been gaining interest almost three decades among the process industry community. Especially concerning to the major industrial accidents that occurred during the years, such as Flixborough (1974), Seveso (1976), Mexico City (1984), Texas (1989), Kuwait (2000), Lincolnshire (2001) and Shandong, (2003), contributed to that interest. Malaysia also had experience in some major accidents, such as the explosion and fire of at the firecracker plant (Bright Sparkle), the explosion of ship-tanker loaded with hydrocarbon at Port Klang Shell Depot and recently the explosion of fertilizer's warehouse at Port Klang, Malaysia [2].

Storage and transportation of dangerous substances have defined the set of risk sources, which are located on territory, called impact area. Release of chemical due to accident could be severe and poses an immediate effect to workers on-site and communities off-site as well as the potential to adversely affect the environment. Liquefied petroleum gas (LPG) is a very important fuel and chemical feed stock. However, it also causes major fires and explosions. For bulk storage and bottling of liquefied petroleum gas (LPG), there are 11 major hazards installations (MHI) and 150 non-major hazard installations (NMHI) as categorized under Control of Industrial Major Accident Hazards (Amendment) Regulations, 1990 (CIMAH) [2]. These incidents can be unconfined vapour cloud explosions, confined explosions, boiling liquid expanding vapour explosions and fires. The causes of these losses have involved chemical accidents, overfilling of containers, and loading and sampling operations. Several physical models can be used to calculate and to predict the physical effects of explosion and fire from LPG accidents. Furthermore, the area affected can also able be predicted.

A preliminary risk analysis on the impact of LPG storage explosion to the community in the Faculty of Engineering, Universiti Putra Malaysia (UPM) is studied. The Faculty of Engineering of Universiti Putra Malaysia is located at the Serdang Campus, some 22 kilometres to the south of Kuala Lumpur, currently as one of the largest faculties at UPM with student enrolment of 3000. The LPG storage tank is to be installed as part of the second phase development project of faculty facilities. The storage tank is in cylindrical shape, with capacity of 120 tones. The dimensions of the vessel are 30 m in length and 4 m in height.

Geographical Information System (GIS) is used as a tool to provide geographical information of the potential affected areas in order to evaluate the consequences or impact of the disaster. The functionality of GIS enables the integrated model to handle the data management, computational aspects and the integrated needs as emphasised in the hazards approach. The role of the GIS, therefore, is to allow a modeller to visualize development changes to the landscape and to produce resultant input values for the individual models and create a map of a target source. The affected area in vicinity of the LPG storage tank in UPM was identified by using ArcView 8.3 software. ArcView 8.3 can be use easily to create maps and to add the data to them. Using ArcView software's powerful visualization tools, one can access records from existing databases and display them on maps.

RISK ANALYSIS IN LPG INSTALLATION

The scope of this paper is to evaluate the physical effects of the release of hazardous substances or energy following the possible accidental events. The evaluation of each release is represented using cause-consequence diagrams, Event Tree, that starting from the initial accident event eventually build all the plausible scenarios. Figure 1 shows the event tree for LPG released and the probabilities for the various possible of the events [3]. This paper focuses on the final events that are: vapour cloud explosion (VCE), boiling liquid expanding vapour explosion (BLEVE) and fire.

Explosion Hazards

The main hazard from explosion is the blast wave. A blast wave is the result of an explosion in air that accompanied by a very rapid rise in pressure. Pressure effects are usually limited in magnitude and are thus of interest mainly for prediction of domino effects on adjacent vessels and equipment rather than for harm to neighbouring communities. The blast effects can be estimated from the TNT equivalence method. Table A1 presents criteria for assessing the likelihood of eardrum rupture occurring as a result of exposure to blast wave overpressures [4]. The pressure effects on humans due to blast waves [5] are presented in Table A2. Pressure effects are usually limited to a small area and the effect of pressure on the environment is therefore seldom discussed. However, the same discussion as for humans is also valid, for both the general environment and animals; namely any adverse effects or injuries are more dependent on them being hit by a flying object. Table A3 describes the types of damage that may occur to various construction types as a result of exposure to various levels of peak side-on overpressure. As illustrated, significant damage is expected for even small overpressure [5].

A confined explosion occurs in a confined space, such as a vessel or a building. A confined explosion is a result of a rapid chemical reaction, which is constrained within vessels and buildings. Dust explosions and vapour explosions within low strength containers are one major category of confined explosion [3]. A basic distinction between confined explosions and unconfined explosions is confined explosions are those which occur within some sort of containment. Often the explosion is in a vessel or piping, but explosions in buildings also come within this category. Explosions, which occur in the open air, are unconfined explosions.

The calculation models of peak overpressure are primarily based on broad approaches. The simplest model is the TNT equivalence method. TNT model is based on the assumption of equivalence between the flammable material and TNT, factored by an explosion yield term [6]. TNT model is based on the assumption of equivalence between the flammable material and TNT. An equivalence mass of TNT is calculated using the following equation [7]:

$$m_{TNT} = \eta\, M\, \Delta H_c\, /\, E_{TNT} \tag{1}$$

The distance to a given overpressure is calculated from the equation [8]:

$$r = 0.367\ x\ m_{TNT}^{1/3}\ exp$$
$$\left[3.531 - 0.7241\ 1n(p_o) + 0.0398(1np_o)^2\right] \tag{2}$$

Table 1: Peak overpressure vs. distance for blast wave from an explosion

r(m)	p^o(kPa)
100	94.22
200	27.61
300	14.64
400	9.60
500	7.01

The TNT equivalence predicts peak overpressure with distance. It should be noted that the pressure depends strongly on the distance between the place of the explosion and the structure. The consequence is that explosion of the same explosive charge can cause very different overpressures depending on the location of the explosive charge.

Boiling Liquid Expanding Vapour Explosion (BLEVE)

Boiling Liquid Expanding Vapour Explosion (BLEVE) occurs when there is a sudden loss of containment of a pressure vessel containing a superheated liquid or liquefied gas. A BLEVE is a sudden release of a large mass of pressurized superheated liquid to the atmosphere. Formulas to estimate the BLEVE physical parameters are as follow [6]:

$$D_{max} = 6.48M^{0.325} \tag{3}$$

$$t_{BLEVE} = 0.825M^{0.26} \tag{4}$$

$$H_{BLEVE} = 0.75\ D_{max} \tag{5}$$

$$D_{initial} = 1.3\ D_{max} \tag{6}$$

Table 2: The resuts of BLEVE physical parameters

D_{max}(m)	t_{BLEVE}(s)	H_{BLEVE}(m)	$D_{initial}$(m)
289.94	17.26	217.46	376.92

A fireball is assumed to be spherical and resting on the ground. The radius is given by equation (3). The model is described in detail on the work of Roberts [9] and Fay J. and Lewis D. [10]. One of the simplest practical models for evaluating fireball hazards is the point source model. This has been used to estimate the intensity of thermal radiation from the resulting fireball. This model estimates the emissive power as a function of the combustion mass [11]. Fireball composition occurs when volatile hydrocarbons are released and rapidly ignited. In calculating the quantity of LPG participating in the fireball the complete content of the tank is generally taken into account. The radiation received by a target (for the duration of the BLEVE incident) is given by [9]:

$$Q_{t\,arg\,et} = \tau\, E\, F_{21} \tag{7}$$

Thermal radiation is absorbed and scattered by the atmospheric. Pieterson and Huerta [12], recommend a correlation formula that account for humidity:

$$\tau = 2.02\ (P_w l)^{-0.09} \tag{8}$$

The path length, distance from flam surface to target is:
$$l = \left[H^2_{BLEVE} + r^2\right]^{0.5} - \left[0.5D_{max}\right] \tag{9}$$

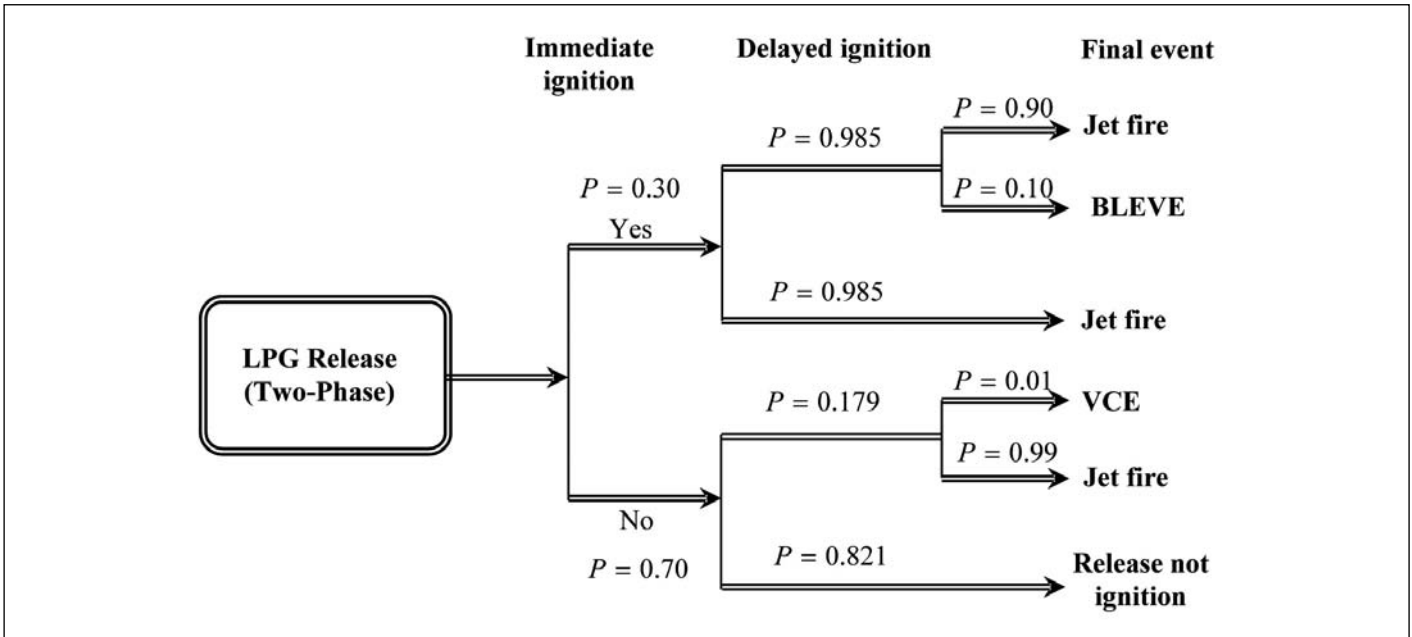Thermal radiation is usually calculated using surface emitted flux, E:

Figure 1: Typical Event Tree (ET) for a flashing liquid continuous release [3]

$$E = \frac{F_{rad} M \, \Delta H_c}{\pi (D_{max})^2 \, t_{BELVE}} \qquad (10)$$

The radiation fraction, F_{21} was given by Roberts [9] in the range of 0.25-0.4. As the effects of a BLEVE mainly relate to human injury, a geometric view factor for a sphere to the surface normal to the sphere (not the horizontal or vertical components) should be used:

$$F_{21} = \frac{D^2_{max}}{4r^2} \qquad (11)$$

BLEVE hazards are not dependent on wind speed, wind direction, or atmospheric stability [13].

Pool Fires and Jet Fires

Pool fires and jet fires are common fire types resulting from fires over pools of liquid or from pressurised release of gas and/or liquid. Pool fires are the result of spillage or leakage from tanks, pipelines, or valves. The total heat release rate of the fire can be calculated as following [14]:

$$Q_r = \zeta \, m \, \Delta H_c \, A_p \qquad (14)$$

$$m = M_\infty \left[1 - exp\,(-kD) \right] \qquad (15)$$

The mass burning rate per unit area for an infinite pool, $m\infty$ is taken as 0.099 and it is dependent on the diameter of the pool. The pool diameter is calculated as following: Around the rupture location the LPG spreads out and forms a pool 2cm high [15].

$$A_p = V/0.02 \qquad (16)$$

$$D = \sqrt{\frac{4}{\pi} \times A_p} \qquad (17)$$
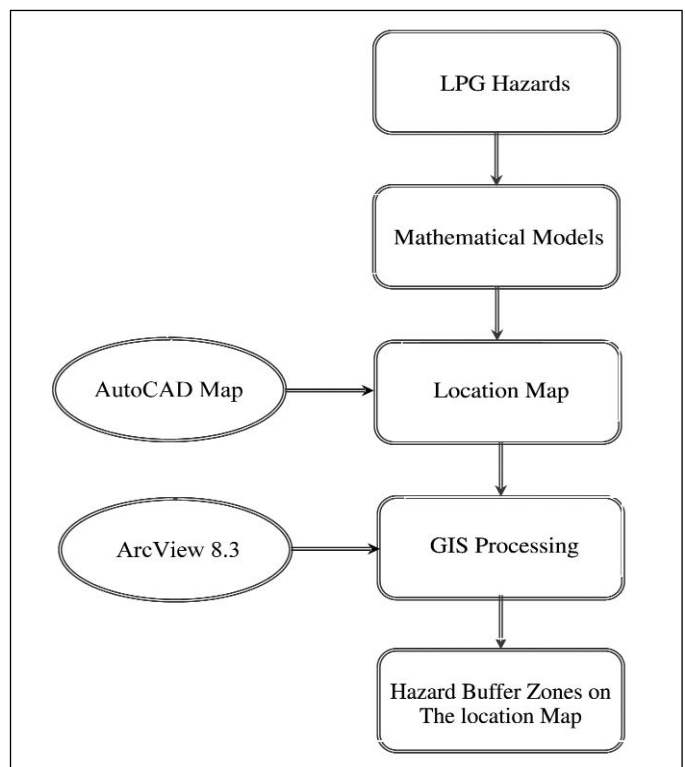

Figure 2: Logic diagram for the estimating LPG hazards by using GIS

The flam high can be estimated from:

$$\frac{L_f}{D} = 42 \left(\frac{m}{\rho_a \sqrt{gD}} \right)^{0.61} \qquad (18)$$

The heat that is radiated from the pool fire is a fraction of the total amount release:

$$Q_R = \kappa Q_T \qquad (19)$$

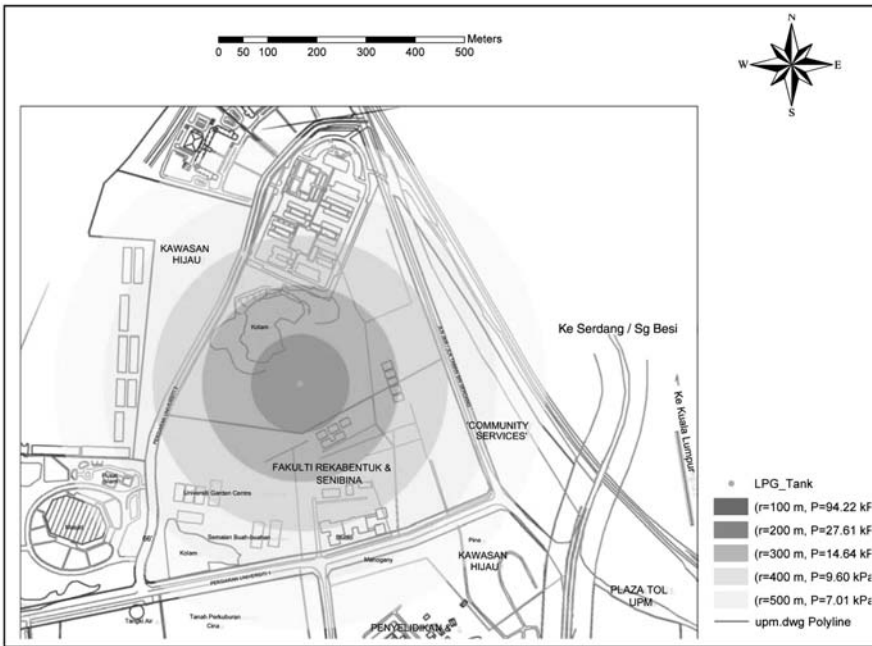where κ is the fraction of total heat emitted as radiation.
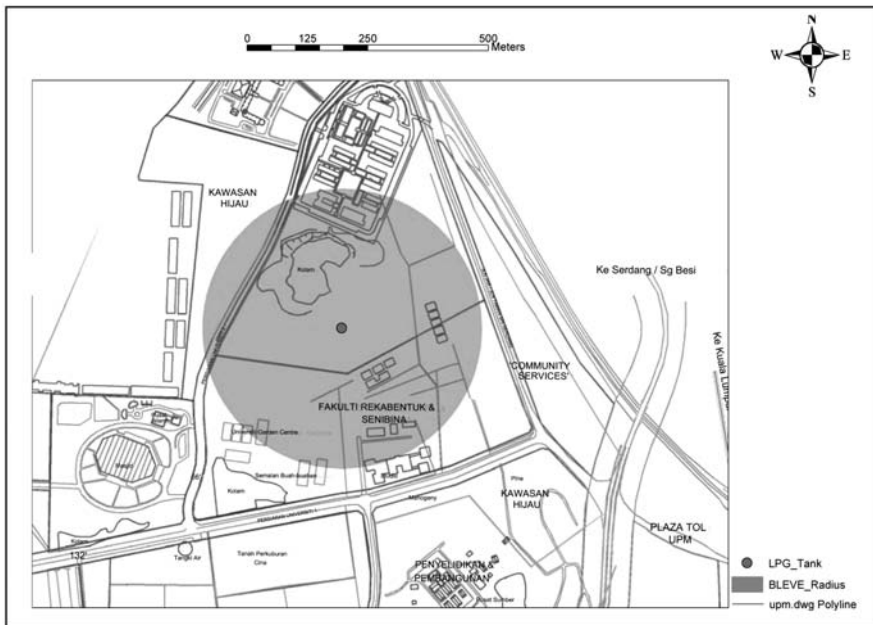
Figure 3: Peak overpressdure buffer zones

Figure 4: BLEVE/Fireball radius

BUILDING THE GIS DATABASE

A substantial portion of the GIS database came from map source documents, while many other sources, such as aerial photos, tabular files, and other digital data can also be used. The map representation is only part of the GIS database, in addition, a GIS can hold scanned images (drawings, plans, photos), references to other objects, names and places and derived views from the data. Building a database consists of three major steps: identifying the geographic features, attributes, and required data layers; defining the storage parameters for each attribute; and ensuring co-ordinate registration. The collection of cartographic data can be achieved by any of these alternative procedures: extant maps through digitizing or scanning, photogrammetric procedures or terrestrial surveying measurements. AutoCAD is used as a tool in map drawing for LPG tank location and the vicinity and the scale is 1: 6,000. The procedures of estimating the hazard buffer zones are shown in Figure 2.

RESULTS AND DISCUSSION

This study aims to estimate the impacts due to installation of a LPG tank, at Faculty of Engineering, UPM. Expected consequences and the actions proposed to be taken in order to evaluate the probable effects to human and environment in the surrounding area also will be discussed. From the TNT modelling, it can be noted that the pressure depends strongly on the distance between the place of the explosion and the structure. The consequence is that the explosion of the same explosive charge can cause very different overpressures depending on the location of the explosive charge. Pressure dependsalso on the location of the explosive charge above the ground. Table 1 shows the peak overpressure results for different distances for material release. The areas affected include laboratories, classes, offices, roads, students' hostels and areas in the vicinity of Serdang Town. The resulting damage to the surrounding area is cased by a blast wave generated by an explosion event. The major effect of the hazards will be investigated in the area with radius of 500 m of LPG tank. The results in Table 1 are then referred to the Tables A1, A2 and A3 to estimate the overpressure effect on human. It is clearly seen that the major effect of overpressure generated by blast wave will affect a human being in area with radius of 200 m. It is estimated more than 10% likelihood of eardrum rupture and man may receive several fatal not only from direct exposure to the blast wave, but hit by the falling objects from the demolished structures.

Geographical data and results of hazards estimation of LPG tank of the Faculty of Engineering, UPM, are analyzed via the program of ArcView 8.3, a GIS and mapping software, in order to provide data visualization, query and analysis on the hazard of LPG tank. Figure 3 shows the peak overpressure buffer zones using ArcView 8.3 software. The buffer zones have been drowning for different peak overpressure values. It can easy classify the map to different zones depend on the pressure effects.

The major effect of thermal effect resulted from BLEVE. Thermal radiation from BLEVE can cause severe harm and damage to human and construction. The results for fireball characteristics are summarized in Table 2.

Most of the heat radiation will appear in the fireball radius. Within this radius, there will be severe damage to buildings and able to bring harm to humans. The intensity of thermal radiation from resulting fireball has been estimated from point source model. The modelling results are summarized in Table 3. In order to calculate the quantity of LPG participating in the fireball, the complete content of the tank is generally taken into account. The calculated results show that the maximum diameter of the fireball is equal to 289.94 m, indicates that all circled areas that have diameter within 289.94 m around the tank will be damaged by fireball. The maximum diameter for fireball is illustrated in Figure 4.

According to Table A4, a person who exposes to excessive radiation heat from the fires may receive fatal burns. Combustible structures maybe ignited by exposure to a radiant heatflux of 31.5 kW/m^2 or more. Therefore, it conservatively assumes that all men within the 31.5 kW/m^2 isopleths will experience high possibility of fatalities. Unprotected skin maybe severely burned if exposed to a radiant flux of5.0 kW/m^2 for 30 second or more. In the area between 31.5 kW/m^2 and 5.0 kW/m^2 isopleths, a person who is inside the building will be protected by the structure, but one who is outside the building and unable to reach the shelter quick enough may receive fatal burns. Figure 5 shows the radiation received by target buffer zones around LPG tank.

To estimate thermal radiation damage to both people and structures at a distance, from the pool fire, the radiation at that distance is required. Table 4 shows estimated fire pool size and the thermal radiation. The thermal radiation buffer zone from pool fire hazard is also visually presented in Figure 6 .

CONCLUSIONS

This paper presented preliminary studies on the potential of BLEVE hazard. Theoretical investigations of various methods for calculating the physical effects of explosions and fires of vessels containing liquefied petroleum gases (LPG) in Faculty of Engineering, UPM, have been carried out with several physical models. Zones of high fatality and damage on construction have been classified on the location map. Mapping the visual display of information, has shown its capability as a useful tool in hazard analysis and risk management. GIS can be used to analyze and predict the BLEVE events with the aid of the mapping tools and models on the potential risk area.
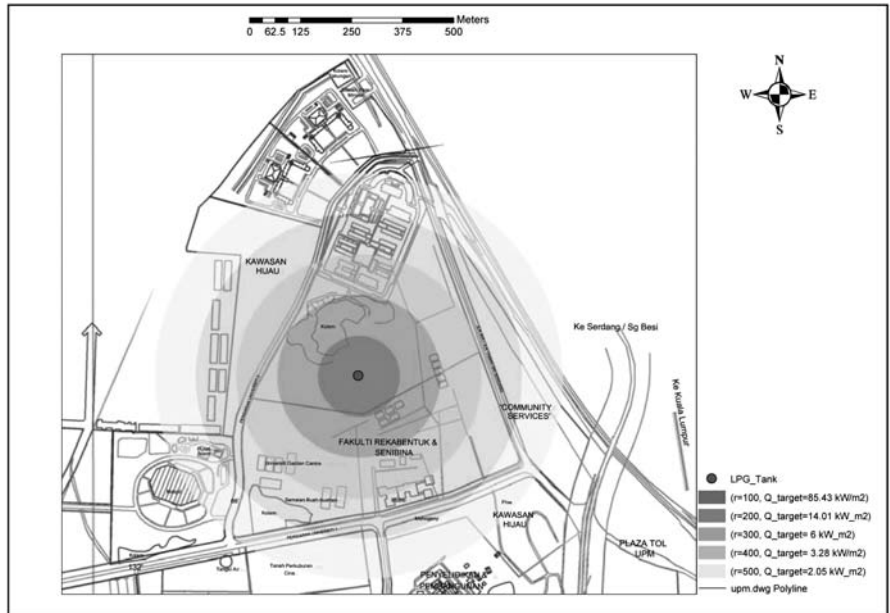
Figure 5: Radiation received buffer zones around LPG tank
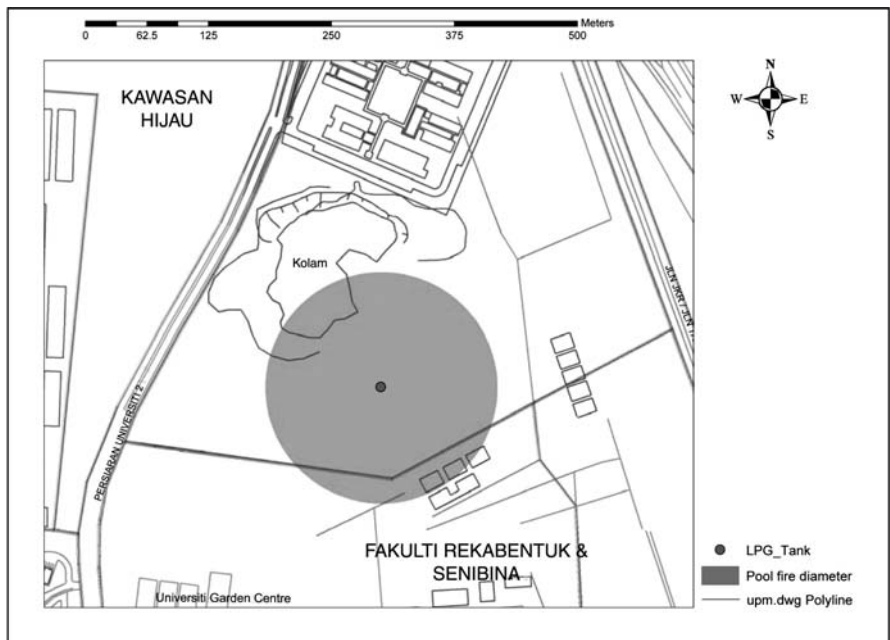
Figure 6: Thermal radiation from as function of pool fire diameter

Table 3: The radiation-received by a target

$r(m)$	$l\,(N/m^2)$	F_{21}	τ	$Q_{target}\,(kW/m^2)$
100	94.38	2.10	0.66	58.43
200	150.48	0.53	0.63	14.01
300	225.56	0.23	0.61	6.00
400	310.32	0.13	0.59	3.28
500	400.27	0.08	0.58	2.05

Table 4: Estimate the fire pool size and the thermal radiation

$M(kg)$	$A_p(m^2)$	$D(m)$	m	$L_f(m)$	$Q_R\,(kW/m^2)$
40,000	3642.99	68.12	0.099	85.92	$1.10*10^6$
60,000	5464.48	88.43	0.099	98.92	$1.65*10^6$
80,000	7285.97	96.34	0.099	109.32	$2.20*10^6$
100,000	9107.47	107.713	0.099	118.14	$2.75*10^6$
120,000	10928.96	117.99	0.099	125.86	$3.30*10^6$

Table A1: Eardrum Rupture Criteria for Exposure to Blast Overpressures

Likelihood of Eardrum Rupture	Peak Overpressure (kPa)
90%	84.12
50%	43.43
10%	22.06
1%	13.10

Table A2: Pressure effects on humans

Pressure (kPa)	Effect
35	Limit for eardrum rupture
70	Limit for lung damage
180	1% mortality
210	10% mortality
260	50% mortality
300	90% mortality
350	99% mortality

Table A3: Damage Estimates for Common Structures Based on Overpressure (These values are approximations)*

Pressure (kPa)	Damage
0.21	Occasional breaking of large glass windows already under strain
0.69	Breakage of small windows under strain
1.03	Typical pressure for glass breakage
2.07	"Safe distance" (probability 0.95 of no serious damage below this value); projectile limit; some damage to house ceilings; 10% windoe glass broken
2.76	Limited minor structural damage
3.4-6.9	Large and small windows usually shatter; occasional damage to window frames
4.8	Minor damage to house structures
6.9	Partial demolition of houses, made uninhabitable
6.9-13.8	Corrugated asbestos shatters; corrugated steel or aluminium panels, fastenings fail, followed by buckling; wood panels (standard housing), fastenings fail, panels blow in
13.8	Partial collapse of walls ans roofs of houses
13.8-20.7	Concrete or cinder block walls, not reinforced, shatter
17.2	50% destruction of brickwork of houses
20.7-27.6	Frameless, self-framing steel panel buildings demolished; rupture of oil storage tanks
27.6	Cladding of light industrial buildings ruptures
34.5	Wooden utility poles snap; tall hydraulic presses (40,000 Ib) in buildings slightly damage
34.5-48.2	Nearly complete destruction of houses
68.9	Probable total destruction of buildings; heavy machine tools (7000 Ib) moved and badly damaged, very heavy machine tools (12,000 Ib) survive

*V.J. Clancey, "Diagnostic Features of Explosion Damage," paper presented at the Sixth International Meeting of Forensic Sciences (Edinburgh, 1972)

Table A4: Effect of thermal radiation on construction [16]

Thermal radiation (kW/m2)	Effect	Distance (m)
37.5	Spontaneous ignition of wood after long exposure	124
23-25	Unprotected steel will reach thermal stress temperatures which can cause failures	151-157
	Non-piloted ignition of wood occurs	151
25	Cable insulation degrades	168-177
18-20	Piloted ignition of wood occurs	211
12.5	Thermal stress level high enough to cause structural failure. Minimum energy required for piloted ignition	
12.6	of wood, melting of plastic tubing	210
12	Plastic melts	215

REFERENCES

[1] International Labour Organisation (ILO), 1988. Major hazard control: A Practical Manual, ILO, London.

[2] Mustapha S. and Zain I., 2003. Safety Report: Maintaining Standard and Reviewing. IChemE, Symposium Series No. 149.

[3] Malder G., 2001. Deterministic and Probabilistic Approaches in Risk Analysis. (www.mahbsrv.jrc.it).

[4] Eisenberg N., Lynch, C. and Breeding R., 1975. Vulnerability Model: A Simulation System for Assessing Damage Resulting from Marine Spills. *Rep. CG-D-136-75. Enviro Control Inc., Rockville, MD.*

[5] Fischer, S., Forse'n, R., Hertzberg, O., Jacobsson, A., Koch, B., Runn, P., Thaning, L. and Winter, S., 1995. *Vadautslappav Brandfarliga Och Giftiga Gaser Och Vatskor* (in Swedish), FOA-D-95-00099-4.9-SE, Forsvarets Forskningsanstalt Stockholm.

[6] CCPS, 1989. Guidelines for Chemical Process Quantitative Risk Analysis. Centre for Chemical Process Safety of the American Institute of Chemical Engineering, New York.

[7] Baker E. et. al.,1983. Explosion hazards and evaluation. Elsevier, New York.

[8] Ozog, H., Melhem G., van den Berg B., Mercx P., 1996. Facility Sitting-Case Study Demonstrating Benefit of Analyzing Blast Dynamics. *International Conference and Workshop on Process Safety Management and Inherently* Safer Processes, AIChE/CCPS: 293-315.

[9] Roberts A., 1981. Thermal Radiation Hazards from Release of LPG Pressurised Storage. *Fire Safety Journal*, 4, 197-212.

[10] Fay J. and Lewis D., 1976. Unsteady burning of unconfirmed fuel vapour clouds. Sixteenth Symposium on Combustion, Massachusetts Institute of Technology, p.1397.

[11] Papazoglou I. and Aneziris O., 1999. Uncertainty quantification in the health consequences of the boiling liquid expanding vapour explosion phenomenon, *Journal of Hazardous Materials*. Vol. 67: 217-235.

[12] Pietersen C. and Huerta S., 1984. Analysis of the LPG Incident in San Juan Ixhuatepec. Mexico City. 19 November, TNO Report No. 85-0222: 8727-3325, The Hague.

[13] Petroliam Nasional Bhd (Petronas), 1989. Dagangan Tawau LPG and White Products Marketing Terminal Public Risk Assessment. Petronas Dagagan, Malaysia and Energy Analysis Report.

[14] Dow Chemical Co., 1993. Corporate Loss Prevention: Chemical Hazards Engineering Guidelines. The Dow Chemical Company, Michigan.

[15] *Preparation of safety cases for major hazard control,* NPC Hotel, Petaling Jaya, 1994.

[16] Dow, 1993, Corporate Loss Prevention. *Chemical Hazards Engineering Guidelines.* The Dow Chemical Company, Midland, Michigan.

NOMENCLATURES

A_p	Pool area	m^2
D	Pool diameter	m
$D_{initial}$	Initial ground level hemisphere diameter	m
D_{max}	Peak fireball diameter	m
E	Surface emitted flux	kW/m^2
E_{TNT}	Energy of explosion of TNT	KJ/kg
F_{rad}	Radiation fraction, typically (0.25-0.4)	-
F_{21}	View factor	-
g	Acceleration of gravity	m/s^2
H_{BLEVE}	Centre height of fireball	m
H_w	Jet flame conical half-width at flame tip	m
k	Constant specific for each fuel	m^{-1}
l	Path length, distance from flame surface to target	m
L_f	Flame height	m
M	Initial mass of flammable liquid	kg
m	Mass burning rate per unit area	$Kg.m^2.s$
$m\infty$	Mass burning rate per unite area for an infinite pool	$Kg.m^2.s$
m_{TNT}	Equivalent mass of TNT	kg
P_w	Water partial pressure	N/m^2
P_0	Peak overpressure	kPa
Q_R	Heat radiation by fire	kW
$Q_{t \arg et}$	Radiation received by a black body target	kW/m^2
Q_T	Total rate of heat release	kW
r	Distance from the ground-zero point of the explosion	m
t_{BLEVE}	Fireball duration	s

Greek Symbols

η	Empirical explosion efficiency, 0.95	-
ΔH_c	Heat of combustion	KJ/kg
τ	Atmospheric transmissivity	-
κ	Fraction of total heat emitted as radiation	-
ζ	Efficiency of combustion, (it can be assumed 95%)	-
ρ_a	Ambient air density	Kg/m^3

Application of Boundary Element Method for the Analysis of Potential Flow Field and Wave Resistance in Finite Depth of Water

Md. Shahjada Tarafder and Gazi Md. Khalil
Department of Naval Architecture and Marine Engineering,
Bangladesh University of Engineering and Technology, Dhaka-1000, Bangladesh, India

ABSTRACT

A boundary element method is presented for solving a nonlinear free surface flow problem for a ship moving with a uniform speed in shallow water. The free surface boundary condition is linearized by the systematic method of perturbation in terms of a small parameter. The surfaces are discretized into flat quadrilateral elements and the influence coefficients are calculated by Morino's analytical formula. Dawson's upstream finite difference operator is used in order to satisfy the radiation condition. A verification of the numerical modelling is made using the Wigley hull. The peak of the wave resistance curve and the wave pattern at the critical speed demonstrate the validity of the computer scheme.

Keywords : Boundary element method, free surface, perturbation method, shallow water effect and wave making resistance

INTRODUCTION

The resistance of a ship is quite sensitive to the effects of shallow water. In the first place, there is an appreciable change in potential flow around the hull. If the ship is considered as being at rest in a flowing stream of restricted depth, but unrestricted width, the water passing below it must speed up more than in deep water, with a consequent greater reduction in pressure and increased sinkage, trim and resistance. If the water is restricted laterally as in a river or canal, these effects are further exaggerated. The sinkage and trim in very shallow water may set an upper limit to the speed at which ships can operate without touching the bottom.

A second effect is the changes in the wave pattern which occur in passing from deep to shallow water. These changes have been studied by Havelock [4] for a pressure point impulse travelling over a free water surface. He has also proposed different approaches to obtain an appropriate formula for the ship resistance in shallow water in 1922 [5].

Kinoshita and Inui [9] extend Havelock's theory to satisfy the bottom boundary condition more exactly and Inui [7] further develops the theory to solve the channel problem. Kirsch [10] uses linearized wave theory to calculate the wave making resistance for simplified hull form in various water depths and channel widths. Muller [16] has carried out extensive experiments and theoretical calculations based on linearized wave theory to investigate the effect of shallow water on wave resistance. The wave resistance is determined by Guilloton's method and Havelock's integral.

More recently the Rankine source panel method based on linear wave theory has been applied to compute the wave resistance of ships in shallow water. Yasukawa [23] has developed a first order panel method based on Dawson's approach for the linear free surface condition. The shallow water effect is taken into consideration by replacing the bottom surface with Rankine sources. Lee [11] improves the solution efficiency over Yasukawa's work by choosing the Green function to be the sum of the Rankine source and its image with respect to bottom surface.

Kim et al. [8] analyze the free surface potential flow around ships in shallow water with linear and nonlinear free surface boundary conditions and simulated the shallow water effect by applying a symmetry condition on the bottom surface. The linear method is developed on the basis of double body approximation and thus the free surface condition is linearized with respect to the flow with an undisturbed free surface. In the nonlinear method the exact free surface conditions are approached in an iterative process, where in each iteration a condition linearized about the previous solution, is satisfied on the previously calculated wavy surface. The process starts with the free surface as a rigid lid and stops when the change in wave height between two iterations is below a given value.

Xinmin and Xiuheng [22] have applied Rankine source method to the computation of hydrodynamic forces and wave patterns of ship hulls moving in restricted water. Parabolic curved panels are adopted to model the hull surface and a body fitted grid is chosen to divide the local free surface. The other researchers who have made important contributions in the hydrodynamic characteristics of ships in shallow water are Monacella [15], Tuck and Taylor [21], Maruo and Tachibana [13] and Pettersen [17].

The aim of the present work is to investigate the influence of finite depth on the wave making characteristics of ships using a potential based panel method. The free surface conditions are linearized about the mean water surface by means of Taylor series expansion. A computer program PAFS (Panel Method Applied to Free Surface) is originally developed in the department of Naval Architecture and Ocean Engineering in Yokohama National University (Japan) for calculating the wave making resistance of ship in deep water. This program has been further extended by the

author to take into account the effect of finite depth on wave making resistance. The interested reader may find the details for the computer program in Tarafder [20]. The validity of the computer program is examined with the Wigley hull.

MATHEMATICAL MODELLING OF THE PROBLEM

Consider a ship moving in a finite depth of water h with a constant speed U in the direction of the positive x-axis, as shown in Figure 1. The z-axis is vertically upwards and the y-axis extends to starboards. The origin of the co-ordinate system is located in an undisturbed free surface at a midship, so that the undisturbed incident flow appears to be a streaming flow in the positive-x direction. It is assumed that the fluid is incompressible and inviscid and the flow irrotational. The total velocity potential function Φ can be expressed as

$$\begin{aligned} \Phi &= Ux + \phi \\ &= Ux + \sum_{n=1}^{\infty} \varepsilon^n \phi_n \end{aligned} \tag{1}$$

where, ε is a perturbation parameter and ϕ is the perturbation velocity potential due to the existence of the body. The disturbance velocity potential satisfies the Lapace equation $\nabla^2\phi = 0$ in the fluid domain V $\tag{2}$

The fluid domain V is bounded by the hull syrface S_H, free surface S_F, sea bottom S_B and the surface at infinity S_∞. Now the problem can be constructed by specifying the following boundary conditions as follows:

(a) *Hull boundary condition:* The hull boundary condition simply expresses the fact that the flow must be tangential to the hull surface i.e. the normal component of the velocity must be zero.

$$\begin{aligned} \varepsilon &: \nabla\phi_1.n = -Un_x \\ \varepsilon^2 &: \nabla\phi_2.n = 0 \end{aligned} \tag{3}$$

in which denotes the unit normal vector on the surface and is positive into the fluid.

(b) *Free surface condition:* The free surface condition is nonlinear in nature and should be satisfied on the true surface, which is unknown and can be linearized as a part of the solution using
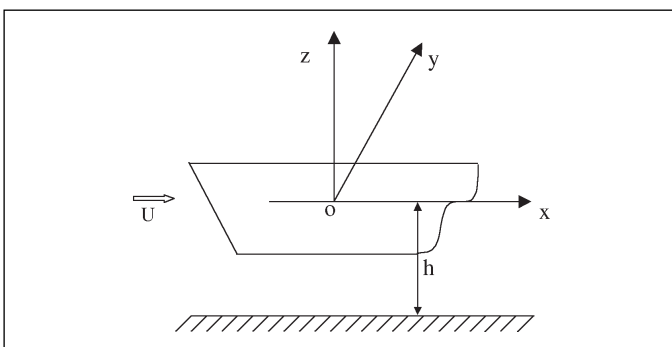

Figure 1: Definition sketch of the co-ordinate system

perturbation method. The free surface boundary condition for first and second order approximation can be written as (see Maruo, 1966) [12];

$$\varepsilon \quad : \phi_{1xx} + K_0\phi_{1z} = 0 \qquad \text{at } z = 0$$

$$\varepsilon^2 \quad : \phi_{2xx} + K_0\phi_{2z} = f(\phi_1) \tag{4}$$

$$f(\phi_1) = -\frac{1}{U}\frac{\partial}{\partial x}(\phi_{1x}^2 + \phi_{1y}^2 + \phi_{1z}^2) - \zeta_1\frac{\partial}{\partial z}(\phi_{1xx} + K_0\phi_{1z})$$

(c) *Sea bottom condition:* The first and second order vertical velocity component on the sea bottom can be expressed as

$$\begin{aligned} \varepsilon &\quad : \nabla\phi_1.n = 0 \\ \varepsilon^2 &\quad : \nabla\phi_2.n = 0 \qquad \text{at } z = -h \end{aligned} \tag{5}$$

(d) *Radiation condition:* It is necessary to impose a condition to ensure that the free surface waves vanish upstream of the disturbance.

THE BOUNDARY ELEMENT METHOD

Applying Green's second identity Laplace's equation can be transformed into an integral equation as (see Curle & Davis, 1968) ;

$$4\pi E\phi(p) = \sum_{j=1}^{N_H} \int_{S_H} \phi(q)\frac{\partial G}{\partial n_q} dS - \sum_{j=1}^{N_H} \int_{S_H} \frac{\partial\phi(q)}{\partial n_q} GdS$$

$$+ \sum_{j=1}^{N_B} \int_{S_B} \phi(q)\frac{\partial G}{\partial n_q} dS - \sum_{j=1}^{N_F} \int_{S_F} \phi(q)\frac{\partial\phi(q)}{\partial n_q} GdS \tag{6}$$

where, $E = \begin{cases} 1/2 \text{ on } S_H, S_B \\ 1 \text{ on } S_F \end{cases}$

The Green's function G satisfies the Laplace equation and can be approximated (see Faltinsen, 1993) as [3];

$$G = \frac{1}{R(p; q)} + \frac{1}{R'(p; q)}$$

where R is the position vector between the field point p and the point of singularity q on the surface and R´ is its image. The surface S_∞ is a control surface at a large distance from the body and is chosen as the surface of a circular cylinder of large radius. So the integral over the surface S_∞ must be zero as the radius of cylinder increases infinitely.

The integral over the element in equation (6) is calculated by Morino's analytical expression (see Suciu and Marino, 1976) [19] based on the assumption of quadrilateral hyperboloid element. After satisfying the boundary conditions as stated in equations (3) to (5), the integral equation (6) can be written into a matrix form as:

$$[A]x = [B].$$

where [A] and [B] are the matrices built up by the Green's function and its derivatives, and x is the column matrix formed by the strength of the sources and dipoles respectively. The second derivatives of velocity potentials in the left side of free surface

condition (4) are computed by Dawson's upstream finite difference operator (see Dawson, 1977) [2] in order to satisfy the radiation condition.

The derivatives of the velocity potentials (ϕx, ϕy) in right side of equation (4) are evaluated by fitting a second-degree polynomial function passing through the potentials at the centroid of three adjacent panels on the surfaces. The derivative of velocity potential along the z-direction is obtained after calculating the velocity potentials at three points on the normal vector. The matrix of linear system of equations is solved by LU decomposition method as described by Press et al. [18]. The advantage of using LU technique is that the authors only need to partition LU in one time for first order problem and subsequently, the authors shall apply it for higher order problems. Therefore, the CPU time can be saved.

CALCULATION OF WAVE PROFILE AND RESISTANCE

The linearized equation of wave profile for first and second order approximation can be obtained as

$$\zeta_1 = -\frac{U}{g}\phi_{1x} \tag{7}$$

$$\zeta_2 = -\frac{U}{g}\phi_{2x} - \frac{U}{g}\zeta_1\phi_{1xz} - \frac{1}{2g}(\phi_{1x}^2 + \phi_{1y}^2 + \phi_{1z}^2) \tag{8}$$

The wave resistance can be calculated by integration of pressure over the area of the hull up to the mean water level. After including the water line integral the wave making resistance can be obtained as below:

$$R_w = -\frac{1}{2}\int[\rho(U^2 - \nabla\Phi.\nabla\Phi) - \rho gz]\,dS - \frac{1}{2}\rho g\oint\zeta^2 n_x dl \tag{9}$$

RESULTS AND DISCUSSION

To investigate the shallow water effect on wave resistance and wave pattern around the ship-like body, the method has been tested for the Wigley hull. The equation of this type of hull surface (see Hofman and Kozarski, 2000) is

$$y(x,z) = \frac{B}{2}S(z)\left(1 - \frac{4x^2}{L^2}\right) \tag{10}$$

where B and T are the vessel width and draft respectively and $S(z)$ is a function defining the shape of the cross-sections. For rectangular (wall sided) cross-section $S(z) = 1$, for triangular cross-section $S(z) = 1+z/T$, for parabolic cross-sections $S(z) = 1-(z/T)^2$, etc. The symmetric parabolic ship section and parabolic waterlines are used in the present numerical treatment of the problem. The principal particulars of this model are shown in Table 1.

Since the body is symmetric, one-half of the computational domain is used for numerical treatment. The panels from 1.0 ship length upstream to 2.5 ship length downstream cover the free surface domain. The transverse extension of the free surface is about 1.6 ship length. The extent of the sea bottom is -3 ≤ x ≤ 5, 2 ≤ y ≤0. The number of panels on the hull, free surface and sea bottom are taken 40x7, 70x15 and 40x10 respectively as shown in Figure 2. A three-point upstream difference operator is used in both longitudinal and transverse directions to advent disturbances

Table 1: Principal particulars of the Wigley hull

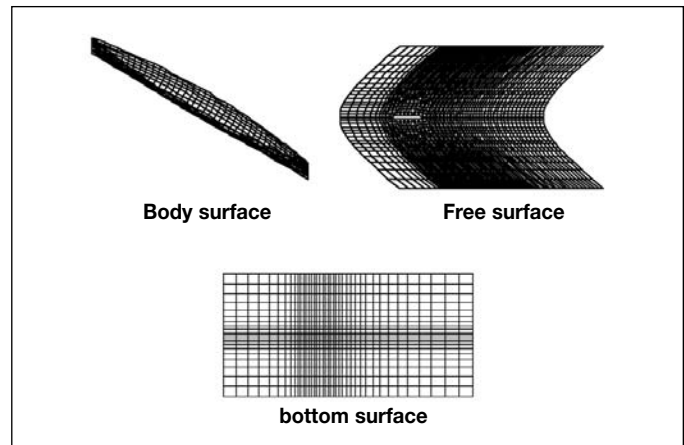| Parameter	Magnitude
B / L	0.10
T / L	0.0625
C_B, Block coefficient	0.444
C_M, Mid ship coefficient	0.667

Figure 2: Panel arrangements for the Wigley model

in the downstream direction. The method employs a clustering of panels on the free surface and sea bottom respectively.

Figure 3 presents a comparison of the wave profiles based on second order approximations with fixed sinkage and trim (abbreviated as 2nd, Fixed) in deep and shallow water at various ship speeds. The shallow water effect on the profiles becomes evident when the Froude number F_n, based on the length L of the model, reaches 0.332 and the differences between the wave profiles in deep and shallow water are mainly located at the middle and stern.

The calculated wave profiles at various water depth-to-draft ratios (h/T = 2.4, 2.8 & ∞) are also plotted in Figure 4 for a particular speed $F_n = 0.289$. The Froude number based on water depth is obtained from the relation, $F_h = F_n\sqrt{(L/h)}$. The two shallow water, h/T = 2.4 and 2.8 are subcritical depths (Fh < 1.0) with respect to the speed $F_n = 0.289$. The differences among the wave profiles in deep and shallow water become larger as the depth of the water decreases. The expected steeper bow waves are generated. This indicates that the second order nonlinear effect seems to be very significant for shallow water although the hull is quite slender.

Figure 5 shows a comparison of wave making resistance based on first and second order approximation with fixed sinkage and trim in deep and shallow water. The general effect of shallow water is to cause an increase in resistance at the lower speeds compared with the deep-water value but a reduction in resistance at the higher speeds as might be expected from the previous work of Millward and Bevan [14]. Since the four shallow water curves correspond to different water depth/draft (h/T) ratios it can be also seen that the shallow water effect becomes more pronounced as the depth-to-draft ratio decreases, that is, as the water becomes shallower, although in the supercritical region the difference among the four depths of water is small.

The wave making resistance of the Wigley hull based on first and second order approximation at $h/T = 2.8$ are also plotted in Figure 6. The first order solution predicts the maximum wave making resistance not at the critical speed but at a slightly faster speed, $F_h = 1.004$ while the second order solution predicts the maximum resistance at $F_h = 0.98$.

CONCLUSIONS

The present paper deals with the computation of free surface flow around a ship in shallow water using a potential based panel method. An attempt has been made to predict numerically the hydrodynamic characteristics of the Wigley hull in shallow water. The following conclusions can be drawn from the present numerical analysis:

a) The wave making resistance in shallow water begins to increase appreciably as the critical speed ($F_h = 1.0$) is approached and then decreases.

b) The first order solution predicts the maximum resistance not at the critical speed but at a slightly higher speed ($F_h = 1.004$) while the second order solution predicts the maximum wave making resistance at a slightly lower speed ($F_h = 0.98$).

c) The second order solution significantly improves the wave profiles particularly at the bow and the first trough but after that the difference between the first and second order results seems to be insignificant.

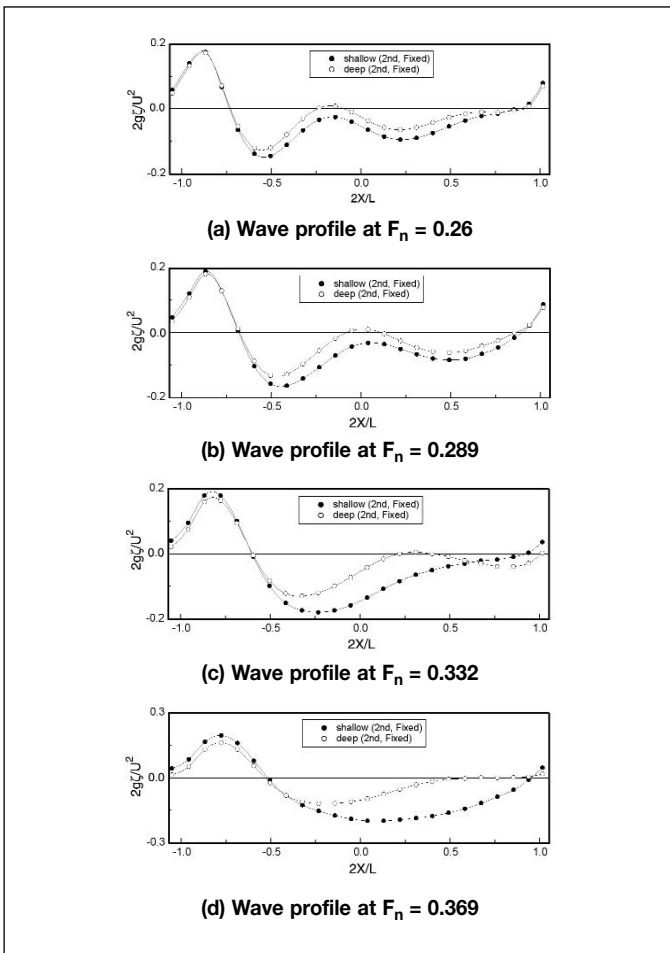d) In lower water depths the water surface in the midship region is remarkably displaced downward for all velocities.

(a) First order approximation

(b) Second order approximation

Figure 4: Comparison of calculated wave profiles in deep and subcritical depths for the Wigley hull at $F_n = 0.289$

(a) Wave profile at $F_n = 0.26$

(b) Wave profile at $F_n = 0.289$

(c) Wave profile at $F_n = 0.332$

(d) Wave profile at $F_n = 0.369$

Figure 3: Wave profiles (2nd, Fixed) of the Wigley hull in deep and at $h/T = 2.8$

(a) First order approximation

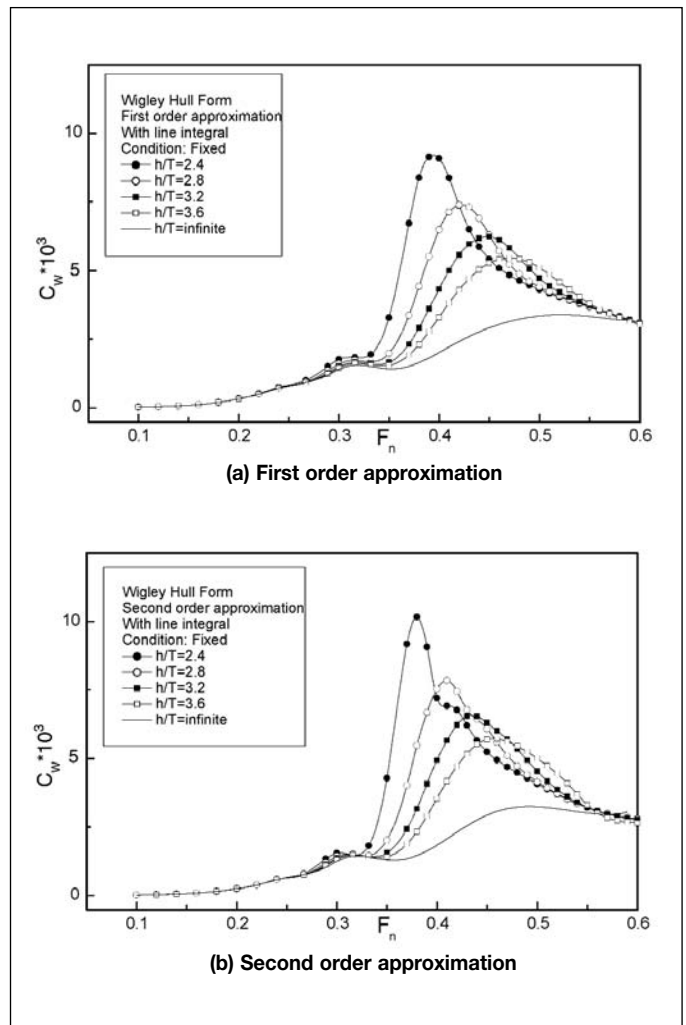(b) Second order approximation

Figure 5: Comparison of computed wave making resistance of the Wigley hull in deep and shallow water
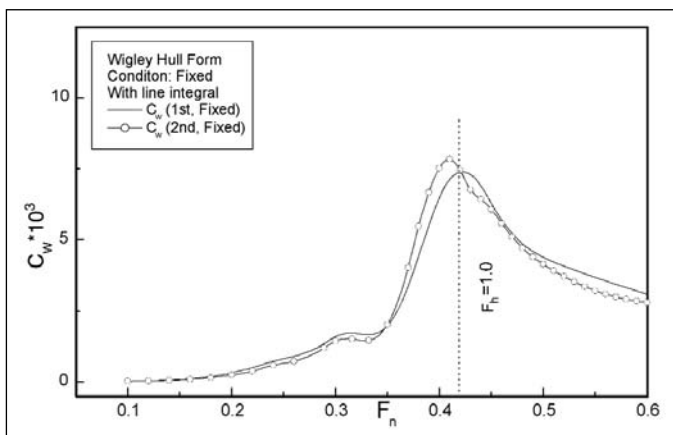
Figure 6: Wave making resistance of the Wigley hull at h/T = 2.8

REFERENCES

[1] Curle, N. and Davis, H. J. (1968), *Modern Fluid Dynamics*, Vol. 1, D. Van Nostrand Company Ltd., London, pp.108-111.

[2] Dawson, C. W. (1977), A practical computer method for solving ship-wave problems, *Proceedings of Second International Conference on Numerical Ship Hydrodynamics*, pp.30-38.

[3] Faltinsen, O. M. (1993), *Sea Loads on Ships and Offshore Structures*, Cambridge University Press, pp.110-122.

[4] Havelock, T. H. (1908), The propagation of groups of waves in dispersive media with application to waves on water produced by a traveling disturbance, *Proceedings of the Royal Society*, London, Vol. 81.

[5] Havelock, T. H. (1922), The effect of shallow water on wave resistance, *Proceedings of the Royal Society*, A, Vol. 100, pp.499-505.

[6] Hofman, M. and Kozarski, V. (2000), Shallow water resistance charts for preliminary vessel design, *International Shipbuilding Progress*, Vol. 47(449), pp.61-76.

[7] Inui, T. (1954), Wave making resistance in shallow sea and in restricted water with special reference to its discontinuities, *Journal of the Society of Naval Architects of Japan*, Vol. 76, pp.1-10.

[8] Kim, K, Choi, Y. Jansson, C. and Larsson, L. (1996), Linear and nonlinear calculations of the free surface potential flow around ships in shallow water, *20th Symposium on Naval Hydrodynamics*, pp.408-425.

[9] Kinoshita, M. & Inui, T. (1953), Wave making resistance of submerged spheroid ellipsoid and a ship in shallow sea, *Journal of the Society of Naval Architects of Japan*, Vol. 75, pp.119-135.

[10] Kirsch, M. (1966), Shallow water and channel effects on wave resistance, *Journal of Ship Research*, pp.164-181.

[11] Lee, S. J. (1992), Computation of wave resistance in the water of finite depth using a panel method, *The Journal SNAK92*, pp.130-135.

[12] Maruo, H. (1966), A note on the higher order theory of thin ships, *Bulletin of the Faculty of Engineering*, Yokohama National University, Vol. 15, pp.1-21.

[13] Maruo, H. and Tachibana, T. (1981), An investigation into the sinkage of a ship at the transcritical speed in shallow water, *Journal of the Society of Naval Architects of Japan, Vol. 150*, pp.56- 62.

[14] Millward, A. and Bevan, M. G. (1986), Effect of shallow water on a mathematical hull at high subcritical and supercritical speeds, *Journal of Ship Research, Vol. 30,* No.2, pp.85-93.

[15] Monacella, V. J. (1964), The disturbance due to a slender ship oscillating in waves in a fluid of finite depth, *Journal of Ship Research*, pp. 242-252.

[16] Muller, E. (1985), Analysis of the potential flow field and of ship resistance in water of finite depth, *International Shipbuilding Progress, Vol.32*, No.376, pp.266-277.

[17] Pettersen, B. (1982), Calculation of potential flow about three dimensional bodies in shallow water with particular application to ship maneuvering, *Journal of Ship Research, Vol.26,* No. 3, pp.149-165.

[18] Press, W. H., Teukolsky, S. A., Vetterling, W. T. and Flannery, B. P. (1999), *Numerical Recipes in Fortran 77: The Art of Scientific Computing, Vol. 1,* Cambridge University Press, pp.35-40.

[19] Suciu, E. O. and Morino L. (1976), A nonlinear finite element analysis for wings in steady incompressible flows with wake roll-up, AIAA Paper, No. 76-64, pp.1-10.

[20] Tarafder, M. S. (2002), Computation of Wave Making resistance of Ships in Shallow Water Using a Potential Based Panel Method, Doctoral Thesis, Department of Naval Architecture and Ocean Engineering, Yokohama National University, Japan.

[21] Tuck, E. O. and Taylor, P. J. (1970), Shallow wave problems in ship hydrodynamics, *8th Symposium on Naval Hydrodynamics*, pp. 627-658.

[22] Xinmin, X. and Xiuheng, W. (1996), A study on manoeuvring hydrodynamic forces acting on 3-d ship hulls with free surface effect in restricted water, *International Shipbuilding Progress, Vol.43,* No.433, pp.48-69.

[23] Yasukawa, H (1989), Calculation of free-surface flow around a ship in shallow water by rankine source method, *5th International Conference on Numerical Ship Hydrodynamics,* pp.643-653.

NOMENCLATURE

B	breadth of the ship model	S_∞	surface at infinity
C_w	wave making co-efficient	T	draft of the ship model
F_h	depth based Froude number	U	uniform velocity in the positive-x direction
F_n	length based Froude number	Φ	total velocity potential
g	acceleration due to gravity	ϕ	perturbation velocity potential due to presence of the body
G	Green's function	ϕ_x	velocity of the fluid in the x-direction
h	depth of water	ϕ_y	velocity of the fluid in the y-direction
K_0	wave number	ϕ_z	velocity of the fluid in the z-direction
L	length of the ship model	ϕ_1	first order perturbation velocity potential
N_H	number of panels on the hull surface	ϕ_2	second order contributory part for perturbation velocity potential
N_F	number of panels on the free surface		
N_B	number of panels on the bottom surface	ζ	wave elevation
S_H	hull surface	ζ_1	first order wave elevation
S_F	free surface	ζ_2	second order contributory part for wave elevation
S_B	bottom surface		

Aerodynamic Design and Aircraft Family Concept for an Advanced Technology Regional Aircraft (ATRA)

Prasetyo Edi, Prithvi Raj Arora and Mohammad Saleem
Faculty of Engineering, Universiti Putra Malaysia, 43400 UPM Serdang, Selangor

ABSTRACT

The aim of this work is to make a feasibility study of the application of combined Hybrid Laminar Flow Control (HLFC) - Variable Camber Wing (VCW) to the ATRA aircraft family. The VCW can be used as a lift control during cruise and climb to find the best lift/drag ratio. The prediction of ATRA's performance used computational fluid dynamic and empirical methods. During cruise, compared to the turbulent version, the lift/drag improvement was achieved due to the application of the combined HLFC-VCW. This improvement leads to the reduction of maximum take-off weight (MTOW) for constant design requirements and objectives (DR&O) and to the increased of range performance for constant MTOW.

Keywords : *Aerodynamic design, aircraft family concept, Hybrid Laminar Flow Control, Variable Camber Wing*

INTRODUCTION

For commercial transport aircraft, one of the basic aerodynamic performance objectives is to achieve the highest value of (Mach number)(Lift/Drag), $M(L/D)_{max}$, at the cruise Mach number. Climb and descent performance, especially for short-range missions, is also important and may suggest the "cruise" design conditions to be compromised.

Variable camber (VC) offers an opportunity to achieve considerable improvements in operational flexibility, buffet boundaries and performance (increasing lift/drag ratio in cruise and climb, due to cruise and climb always at optimum lift coefficient) [2].

It is believed that the application of a Hybrid Laminar Flow Control (HLFC) and Variable Camber (VC) as a flow control on the wing would assist in achieving such a goal, but must be shown to be cost-effective [3; 4].

This paper describes the exploration of the above concept and technologies to the initial design of Advanced Technology Regional Aircraft family (ATRA, twin turbofan with 83 - 133 passengers).

ATRA INITIAL BASELINE DESIGN

The following section is a brief design methodology for conceptual sizing of aircraft based on the author's experience as an aircraft configurator at IAe (Indonesian Aerospace)

Design Requirements (R) and Objectives (O), DR&O

As a successor of the regional jet, the baseline (ATRA-100) will offer 108 seats in two class layouts, while the stretched (ATRA-130) and shortened (ATRA-80) versions can accommodate for 133 seats in two class layouts and 83 seats in two class layouts respectively (R). The cruise cost-economic speed was set at Mach (M) = 0.8 (O) at a range of 2,250 nautical miles (nm) (ATRA-100), 2,000 nm (ATRA-80) and 2,500 nm (ATRA-130). For all versions the maximum approach speed will be 127 knots (O).

The improvement of aircraft performance compared to the current technology is expected to come from the application of new technology (i.e. : HLFC and VCW).

Initial Sizing

Using a simple method, the main parameters of initial sizing of the three versions are as follow :

	ATRA-80	ATRA-100	ATRA-130
MTOW (kg)	45,538	56,260	69,576
Thrust/Weight (T/W)	0.291	0.291	0.291
Weight/wing area (W/S), (kg/m²)	413.2	510.5	631.3

General Arrangement

Designing an aircraft can be an overwhelming task for a new configurator. The configurator must determine where the wing goes, how big to make the fuselage, and how to put all the pieces together.

Based on an existing aircraft there are two main types of general arrangement for a regional passenger jet transport aircrafts, i.e. :

1. Boeing, Airbus, Indonesian Aerospace (IAe) type : low-wing, low/fuselage-tail, engine mounted on the wing and tricycle landing gear attached on the wing and stowage on the wing-fuselage fairing.
2. Douglas, Fokker, Canadair type : low-wing, T-tail, engine mounted on the rear fuselage and tricycle landing gear attached on the wing and stowage on the wing-fuselage fairing.

There are several advantages and disadvantages between the above two types of general arrangement, as shown in Table 1.

Table 1: Advantages and disadvantage of two types of arrangement

Consideration	Type 1	Type 2
a. aero. cleanliness wings	bad	good
b. bending relief	yes	no
c. cabin noise levels	better	bad
d. aircraft c.g. management	easy	difficult
e. one engine out trim	difficult	easy
f. engine rotor burst	critical	good
g. engine ground clearance	critical	good
h. engine accessibility	good	difficult
i. fuel system	lighter	heavier

The engine mounted on the wing configuration is typical transport aircraft and the most common for most airliners. For this study, general arrangement type number 1 is selected for the ATRA-100 baseline configuration, ATRA-80 and ATRA-130, as shown in Figure 1.

AIRCRAFT FAMILY CONCEPT

Many Aircraft manufacturers , i.e. : Airbus, Boeing, McDonnell Douglas, Fokker, British Aerospace, IAe, etc., develop their aircraft family based on one wing and one fuselage cross section to reduce development costs. For one fuselage cross section aircraft family, alternatives for Regional Airliner family are :

1. Fixed wing geometry on mid-size, then Direct Operating Cost (DOC) penalties for off-optimum.
2. Fixed wing geometry on mid-size, modification of wing extension/reduction, then development costs
3. Variable Camber Wing (VCW) which could be optimum for all family, but will have increased development costs

The ATRA family will use the third of the above concepts. Figure 2 shows the ATRA Family concept. The Variable Camber Wing concept is described in the following section.

Because of wing fuel tank limitations, the payload-range for ATRA-130 cannot be achieved. There are several options to solve this problem, namely : (1) increase the wing area and/or thickness, (2) reduce the ATRA-130 range performance, (3) add fuel on empennage or fuselage tanks, (4) investigate the use of winglets to reduce induced drag and therefore fuel burn.

There are several options to design the low speed performances of the ATRA-130, namely : (1) use the same wing and high lift devices as the ATRA-100 but with increase in take-off and landing field distance, (2) increase the wing area, (3) improve the high lift devices performance.

The ATRA-100 has maximum design commonality with the ATRA-80 and ATRA-130. The level of commonality between the
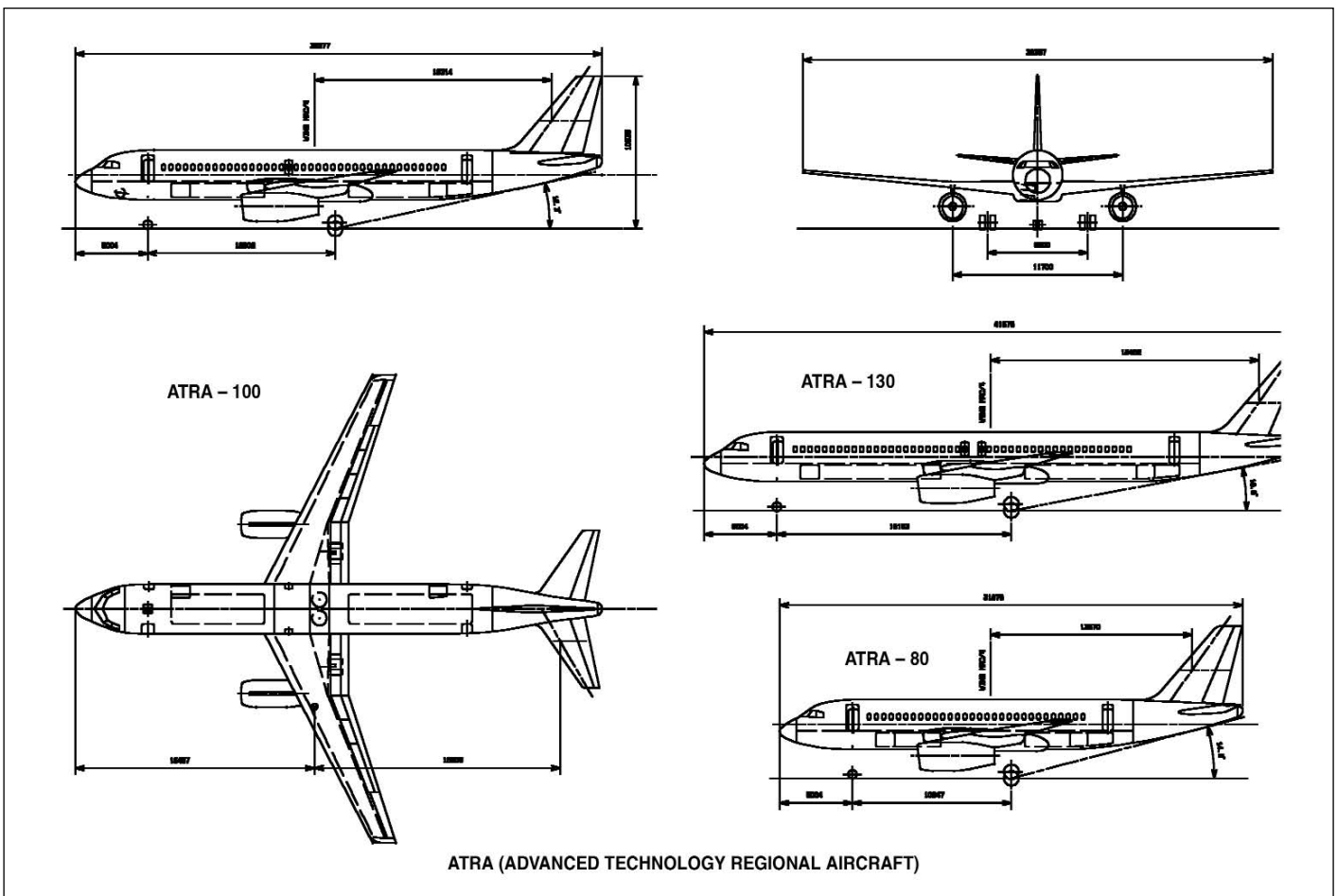

Figure 1: ATRA-100, with additional side views of ATRA-130 (centre) and ATRA-80 (below)

members of the ATRA standard-body aircraft family is such that the ATRA-80, ATRA-100 and ATRA-130 can essentially be operated as one aircraft type with positive effects on crew training, maintenance and aircraft scheduling. In addition, a mixed fleet of ATRA-100 aircraft combined with other aircraft in the ATRA family will allow airlines to better match capacity to demand whilst reducing operating costs, increasing crew productivity and simplifying ground handling.

Being the reduced/increased size development of the ATRA-100 the ATRA-80/ATRA-130 key changes are primarily related to size and capacity as all aircraft share similar systems and the same flight deck. Key changes include : derated/uprated engines, adapted systems and two fuselage plugs removed/added.

AERODYNAMIC DESIGN CONCEPTS FOR ATRA

The main issue in the application of new technologies in transport aircraft is the ability to employ them at low cost without reduction of their benefits. This cost is reflected in the following shares of DOC : fuel, ownership and maintenance. Laminar flow-variable camber technology will only produce acceptable DOC if the penalties due to additional weight and the complexity of the system do not exceed those of the fuel savings.

Hence the most important objective in realizing advanced laminar flow-variable camber technology is to reduce their additional system costs, weight and minimize maintainability and reliability costs.

Initial Wing Design

This section describes the initial design of wing for ATRA-100 baseline configuration. This wing design is unique, because it incorporates hybrid laminar flow control and variable camber wing technology.

A detailed examination of the very complex wing design is outside the scope of this work, but it is considered appropriate to mention some of the measures that may be taken, although not all of them are required for each design.

Performance Objectives

For a typical jet aircraft, the equation for cruise range (R) can be expressed as :

$$R = \left(\frac{a_0 \sqrt{\Theta}}{TSFC}\right)\left(\frac{ML}{D}\right) In\left(\frac{W_{initial}}{W_{final}}\right) \qquad (1)$$

where : a_0 = speed of sound
Θ = temperature ratio, T/T_0

The above equation states that if the thrust specific fuel consumption (TSFC) is considered to be nearly constant (which it usually is in the cruise region), a jet aircraft will get the most range for the fuel burned between weights $W_{initial}$ and W_{final} by making the quantity M(L/D), a maximum. The basic aerodynamic performance objective is, therefore, to achieve the highest value of M(L/D)max at the cruise Mach number. Climb and descent performance, especially for short range mission, is also important

and may suggest the "cruise" design conditions be compromised.

The improvement of M(L/D) compared to the current technology is expected to come from the application of new technology (i.e. : HLFC and VCW).

Wing area, planform and airfoil design

With MTOW of ATRA-100 = 56,260kg and W/S = 510.5 (kg/m²), wing area for ATRA-100 (S) = 110.21m².

Wing planform selection is based on a combination of criteria that require constant review during the design phase. Planform span, aspect ratio, sweep, and taper will be revised based on the trades taking place during the design. As sweep increases, the MTOW, operating empty weight (OEW), mission fuel and engine size increase for a constant aspect ratio and wing loading. As aspect ratio increases, OEW and MTOW increase while engine size and fuel burn decrease.

A detailed trade off study of planform parameters is outside the scope of this work. For ATRA-100 Baseline, sweep and taper ratio are taken from comparison with existing aircraft data, i.e. :

- A quarter chord sweep ($\wedge_{c/4}$) = 25 deg.
- Taper ratio (λ) = 0.274
- Aspect ratio (AR) = 9.5

The wing planform for ATRA-100 Baseline is illustrated in Figure 3.

Selection/design of the outboard wing sweep and outboard aerofoil section are made at the same time. Usually for most swept wings, the outboard aerofoil section defines the wing Mach number capability. This is a result of the higher outboard wing section loading compared to the inboard wing. The lower inboard wing lift is due to wing taper and the lower lift curve slopes near the side of fuselage. The outboard wing aerofoil is selected/designed based not only on the design Mach number but also on the aerofoil off-design characteristics. Good low Mach number lift capability is required for climb performance and for aircraft gross weight growth capability. High Mach number characteristics should exhibit low drag creep below cruise Mach number and still maintain gentle stall buffet characteristics. Shock position should remain fairly stable with small changes in Mach number or angle of attack to maintain good ride quality and handling characteristics.

Typically transonic HLFC aerofoil sections have been designed with pressure distributions having a small peak close to the leading edge, followed by a region of increasing pressure (an adverse pressure gradient) over the suction region, after which the 'roof-top' has a mildly favorable pressure gradient . Such a pressure distribution has been found to maximize the extent of laminar flow.

For this study, three airfoils were designed, i.e. airfoil for root, inboard and outboard, as shown in Figure 4.

THE APPLICATION OF COMBINED HLFC-VCW

Practical use of HLFC requires that laminar flow be maintained through a range of cruise lift coefficients and Mach numbers.
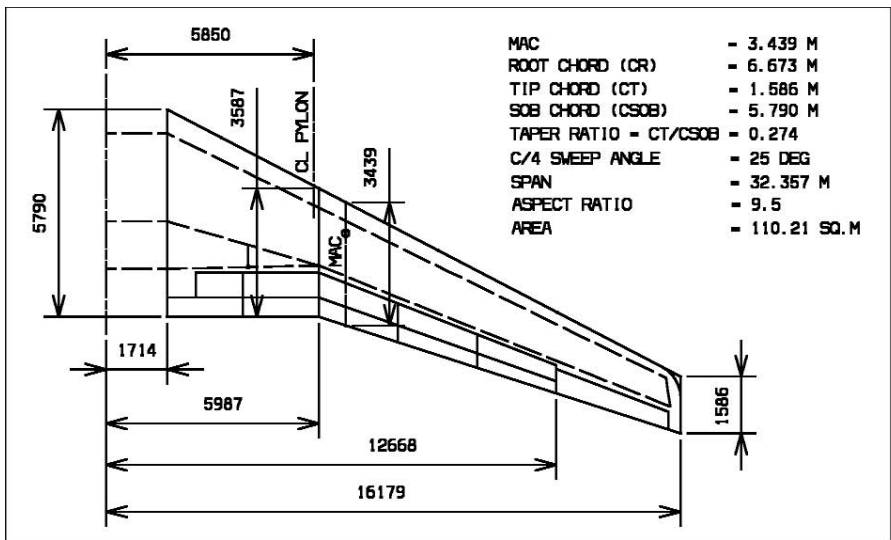
Payload-range   **concept**

System concept

trio regional airliner   adapted systems

Fuselage concept

two fuselage plugs removed/added

ATRA 80 (83 PAX: 8 FIRST CLASS 38" PITCH AND 75 TOURIST CLASS 32" PITCH)

− 1.955 M   − 2.444 M

ATRA100 (108 PAX: 8 FIRST CLASS 38" PITCH AND 100 TOURIST CLASS 32" PITCH)

+ 3.060 M   + 2.339 M

ATRA130 (133 PAX: 8 FIRST CLASS 38" PITCH AND 125 TOURIST CLASS 32" PITCH)

Variable camber wing concept   **Powerplant concept**

optimum cruise/climb management

constant altitude cruise management

derated/uprated engines

Figure 2: The ATRA Family concept

MAC	= 3.439 M
ROOT CHORD (CR)	= 6.673 M
TIP CHORD (CT)	= 1.586 M
SOB CHORD (CSOB)	= 5.790 M
TAPER RATIO = CT/CSOB	= 0.274
C/4 SWEEP ANGLE	= 25 DEG
SPAN	= 32.357 M
ASPECT RATIO	= 9.5
AREA	= 110.21 SQ.M

Figure 3: ATRA wing concept

Variations in lift coefficient and Mach number will change the wing pressure distributions from the optimum and may result in some loss of laminar flow. Therefore, it was decided to investigate a HLFC wing together VC-flap. Deflection of the VC-flap permits controlling the pressure distribution over the forward part of the airfoil, keeping it similar to the design pressure distribution, even when the lift coefficient and Mach number differ considerably from the design values. With careful design of VC-flap, it can be used to reduce the wave drag penalty, and to sustain attached flow in turbulent mode.

Candidate laminar flow – variable camber section

Figure 5 shows the section views of two wing configurations considered in this study. Configuration I has both upper and lower surface suction, from the front spar forward with leading edge systems as proposed by Lockheed [6]. Because it has no leading-edge device, it requires double-slotted fowler flaps to achieve maximum lift coefficient ($C_L$max) requirements. Configuration II replaces the lower surface suction with full-span Krueger flaps, which, combined with single-slotted fowler flaps, provide equivalent high lift capability. The Krueger flaps also shield the fixed leading edge from insect accumulation and provide a mounting for the anti icing system. Only the upper surface, however, has suction panels. The leading edge system used on configuration II is similar to leading edge systems as proposed by Douglas [6]. A summary of the advantages, risks, and disadvantages are :

- Configuration I : the advantages are (1) a simple system with no leading edge device and (2) upper and lower surface laminar flow for least drag. The disadvantages and risks are (1) more potential for insect contamination on the suction device which may cause boundary-layer transition, (2) high approach speeds and landing field lengths and/or a more complex trailing-edge high lift system, (3) longer take-off field lengths, particularly for hot, high-altitude conditions, and (4) a trim penalty due to higher rear loading (when the flaps are deployed).

- Configuration II : the advantages are (1) less potential insect contamination on the suction device, hence laminar boundary layer will be more stable, (2) simpler trailing-edge high lift devices, (3) lower approach speeds and shorter take-off and landing field lengths, and (4) less a trim penalty (when the flaps are deployed). The disadvantages and risks are (1) less drag reduction due to laminar flow only on the upper surface and (2) a more complex leading-edge system.

Preliminary estimates [4] indicated cruise drag reductions of about 11% for HLFC having laminar flow on the upper and lower surface, while the reduction for HLFC having laminar flow only on the upper surface was only 7%. The deficiencies noted for configuration I are related to low speed performance and insect contamination problems. The potential exists for high lift performance improvements if wings were specifically designed for the HLFC task. Although it has an inherently lower drag reduction, configuration II is more likely to provide a stable laminar boundary-layer due to a lower likelihood of being contaminated by insects. Taking into account the above considerations, configuration II was selected, for this study.

Hybrid laminar flow – variable camber section baseline configuration

The Hybrid Laminar Flow Control - Variable Camber Wing (HLFC-VCW) section baseline configuration for use on the ATRA-100's wing is shown in Figure 6.

Ideally the change in section profile craft of the rear spar should not cause separation of airflow, which would otherwise give rise to higher profile drag. To overcome the problem of separation, the radii of local curvature must be greater than half the chord, but not too high, as the section will have a higher pitching moment, and hence higher trim drag, which then will reduce the benefit of variable camber itself. The radii should be optimized between these two constraints. The radius is inherent to the trailing-edge upper surface of the aerofoil, so when the aerofoil is used for a VC concept, the aerofoil should be designed with taking into account the above considerations from the beginning.

The concept of variable camber used for the ATRA-100's wing is quite similar to traditional high lift devices. The camber variation is achieved by small rotation motions (in two directions for positive and negative deflections). In VC-operation the flap body slides between the spoiler trailing edge and the deflector door. The radius of flap rotation is picked-up from the radius of curvature of the aerofoil trailing edge upper surface at about 90% chord. Camber variation is therefore performed with continuity in surface curvature at all camber settings. During this process the spoiler position is unchanged.
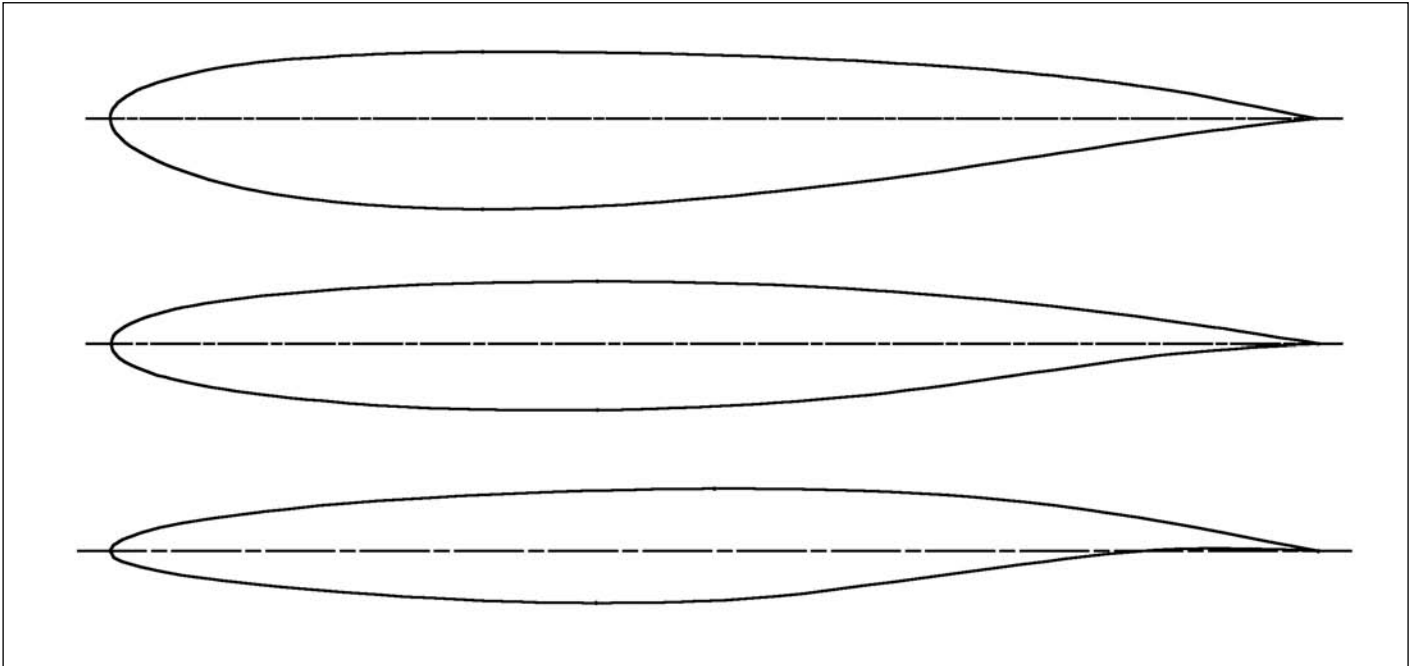
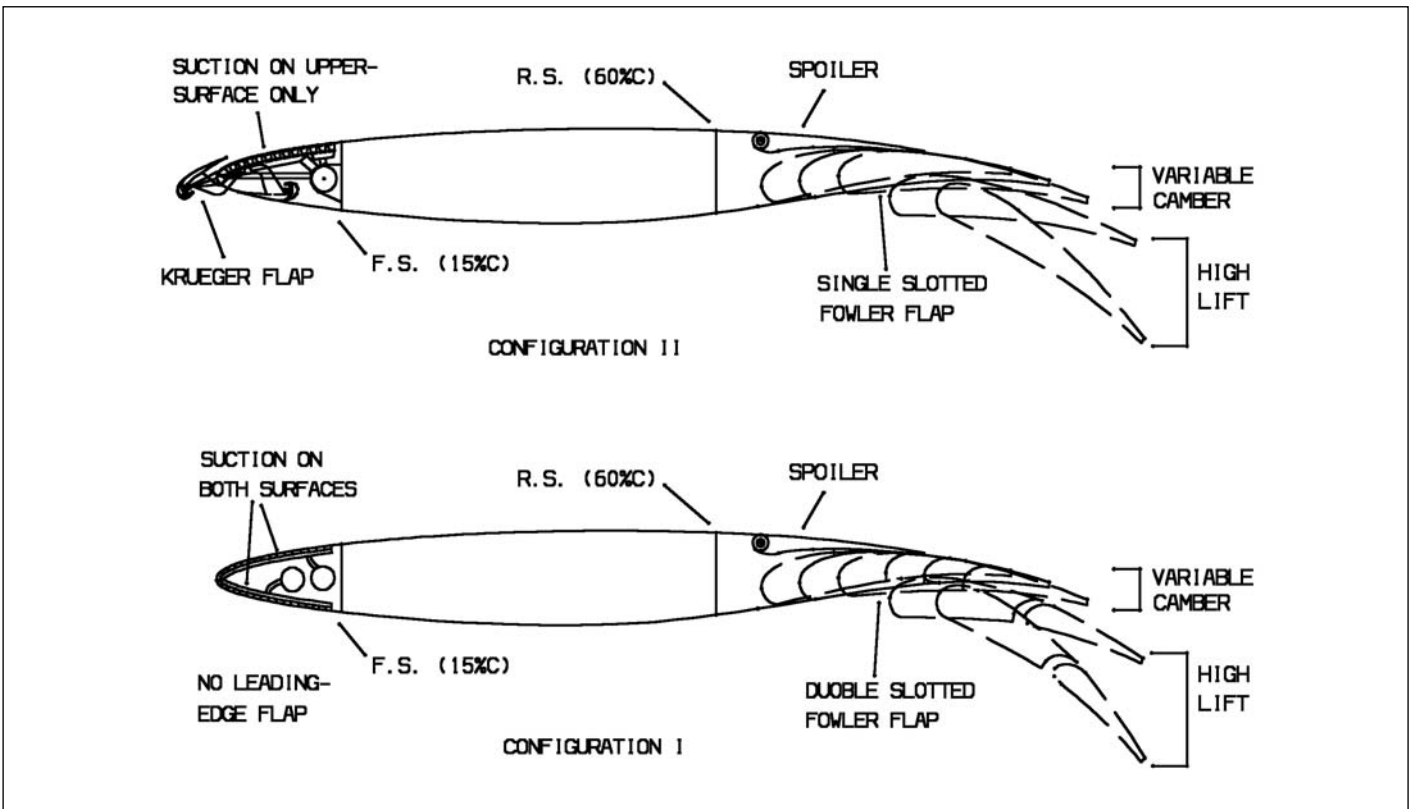*Figure 4: Airfoil for ATRA wing (root, inboard and outboard)*

Figure 5: Cross sections of candidate combine HLFC-VCW configurations

AIRCRAFT PERFORMANCE

The computational design analysis and revision of the ATRA-100 aircraft due to lift/drag improvement from the application of HLFC on the ATRA-100 aircraft compared to the turbulent version will be described in the following section.

Computational design analysis for ATRA-100 wing

Figures 7 and 8 show the contours of static pressure and Mach number in fully turbulent flow for variable-camber flap deflected respectively, for detailed flow analysis see Reference [3].

The lift coefficient versus angle of attack (alpha) for turbulent and laminar flow (HLFC-VCW) as featured in Figure 9.

Revision of the ATRA-100 aircraft

Technically, the application of the combined HLFC-VCW to the civil transport aircraft appears to provide significant performance gains in terms of fuel consumption and payload range
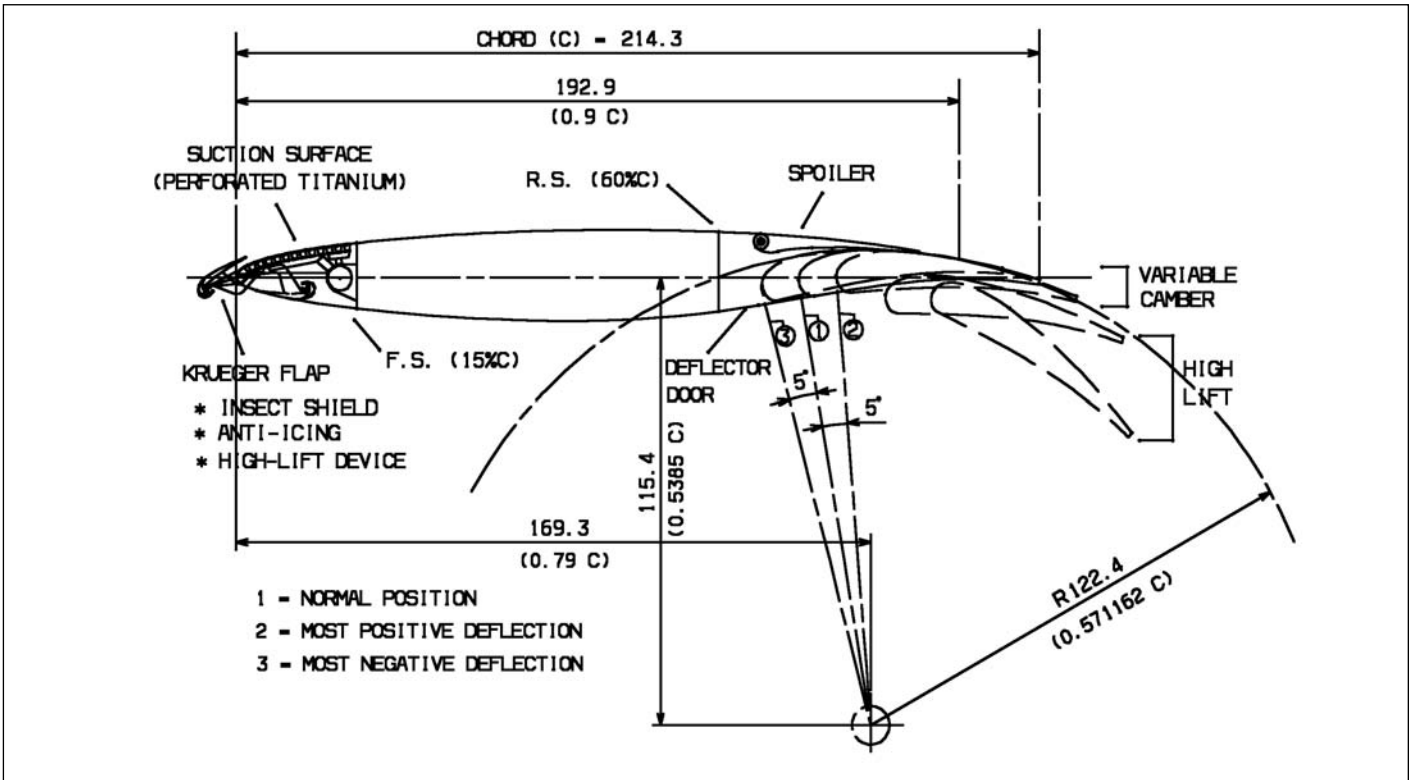
Figure 6: HLFC-VCW section baseline configuration
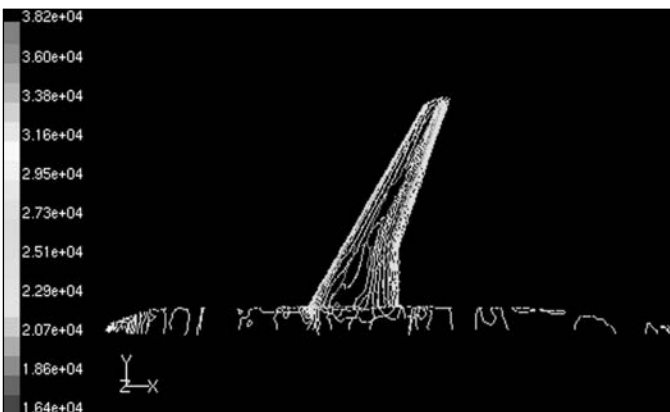
Figure 7: Configuration II: contours of static pressure, Pascal (fully turbulent flow)
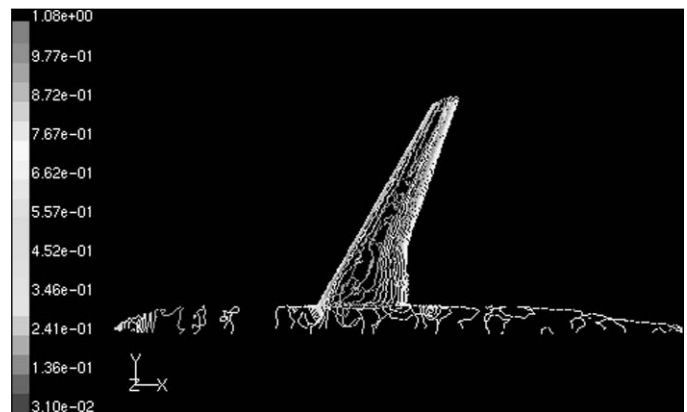

Figure 8: Configuration II: contours of March number (fully turbulent flow)

performance. However, in order to justify the implementation of the technology economically, it is necessary to consider the associated costs throughout the entire program.

It was judged that the most appropriate method of examining the cost implications of the combined HLFC-VCW would be to examine it's effects on the direct operating costs (DOC) of the aircraft. Due to lack of time, for the purposes of this research, aircraft weight reductions and increased range performance due to the application of the combine HLFC-VCW would be examine rather than DOC, with the assumption if the aircraft weight is reduced DOC would also reduce..

The aircraft lift/drag improvement at cruise (Mach 0.8, 35,000 ft and $R_N = 6.28e^6$/m) was 7.675 % of total cruise drag [3].

Some of the advantages and disadvantages of the application of the combined HLFC-VCW to civil transport aircraft compared to the turbulent version are [3] :

- HLFC systems weight = 0.373 % MTOW,
- VCW systems weight = 0.5 % wing weight,
- Lift/drag increment due to VCW application = 2.5 %,
- The increment in fuel flow to maintain the specified net thrust due to power off-take of HLFC suction systems = 0.2 %,
- Assumption : the reduction of wing sections t/c due to the application of the HLFC is eliminated by the application of VCW and wing sweep is unchanged.

The above values are from aircraft that does not closely match of the ATRA aircraft types included in this study, preventing any direct comparisons. However, the benefits and/or drawbacks associated with the various HLFC and/or VCW applications are provided. In the absence of a detailed investigation, it was decided to use the above values.

With the above predictions and assumptions and simple sizing method, the benefits of the combine HLFC-VCW to the ATRA-100
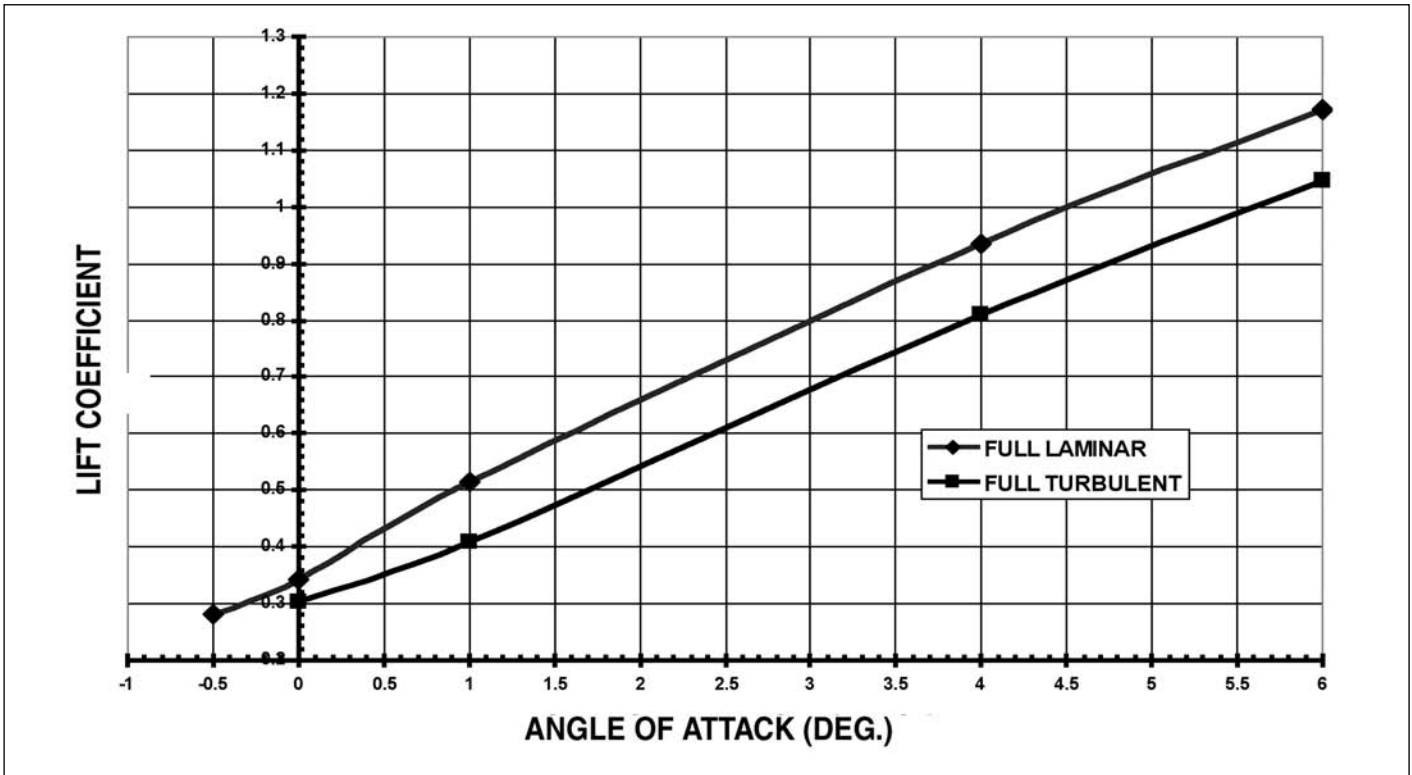
Figure 9: Configuration I: lift coefficient versus angle of attack (alpha)

aircraft compared to the turbulent version are : (1) for constant DR&O : MTOW reduction = 4.25 % and (2) for constant MTOW : range performance increased by 7.63 %.

CONCLUSIONS

The aircraft family concept using variable camber wing technology to manage the lift requirement is feasible from technical point of view.

During cruise (Mach 0.8, 35,000 ft and RN = 6.28e6/m), compared to the turbulent version, the lift/drag improvement due to the application of the combine HLFC-VCW to the ATRA aircraft was 7.675 % of total cruise drag; and for constant DR&O : MTOW reduction = 4.25 % while for constant MTOW : range performance increased by 7.63 %. The VCW can be used as a lift control during cruise and climb to find the best lift/drag ratio.

The application of combined HLFC–VCW concept to reduce the aircraft drag is feasible for a transport aircraft from aerodynamic point of view, but must be shown to be cost effective.

REFERENCES

[1] R. M. Denning, J. E. Allen and F. W. Armstrong. Future large aircraft design - the delta with suction. *The Aeronautical Journal,* 2212, 187-198 (May 1997).

[2] E. Greff. (Deutsche Airbus GmbH, Bremen, FRG). Aerodynamic design and technology concepts for a new ultra-high capacity aircraft. ICAS, 96-4.6.3. (1996).

[3] P. Edi. Investigation of the application of hybrid laminar flow control and variable camber wing design for regional aircraft. PhD thesis, AVT/CoA/Cranfield University, Cranfield - UK (1998).

[4] Boeing Commercial Airplane Company. Hybrid laminar flow control study final technical report. NASA CR 165930 (October 1982).

[5] Conceptual Design Staff. ATRA-100 Multi National Project Aircraft (Boeing, MBB, Fokker, IPTN). Wing Design Doc. Bandung-Indonesia. 1987.

[6] R. D. Wagner, D. V. Maddalon and D. F. Fisher. Laminar Flow Control Leading-Edge Systems in Simulated Airline Service. *Journal of Aircraft, Vol. 27,* No. 3, March 1990.

INVITATION

To all members

Every year the Institution receives invitation from government ministries to participate in dialogues concerning the engineering profession, be it in trade (both domestic and international), taxation or some general topics on science and the environment. In these dialogues, the primary purpose is to protect and advance the rights and interests of the engineering profession as a whole, or as an individual, a professional or a consumer, or as general public.

IEM has set up a committee to prepare and compile the views of members for presentation in the dialogue meetings. A series of meetings would be scheduled to enable members to air their views. Notices of such meetings will be announced in the Bulletin from time to time. Please submit details to the Secretariat if you have any views of interests.

INFORMATION FOR AUTHORS

Submission of a contribution is taken to manifest the fact that the submission has not been submitted, accepted, published, or copyrighted elsewhere.

To avoid publication delays, please send all manuscripts to the Editor and observe the following guidelines.

A) SUBMISSION OF PAPER

Send four (4) copies of your manuscript. Each copy should be complete with illustrations (if any) and an abstract. Submission should be made to the address below:

Chief Editor
The Institution of Engineers, Malaysia
Bangunan Ingenieur
Lots 60 & 62, Jalan 52/4
Peti Surat 223, Jalan Sultan
46720 Petaling Jaya
Selangor Darul Ehsan
Tel : 03-7968 4001 / 7968 4002
Fax : 03-7957 7678
E-mail : pub@iem.org.my
Website : http://www.iem.org.my

Three types of papers are solicited for the IEM Journal:

(1) **Regular Paper** – Presentation of significant research, developments or applications in any field of engineering or within the scope of the journal. Tutorials and surveys are also considered. For submission, the length should be about 30 pages; double-spacing, single column with font of 12 (Times).

(2) **Brief Paper** – A concise description of new technical concepts or applications within the scope of the journal. Submission should be about 20 pages; double-spacing, single column with font of 12 (Times).

(3) **Technical Correspondence** – Letter to the Editor, comments on established engineering topics and discussion of published papers. Submission should be about 10 pages; double-spacing, single column with font of 12 (Times).

NOTE: *In the event your paper is accepted for publication, the style of manuscript is in a different format (see point 7 below)*

Manuscripts submitted as papers should state the significance of the problem in the Introduction.

Paper size should be of A4 (210 cm X 297 cm) with 2 cm margins on the left, right, and bottom and 3 cm from the top.

Enclose a signed letter giving your preferred address, telephone, fax number, and e-mail address (if available) for correspondence and return of proofs.

If the manuscript has been presented, published, or submitted for publication elsewhere, please also inform the Editor. Our primary objective is to published technical materials not available elsewhere, but on occasion we publish papers of unusual merit that have appear or will appear before other audiences.

The language of the Journal is English. However, papers in Bahasa Melayu are also accepted and an abstract in English must be included.

Note that upon acceptance of an article for publication, the author is requested to submit a camera-ready format of the manuscript with single-spacing, double-column and font of 10 (Times). Illustrations should be included in the text. An electronic copy of the manuscript should also be submitted. The author is also requested to submit a passport-sized and a short biography. This information will be sent to the author by the Editor.

B) STYLE FOR MANUSCRIPT

The manuscript should be typewritten using double-space, using font of 12 (Times); use one side of sheet only and single column format.

The format for IEM Journal follows that of the IEEE Transactions (USA), except that the submission for you should follow Point 1 above.

As we practice blind review, please do not put your name and address in the manuscript.

Provide and informative 100 to 250 words abstract at the head of the manuscript.

All section should be numbered in Roman such as 1, 11, etc. with the title in capitals.

Sub-sections should be numbered in alphabet such as A, B, C, etc.

Sub-sub-sections (if any) should be numbered as A., A.2, etc.

Number all equations in round brackets such as ( ) and flush to right. The equation should be in the center.

References in the text should be cited each by a reference number in square brackets, e.g. [12] or [4; 6], etc.

In the REFERENCE section, the references should be written as follows :

Style for papers: Reference Number, Author, first initials followed by last name, title (italics), location and publisher, year, chapter or page numbers, month, and year.

Style for books : Reference Number, Author, first initial followed by last name, title (italics), location and publisher, year, chapter or page numbers (if desired).

Sample format for REFERENCES are as follows :

(for papers)

[3]   M. Khalid, S. Omatu, and R. Yusof, "Temperature Regulations with Neural Networks and Alternative Control Shcemes"' IEEE Trans on Neural Networks, Vol. 6, No. 3, pp. 572-582, May, 1995.

(for books)

[4]   S. Omatu, M. Khalid, and R. Yusof, Neural-Control and Its Applications,London: Springer-Verlag, 1995.

If your paper is in Bahasa Melayu, please provide an ABSTRACT in English.

In the event of the paper being accepted, we will require the camera-steady manuscript to be submitted in a double column format, single-spacing and font of 10 (Times). Include all illustrations in between the text (if possible). An electronic copy should be submitted. We prefer word processing to be done in Microsoft Word. If other word processing software is used, please specify.

C) STYLE FOR ILLUSTRATIONS

Try to include the illustrations in between the text.

Originals for illustrations should be sharp, noise-free and of good contrast.

Each illustration must be numbered such as "Figure 1, Figure 2, etc." and have a meaningful caption at the bottom.

For tables, the caption must be at the top.

On graphs, show only the coordinate axes, or at most the major grid lines, to avoid a dense hard-thread result.

All lettering should be large enough to permit legible reduction of the figure to column width, perhaps as much as 4:1. Typing on figures is not acceptable.

Photographs should be glossy prints, of good contrast and gradation and any reasonable size.

Number each original on the back, or at the bottom of the front, and also indicate the author's name.

Upon acceptance of your paper submit a set of the figures and a list of the captions.